TABLE DES MATIÈRES

Page

INTRODUCTION 1

CHAPITRE 1 ÉTAT DE L'ART 5
1.1 Argiles lamellaires comme renfort 5
1.1.1 Structure cristallographique de la montmorillonite 6
1.1.2 Traitement organophile de la montmorillonite 7
1.2 Polymères thermoplastiques comme matrice 10
1.3 Nanocomposites 12
1.3.1 Définition 12
1.3.2 Interphase 12
1.3.3 Structure des nanocomposites 13
1.4 Techniques d'élaboration des nanocomposites 14
1.4.1 Polymérisation in situ 14
1.5 Compatibilisation des nanocomposites 17
1.6 Propriétés mécaniques 18
1.7 Propriétés thermomécaniques 19
1.8 Stabilité thermique 20
1.9 Propriétés diélectriques 21
1.9.1 Permittivité diélectrique 21
1.9.2 Mécanismes de polarisation 23
1.9.3 Relaxation de Debye 25
1.9.4 Relaxation dans les polymères 26
1.9.5 Rigidité diélectrique 28

CHAPITRE 2 MATÉRIAUX ET MÉTHODOLOGIE 33
2.1 Matériaux et procédé de fabrication 33
2.2 Analyse morphologique 35
2.2.1 Diffraction des rayons X (XRD) 35
2.2.2 Microscopie électronique à balayage (MEB) 35
2.2.3 Microscopie électronique à transmission (MET) 36
2.2.4 Microscopie optique (MOP) 36
2.2.5 Microscope à force atomique (AFM) 36
2.3 Propriétés thermiques 37
2.3.1 Analyse thermique par DSC 37
2.3.2 Analyse thermogravimétrique (ATG) 38
2.4 Analyse mécanique dynamique par DMTA 38
2.5 Mesures diélectriques 40
2.5.1 Spectroscopie diélectrique 40
2.5.2 Mesure de rigidité diélectrique 41

CHAPITRE 3 ARTICLE I: LDPE/HDPE/Clay Nanocomposites: Effects of Compatibilizer on the Structure and Dielectric Response 43

3.1 Introduction 44
3.2 Experiment 45
3.2.1 Materials 45
3.2.2 Preparation of nanocomposites 46
3.3 Characterization and measurements 47
3.3.1 Differential scanning calorimetry (DSC) 47
3.3.2 X-ray diffraction (XRD) 47
3.3.3 Microscopical Observations 47
3.3.4 Dielectric Relaxation Spectroscopy 48
3.4 Results and discussion 50
3.4.4 Broadband dielectric spectroscopy 56
3.5 Conclusion 64

CHAPITRE 4 ARTICLE II: Correlation Between Structure and Dielectric Breakdown in LDPE/HDPE/Clay Nanocomposites 65
4.1 Introduction 66
4.2 Experiment 67
4.2.1 Materials 67
4.2.2 Preparation of nanocomposites 67
4.3 Characterization and measurements 68
4.3.1 Optical Microscope 68
4.3.2 Atomic Force Microscope (AFM) 68
4.3.3 Transmission electron microscope (TEM) 69
4.3.4 TGA Characterization 69
4.3.5 Dynamic Mechanical Analysis by DMTA 69
4.3.6 Dielectric Strength 70
4.4 Results and discussion 71
4.4.1 Optical Microscopy 71
4.4.2 Surface Roughness 73
4.4.3 Clay Dispersion by TEM 75
4.4.4 Thermal Properties 75
4.4.5 Dynamic mechanical behavior 79
4.4.6 Dielectric breakdown measurements 82
4.5 Conclusion 84

CHAPITRE 5 ARTICLE III: Structural and Dielectric Studies of LLDPE/O-MMT Nanocomposites 87
5.1 Introduction 88
5.2 Experiment 89
5.2.1 Materials 89
5.2.2 Sample preparation 89
5.3 Characterization and measurements 90
5.3.1 X-ray diffraction (XRD) 90
5.3.2 Transmission electron microscopy (TEM) 91
5.3.3 Atomic force microscopy (AFM) 91

5.3.4 Scanning electron microscopy (SEM) 91
5.3.5 Differential scanning calorimetry (DSC) 91
5.3.6 Fourier transform infrared spectroscopy (FTIR) 92
5.3.7 Dielectric relaxation spectroscopy 92
5.3.8 Dielectric breakdown strength 92
5.4 Results and discussion 93
5.4.1 X-ray diffraction (XRD) technique 93
5.4.2 Microstructure of nanocomposites 94
5.4.3 Atomic force microscopy 95
5.4.4 Thermal Properties 96
5.4.5 FTIR Spectroscopy 97
5.4.6 Effect of screw speed on morphological characterization 99
5.4.7 Broadband dielectric spectroscopy 100
5.4.8 Dielectric breakdown measurements 100
5.5 Conclusion 103

CHAPITRE 6 ARTICLE IV: Simulation and Modeling of Polyethylene/Clay Nanocomposite for Dielectric Application 105
6.1 Introduction 106
6.2 Analysis 107
6.2.1 Analytical models 107
6.2.2 Numerical Methods 111
6.3 Results and discussion 112
6.3.1 Simulation Setup 112
6.3.2 Ordered distribution 114
6.3.3 Random Distribution 117
6.3.4 Effect of the Permittivity of the Inclusion on Effective Permittivity 120
6.3.5 Effect of the Radius (and Volume Fraction) of the Inclusion on Effective Permittivity 123
6.4 Conclusion 125

CONCLUSION GÉNÉRALE 127

RECOMMANDATIONS 131

ANNEXE I PUBLICATIONS 133

LISTE DE RÉFÉRENCES BIBLIOGRAPHIQUES 135

LISTE DES TABLEAUX

Page

Tableau 2.1 Propriétés physiques des matériaux utilisés....33

Tableau 3.1 Sample formulation and designation 46

Tableau 3.2 DSC data for PE and its nanocomposites 52

Tableau 3.3 2θ and d_{001} data for the different nanocomposites 54

Tableau 4.1 Samples formulation and designation....68

Tableau 4.2 Surface roughness data of PE and its nanocomposites 73

Tableau 4.3 TGA data of PE and its nanocomposites in air atmosphere....77

Tableau 4.4 TGA data of PE and its nanocomposites in nitrogen atmosphere 79

Tableau 4.5 Effect of O-MMT clay and compatibilizer on storage modulus E' at different temperatures 80

Tableau 4.6 Effect of O-MMT clay and compatibilizer on loss modulus E'' at different temperatures 81

Tableau 4.7 Weibull parameters for dielectric breakdown strength of PE and its nanocomposites 84

Tableau 5.1 Samples formulation and designation....90

Tableau 5.2 DSC results for pure LLDPE and LLDPE/O-MMT nanocomposites 97

Tableau 5.3 Weibull parameters for dielectric breakdown strength of LLDPE and its nanocomposites....103

LISTE DES FIGURES

Page

Figure 1.1 Schéma de différentes échelles d'une particule de montmorillonite
Tirée de Gloaguen and Lefebvre (2007, p.4) 5

Figure 1.2 Représentation de la structure de montmorillonite
Tirée de Gloaguen and Lefebvre (2007, p.4) 6

Figure 1.3 Schématisation des exemples de tensioactifs :
(a) Alkylammonium (b) Alkyltriméthylammonium
(c) Dialkyldiméthylammonium
(d) Alkylbis(2-hydroxyéthyl)méthylammonium
(e) Alkylbenzyldiméthylammonium
Tirée de Lertwimolnum (2006, p. 12) 7

Figure 1.4 Variation de la distance interlamellaire d_{001} en fonction de la longueur de chaîne Alkyle
Tirée de Lertwimolnum (2006, p. 13) 8

Figure 1.5 Évolution de la distance interlamellaire d_{001} en fonction de la concentration d'agent d'interface
Tirée de Zhao (2003, p. 9262) 9

Figure 1.6 Orientations des chaînes hydrocarbonées dans l'espace entre les feuillets d'argile
Tirée de de Paiva (2008, p. 10) 10

Figure 1.7 Représentation de la description multi-échelles du polyéthylène
Tirée de Doumige (2010, p. 8) 11

Figure 1.8 Évolution du pourcentage du volume du renfort A occupé par l'interphase AB en fonction du diamètre du renfort A
Tirée de Lewis (2004, p. 740) 12

Figure 1.9 Différentes structures de nanocomposites polymère / argile:
(a) Microcomposite; (b) Nanocomposite intercalé; (c) Nanocomposite exfolié
Tirée de Ambid (2007, p. 24) 13

Figure 1.10 Schéma de différentes étapes de la formation du nylon/argile nanocomposites par polymérisations in situ
Tirée de Gloaguen and Lefebvre (2007, p. NM 3050-7) 14

Rapport-Gratuit.com

Figure 1.11 Formation de nanocomposites par mélange en solution
Tirée de Gloaguen and Lefebvre (2007, p. NM 3050-8) 15

Figure 1.12 Schéma de l'élaboration de nanocomposites par mélange à l'état fondu
Tirée de Gloaguen and Lefebvre (2007, p. NM 3050-9) 16

Figure 1.13 Effet du taux de greffage sur l'état de dispersion dans les nanocomposites LLDPE-g-MAH+5 wt % Closite 20A: (a) 0.29 wt %, (b) 0.22 wt %, (c) 0.11 wt %, (d) 0.07 wt %, (e) Closite 20A
Tirée de Wang (2001, p. 9824) 17

Figure 1.14 Influence du taux de charges minérales sur le module d'élasticité du Nylon 6
Tirée de Perez (2008, p. 39).....18

Figure 1.15 Évolution du tan (δ) en fonction de (T-Tg) pour différents nanocomposites avec différents taux de charge de silice
Tirée de Perez (2008, p. 40).....19

Figure 1.16 Évolution de la température de décomposition des nanocomposites LLDPE/MMT en fonction de taux de charge de MMT
Tirée de Qiu (2006, p. 926).....20

Figure 1.17 Schéma représente les différents types de polarisation
Tirée de Dubois (1998, p. E 1850-4) 24

Figure 1.18 Évolution en fonction de la fréquence de la partie réelle et imaginaire de la permittivité diélectrique complexe
Tirée de Rigaud (1995, p.257) 25

Figure 1.19 Variation de la perte diélectrique ε″ en fonction de la fréquence des systèmes PE et PE/nanoargile nanocomposites à la température ambiante
Tirée de Tomer (2011, p. 074113-6).....27

Figure 1.20 Évolution du taux de relaxation en fonction de l'inverse de la température des systèmes Poly(propylene-*graft*-maleic anhydride) et ses nanocomposites
Tirée de Böhning (2005, p. 2772).....27

Figure 1.21 Arborescence observée dans un isolant solide
Tirée de Tilmatine (2006, p. 12) 28

Figure 1.22 Variation de la rigidité diélectrique des systèmes LDPE/HDPE, LDPE et XLPE
Tirée de Green (2011, p. 38) (Green et al., 2011).....29

Figure 1.23 Variation de la rigidité diélectrique des systèmes PE/nanoargile nanocomposites
Tirée de Green (2008, p. 140).....30

Figure 2.1 Schéma représentant le procédé d'élaboration des nanocomposites par la technique du mélange à l'état fondu 34

Figure 2.2 Schéma représentant le principe de mesure par DSC
Tirée de Perez (2008, p. 61).....37

Figure 2.3 Principe de mesure par Analyse Thermo–Gravimétrique (TGA)
Tirée de Sawi (2010, p. 62).....38

Figure 2.4 Analyse Thermomécanique Dynamique DMTA 39

Figure 2.5 Principe de mesure en spectroscopie diélectrique
Tirée de Perez (2008, p. 66).....40

Figure 2.6 Testeur d'huile utilisé pour une mesure de rigidité diélectrique.....41

Figure 3.1 DSC heating thermograms of neat PE, PE/O-MMT and PE/O-MMT/PE-MA nanocomposites.....51

Figure 3.2 DSC cooling thermograms of neat PE, PE/O-MMT and PE/O-MMT/PE-MA nanocomposites.....51

Figure 3.3 X-ray diffraction patterns for MB and PE nanocomposites with and without compatibilizer 53

Figure 3.4 Representative SEM micrographs for a) neat PE, b) PE/O-MMT and c) PE/O-MMT/PE-MA 55

Figure 3.5 Relative permittivity ε' (a) and dielectric loss ε'' (b) versus frequency at various temperatures observed for the neat PE blend 57

Figure 3.6 Relative permittivity ε' (a) and dielectric loss ε'' (b) for PE/O-MMT nanocomposites versus frequency at different temperatures 58

Figure 3.7 Dielectric loss ε'' for PE/O-MMT nanocomposites versus frequency at various temperatures, ...59

Rapport-gratuit.com
LE NUMERO 1 MONDIAL DU MÉMOIRES

Figure 3.8 Dielectric loss ε'' for PE/O-MMT nanocomposites versus frequency at different temperatures with the optimum fitting curves for the Havrialk-Negami equation 59

Figure 3.9 Relative permittivity ε' (a) and dielectric loss ε'' (b) for PE/O-MMT/PE-MA nanocomposites versus frequency at different temperatures 61

Figure 3.10 Relaxation rate f_{max} as a function of inverse temperature for the two relaxation modes observed in PE/O-MMT nanocomposites. The solid lines represent best fits for the Arrhenius function 62

Figure 3.11 Relaxation rate f_{max} as a function of inverse temperature for the MWS relaxation rate observed in PE/O-MMT and PE/O-MMT/PE-MA nanocomposites. The solid lines represent best fits for the Arrhenius function 63

Figure 4.1 Optical microscope images of (a) neat PE, (b) PE/O-MMT and (c) PE/O-MMT/PE-MA 72

Figure 4.2 AFM height images of (a) neat PE, (b) PE/O-MMT and (c) PE/O-MMT/PE-MA 74

Figure 4.3 Low (I) and high (II) magnification TEM images of nanocomposites: (a) PE/O-MMT and (b) PE/O-MMT/PE-MA 76

Figure 4.4 TGA decomposition curves of neat PE and its nanocomposites in air environment 77

Figure 4.5 TGA decomposition curves of neat PE and its nanocomposites in a N_2 environment 78

Figure 4.6 Storage modulus E' of neat PE, PE/O-MMT and PE/O-MMT/PE-MA nanocomposites as function of temperature at 1 Hz 80

Figure 4.7 Loss modulus E'' of neat PE, PE/O-MMT and PE/O-MMT/PE-MA nanocomposites as function of temperature at 1 Hz 81

Figure 4.8 Typical breakdown path for PE/O-MMT in (a) 2D and (b) 3D visualizations, observed by high resolution optical microscope 83

Figure 4.9 Weibull probability plot of dielectric strength of neat PE, PE/O-MMT and PE/O-MMT/PE-MA.....83

Figure 5.1 X-ray diffraction spectrum of LLDPE/clay nanocomposites 94

Figure 5.2 TEM Micrographs of (a) LLDPE+3%O-MMT and (b) LLDPE+3% O-MMT+10% M603 95

Figure 5.3 AFM images of (a) LLDPE+3% O-MMT and (b) LLDPE+3% O-MMT+10% M603 nanocomposites.....96

Figure 5.4 FTIR spectra of of LLDPE and its nanocomposites.....98

Figure 5.5 SEM micrograph of LLDPE+3% O-MMT+10% M603 for a screw speed of (a) 50 rpm and (b) 350 rpm.....99

Figure 5.6 Relative permittivity (a) and dielectric losses (b) as a function of frequency of LLDPE and its nanocomposites at 40°C.....102

Figure 5.7 Weibull probability plot of dielectric strength of LLDPE and its nanocomposites.....102

Figure 6.1 SEM micrograph of (a) PE/O-MMT and (b) PE/O-MMT/PE-MA nanocomposites.....113

Figure 6.2 Unit cell model of a single-inclusion two-component periodic composite material.....114

Figure 6.3 Electric field distribution in the nanocomposite with (a) 1 particle, (b) 8 particles, (c) 27 particles and (d) 64 particles, respectively (ordered distribution) 115

Figure 6.4 Polarization field distribution in the nanocomposites with (a) 1 particle, (b) 8 particles, (c) 27 particles and (d) 64 particles, respectively (ordered distribution).....116

Figure 6.5 Electric field distribution in the nanocomposites with (a) 1 particle, (b) 8 particles, (c) 27 particles and (d) 64 particles, respectively (random distribution) 118

Figure 6.6 Comparison of effective permittivity for random and ordered nanoparticle distributions.....119

Figure 6.7 Comparison of normalized maximum electric field for random and ordered nanoparticle distributions.....119

Figure 6.8 Electric potential distribution in the nanocomposite 121

Figure 6.9 Numerical and theoretical results of the effective permittivity as a function of the dielectric permittivity of inclusion 122

Figure 6.10 Normalized maximum electric field for ordered and random nanoparticle distributions as a function of the dielectric permittivity of inclusion.....122

Figure 6.11 Electric potential distribution in the nanocomposite with 1 particle: (a) ordered distribution and (b) random distribution. The red lines present the electrical field stream lines.....124

Figure 6.12 Variation of the effective permittivity with normalized radius of the spherical nanoclay particles.....125

LISTE DES ABRÉVIATIONS, SIGLES ET ACRONYMES

AFM	Atomic Force Microscopy
ASTM	American Society for Testing and Materials
AC	Alternative Current
C	Carbon
CEC	Capacité d'échange cationique
CNRC	Conseil National de Recherches Canada
CTT	Centre de technologie Thermique
DMTA	Dynamic Mechanical Thermal Analysis
DRX	Diffraction des rayons X
DSC	Calorimétrie Différentielle à Balayage
DP	Décharges Partielles
DC	Direct Current
2-D	Bidimensionnel
3-D	Tridimensionnel
E	Champ électrique constant E
ÉTS	École de Technologies Supérieures
E226	Compatibilisant
FD	Facteur de dissipation
FDS	Frequency Domain Spectroscopy
FR	Flame Retardant
FTIR	Fourier Transform Infrared
H	Hydrogène

HDPE	Polyéthylène à haute densité
HT	Haute Tension
IEC	International Electrotechnical Commission
IEEE	Institute of Electrical and Electronics Engineers
ISO	International Organization for Standardization
IREQ	Institut de Recherche d'Hydro-Québec
LAMSI	Laboratoire sur les alliages à mémoire et les systèmes intelligents
LDPE	Polyéthylène à basse densité
LLDPE	Polyéthylène à basse densité linéaire
MEB	Microscope électronique à balayage
MEF	Méthode des Éléments Finis
MET	Microscope électronique à Transmission
MFI	Melt flow index
MMT	Montmorillonite
M603	Compatibilisant
MW	Molecular Weight
MWS	Maxwell-Wagner-Sillars
N	Azote
NP	Nanoparticule
O	Oxygène
O-MMT	Montmorillonite modifiée organiquement
PP	Polypropylène
P	Polarisabilité

TC	Taux de cristallinité
XLPE	Polyéthylène réticulé

LISTE DES SYMBOLES ET UNITÉS DE MESURE

Unités de Base

kg	kilogramme (masse)
s	seconde (temps)
m	mètre (longueur)
A	ampère (intensité de courante électrique)
K	Kelvin (température)

Volume

m^3	mètre cubique
l	litre

Longueur

m	mètre
mm	millimètre
µm	micromètre
nm	nanomètre
Å	Angstrom

Temps

s	seconde
min	minute
h	heure

Force

N	Newton

Angle

º	degré
rad	radians

Rapport-Gratuit.com

Fréquence

Hz	Hertz
cm^{-1}	centimètre moins un

Puissance

W	watt

Énergie

J	Joule
eV	électron volt

Densité

g/cm^3	gramme par centimètre cubique

Capacité

F	farad

Tension électrique

V	volt

Champ électrique

$kVmm^{-1}$	kilovolt millimètre moins un

Pulsation de la tension appliquée

rad/s	radians par seconde

Viscosité

Pa.s	Pascal seconde

Concentration

g/mol	gramme par mole
ppm	partie par million

Rapport-gratuit.com
LE NUMERO 1 MONDIAL DU MÉMOIRES

INTRODUCTION

Depuis les années 1970, l'utilisation du polyéthylène réticulé (XLPE), comme isolant électrique, a été généralisée pour les câbles de puissance utilisés pour le transport et la distribution de l'énergie électrique. Ce type de matériaux possède des propriétés thermomécaniques et diélectriques spécifiques, mais les polymères réticulés sont difficilement réutilisables ou recyclable. Ainsi, la perspective de les remplacer par des matériaux plus performants comporte d'énormes avantages, tant économiques qu'environnementaux. Le développement d'une nouvelle famille de polymère nanocomposites à base de polyéthylène avec des propriétés diélectriques et thermomécaniques spécifiques s'inscrit, naturellement, dans cette optique.

Les nanocomposites sont des matériaux assez récents, leur apparition date d'une dizaine d'années. De nombreuses études ont montré que l'incorporation d'un faible pourcentage de charges de tailles nanométriques au sein d'un polymère, conduit souvent à une amélioration significative de ses propriétés mécaniques, diélectriques et optiques, ainsi que de sa résistance au feu. Sa perméabilité au gaz se trouve également modifiée, lorsqu'elle est comparée à celle de la matrice polymère pure (Chiu, Yen et Lee, 2010; Dumont et al., 2007; Guastavino et al., 2010; Han et al., 2001; Hotta et Paul, 2004; Kawasumi et al., 1997; Lai, Chen et Zhu, 2009; Lertwimolnun et Vergnes, 2005; López-Quintanilla et al., 2006; Pereira de Abreu et al., 2007; Sanchez-Valdes et al., 2009; Thelakkadan et al.; Utracki et Kamal, 2002; Venkatesh et al., 2012; Villanueva et al., 2009). Les domaines d'application des matériaux nanocomposites sont larges, elles s'étendent de l'isolation électrique haute tension, à l'industrie aéronautique, en passant par l'industrie automobile, etc.

Ce projet se focalise sur les nanocomposites polyéthylène renforcés par des nanocharges à base d'argile lamellaire de type montmorillonite modifiée organiquement (MMT-O). Un des avantages majeurs relatifs à l'utilisation de l'argile, tient du fait de son abondance comme ressource naturelle, ainsi que de son exploitation aisée sur différents sites du monde. Les feuillets argileux individuels ont des épaisseurs de l'ordre du nanomètre, avec des largeurs et longueurs de plusieurs centaines de nanomètres. Le challenge, ici, consiste à séparer ces

feuillets argileux et à optimiser leurs dispersions dans la matrice du thermoplastique afin d'accroitre la surface de contact entre la matrice polymère et le renfort.
Ce travail de thèse s'inscrit, justement, dans cette optique qui consiste à contribuer à optimiser le procédé de dispersion des charges nanoargiles dans une matrice de polyéthylène. En particulier, dans un premier temps, les effets des conditions opératoires ainsi que ceux relatifs à la formulation sont étudiés. Ensuite, la corrélation entre la structure du nanocomposite en question et ses propriétés thermiques, thermomécaniques et diélectriques est analysée. Finalement, un modèle de simulation 3D par éléments finis, permettant de prévoir la permittivité diélectrique des nanocomposites, est développé et les résultats sont comparés à ceux issus de modèles théoriques classiques.
Notons que le but principal de ce travail, est d'évaluer la contribution que peut apporter ce type de matériau dans l'industrie des isolants électriques et très particulièrement les câbles de puissance.

Ce mémoire de thèse se divise en cinq parties.
Le premier chapitre, à caractère bibliographique, est consacré aux nanoargiles, à la présentation des différentes techniques d'élaboration des nanocomposites, ainsi que de la relation entre leurs structures et leurs propriétés.

Dans le second chapitre, nous présentons les matériaux utilisés au cours de cette thèse, ainsi que la méthodologie employée pour évaluer l'état de dispersion, et pour caractériser les propriétés du polymère nanocomposite.

Le troisième chapitre est consacré à l'étude de l'effet des nanoargiles et de l'agent compatibilisant sur la structure, ainsi que sur la réponse diélectrique du polymère nanocomposite.

Dans le quatrième et cinquième chapitre, nous étudions la relation entre la structure et la résistance au claquage diélectrique du polyéthylène/nanoargile.

Dans le sixième chapitre, nous présentons la simulation et la modélisation de la permittivité effective, et également de la distribution du champ électrique dans les nanocomposites polyéthylène /argile.

Enfin, une conclusion générale et des recommandations achèvent ce mémoire de thèse.

CHAPITRE 1

ÉTAT DE L'ART

1.1 Argiles lamellaires comme renfort

Parmi les renforts les plus utilisés dans les matériaux nanocomposites, on trouve la montmorillonite. Il s'agit d'une argile naturelle qui fait partie de la famille des smectites. Comme schématisée sur la Figure 1.1 (Gloaguen et Lefebvre, 2007), la montmorillonite est structurée à différentes formes : feuillet, particule élémentaire et particules agrégées.

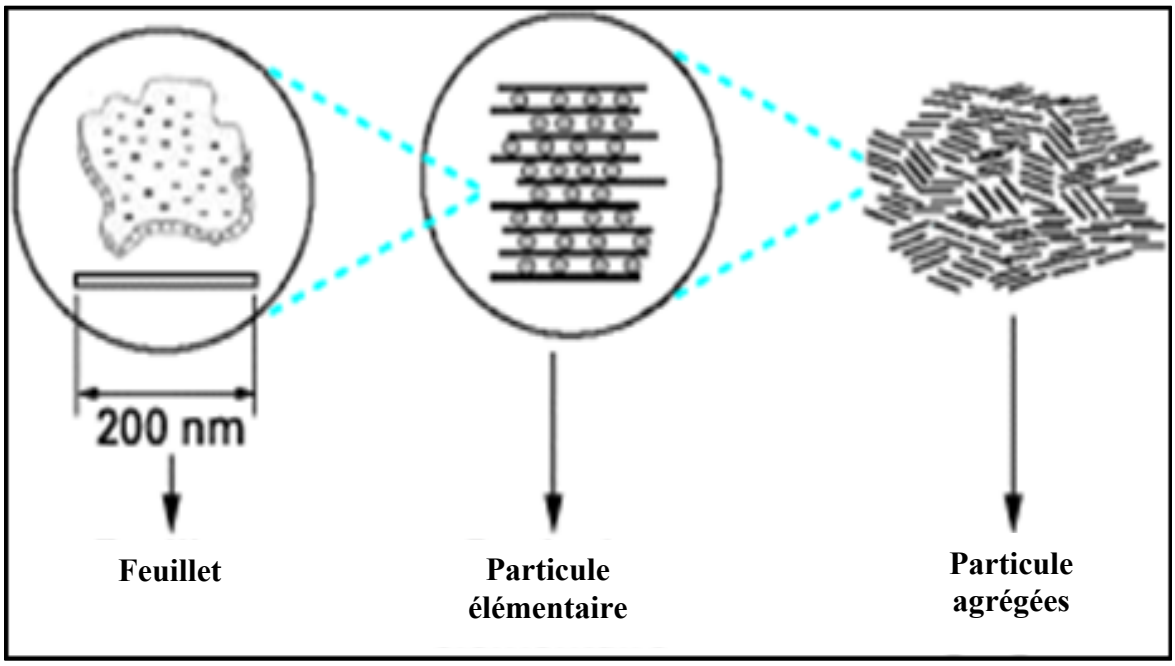

Figure 1.1 Schéma de différentes échelles d'une particule de montmorillonite
Tirée de Gloaguen and Lefebvre (2007, p.4)

L'argile de type montmorillonite est sans doute le plus utilisé pour le renforcement de polymères. Ce matériau inorganique plaquettaire possède, en fait, une surface spécifique élevée et une force électrostatique faible, facilitant ainsi la modification par échange cationique.

1.1.1 Structure cristallographique de la montmorillonite

La structure cristallographique de la montmorillonite (MMT) (illustrée sur la Figure 1.2), montre que MMT est constitué d'une couche d'octaèdres d'alumine comprise entre deux couches de tétraèdres de silice. La dimension latérale d'un feuillet élémentaire de montmorillonite est d'une centaine de nanomètres, avec une faible épaisseur de l'ordre du nanomètre. Les feuillets argileux de MMT sont reliés entre eux par des forces de type électrostatiques et de type Van der Waals (Gloaguen et Lefebvre, 2007).

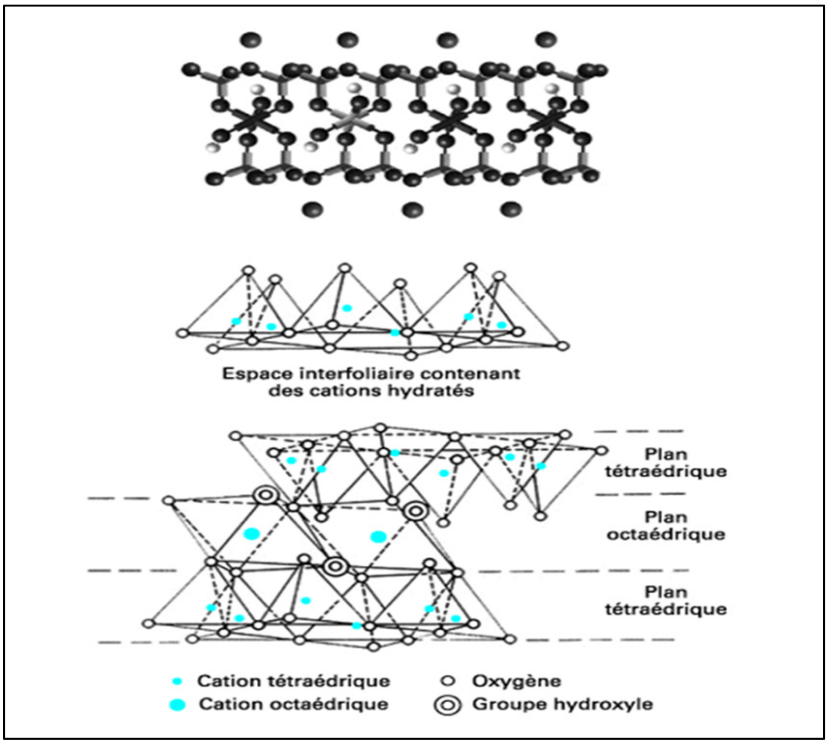

Figure 1.2 Représentation de la structure de montmorillonite
Tirée de Gloaguen and Lefebvre (2007, p.4)

1.1.2 Traitement organophile de la montmorillonite

La montmorillonite présente une certaine affinité pour l'eau, elle est à ce titre hydrophile. Par ailleurs, la majorité des polymères sont hydrophobes. Cette incompatibilité entre le renfort et la matrice rend la dispersion des feuillets de la montmorillonite dans une matrice de polymère très difficile. De ce fait, un traitement organophile de surface est nécessaire. La modification, engendrée par ce dernier, se fait par un échange cationique qui vise à substituer les cations inorganiques par des cations organiques, appelés agents d'interface ou tensioactifs.

Les tensioactifs possèdent deux parties de polarités différentes. Une partie hydrophile compatible avec la surface des feuillets argileux, et une partie hydrophobe constituée par des chaines alkyle, le plus souvent des ions de type alkyle ammonium. La Figure 1.3 présente quelques exemples de tensioactifs utilisés pour modifier organiquement les argiles (Lertwimolnun, 2006).

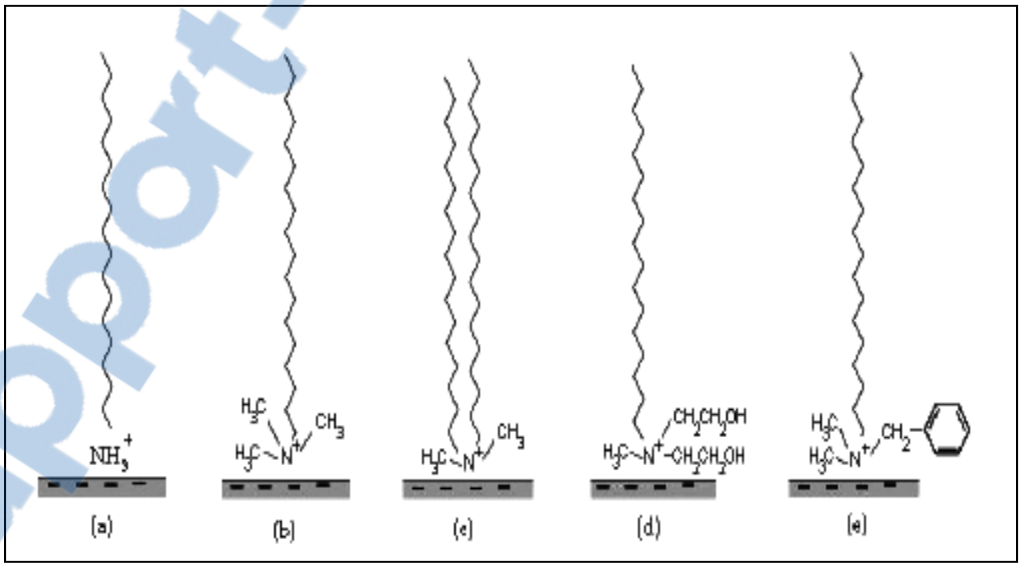

Figure 1.3 Schématisation des exemples de tensioactifs :
(a) Alkylammonium (b) Alkyltriméthylammonium
(c) Dialkyldiméthylammonium
(d) Alkylbis(2-hydroxyéthyl)méthylammonium
(e) Alkylbenzyldiméthylammonium
Tirée de Lertwimolnum (2006, p. 12)

Rapport-Gratuit.com

Les caractérisations structurelles, par la technique de diffraction des rayons X, des argiles organo-modifiés (Figures 1.4 et 1.5), montrent que la distance interlamellaire d_{001} augmente avec la longueur (Lertwimolnun, 2006) et la concentration (Zhao et al., 2003) des tensioactifs.

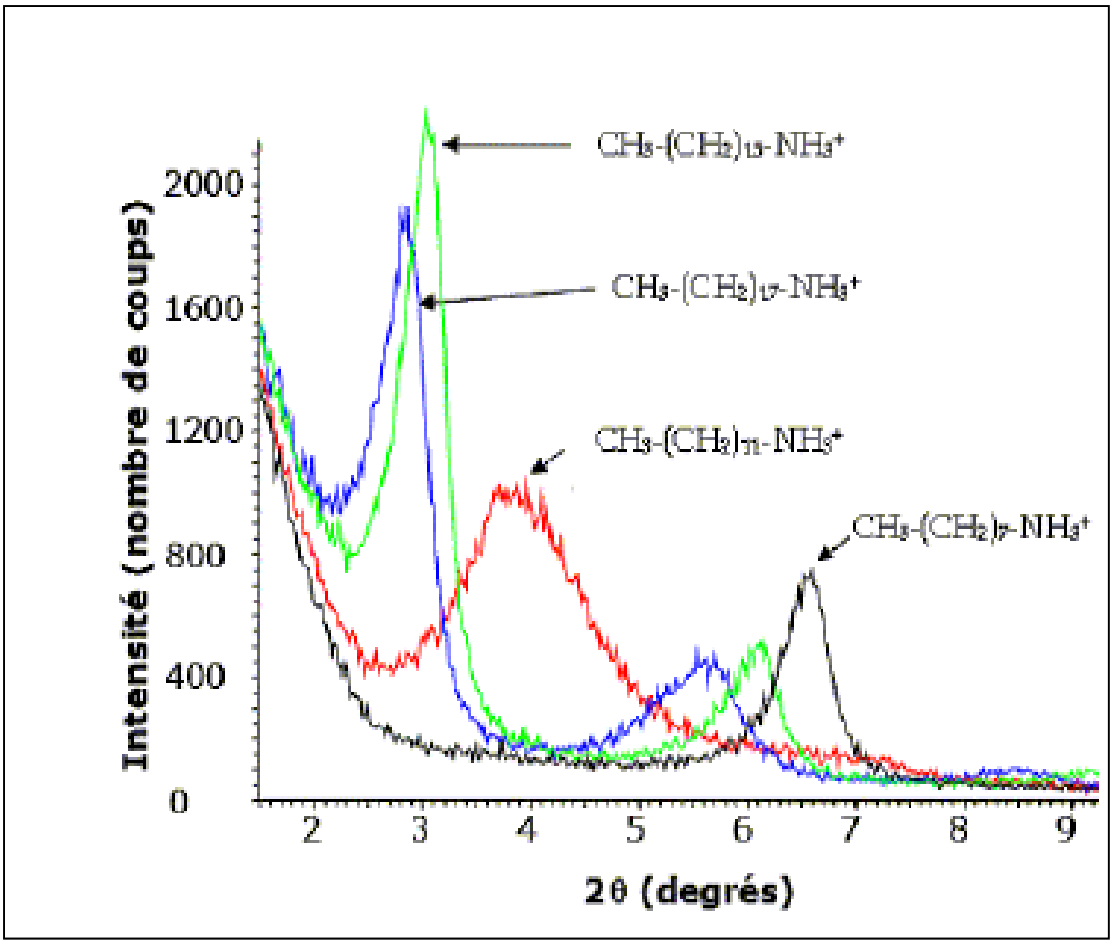

Figure 1.4 Variation de la distance interlamellaire d_{001} en fonction de la longueur de chaîne Alkyle
Tirée de Lertwimolnum (2006, p. 13)

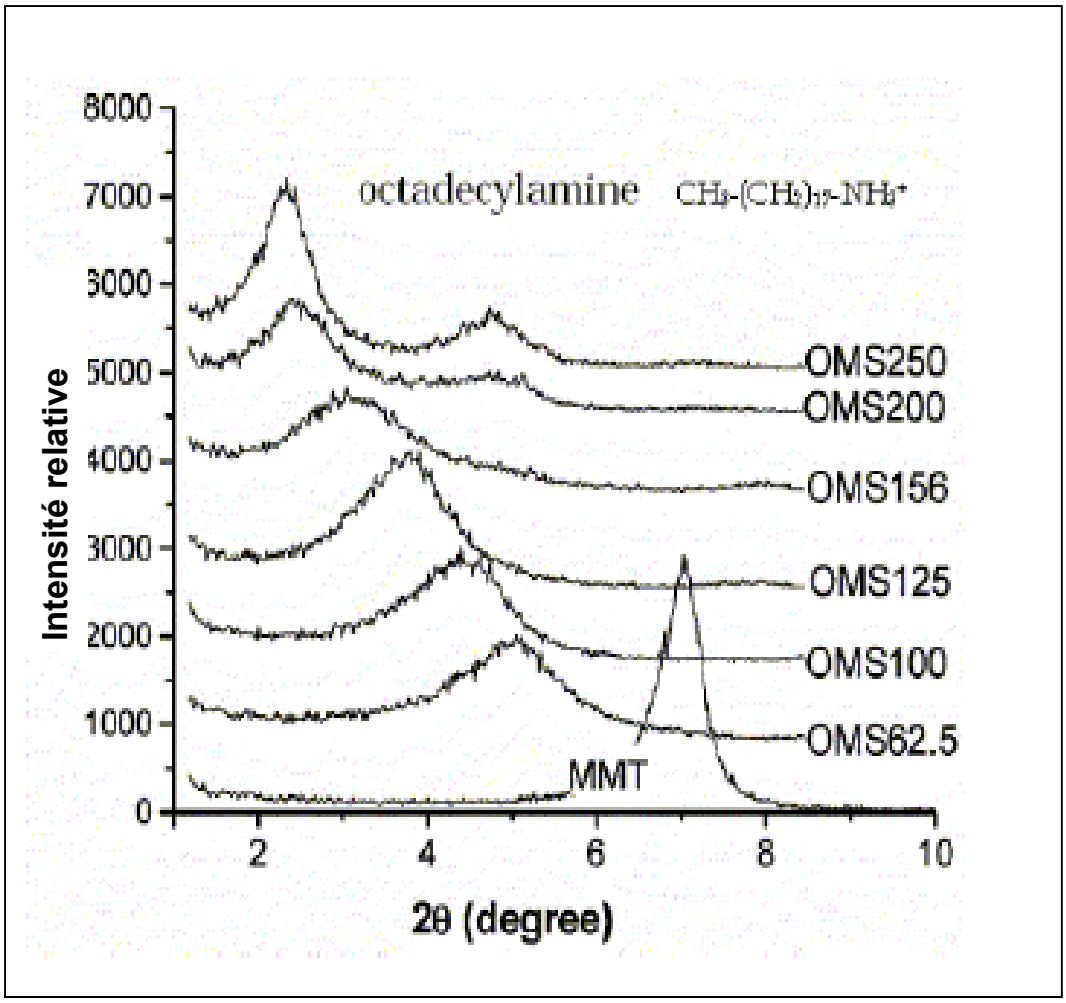

Figure 1.5 Évolution de la distance interlamellaire d_{001} en fonction de la concentration d'agent d'interface
Tirée de Zhao (2003, p. 9262)

Par ailleurs, Lagaly (Lagaly, 1981; 1986) a proposé 4 modèles pour étudier la relation entre la distance interlamellaire et l'orientation des chaines alkyle dans l'espace entre les feuillets d'argile comme il est illustré sur Figure 1.6 (de Paiva, Morales et Valenzuela Díaz, 2008).

Rapport-gratuit.com
LE NUMERO 1 MONDIAL DU MÉMOIRES

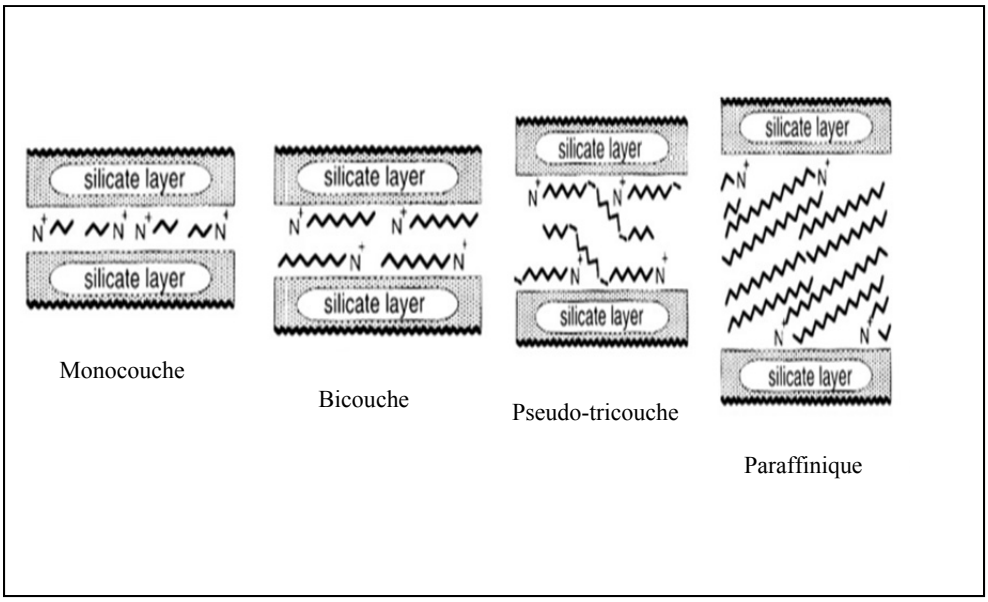

Figure 1.6 Orientations des chaînes hydrocarbonées dans l'espace entre les feuillets d'argile
Tirée de de Paiva (2008, p. 10)

1.2 Polymères thermoplastiques comme matrice

Parmi les thermoplastiques semi-cristallins les plus étudiés, comme matrice organique utilisée dans l'élaboration des matériaux nanocomposites, on trouve le polyéthylène et le polypropylène. Ces deux thermoplastiques font partie de la famille des plastiques courants et qui représentent plus 90 % des plastiques consommés. Le succès de ces polymères s'explique par leur faible coût et leurs vastes domaines d'application: l'emballage (film, accessoire ménager), l'électronique (isolation de câbles électriques), l'automobile (réservoirs à essence d'automobiles…) et la construction (aspect pierre, dalles, Tube.).

Dans le domaine de l'isolation électrique à haute tension, le polyéthylène constitue un matériau de choix grâce à son hydrophobicité, couplée à une bonne tenue aux contraintes climatiques. Ce polymère, qui possède une bonne tension de claquage et une bonne stabilité thermique, est classé comme un excellent diélectrique.

La description de la structure du polyéthylène est décrite par cinq échelles différentes (Figure 1.7 (Douminge, 2010)). On distingue d'abord la structure moléculaire (*échelle 1*), où la

macromolécule est constituée d'une chaîne principale, sur laquelle des molécules (ou atomes) sont substitués de façon régulière, la structure conformationnelle (*échelle II*), dans laquelle la chaîne macromoléculaire est arrangée d'une façon spatiale, la structure des états cristallins et amorphes (*échelle III*), l'arrangement de la phase amorphe et des cristaux sous forme de sphérolites (*échelle IV*), et enfin, l'échelle macroscopique (*échelle V*).

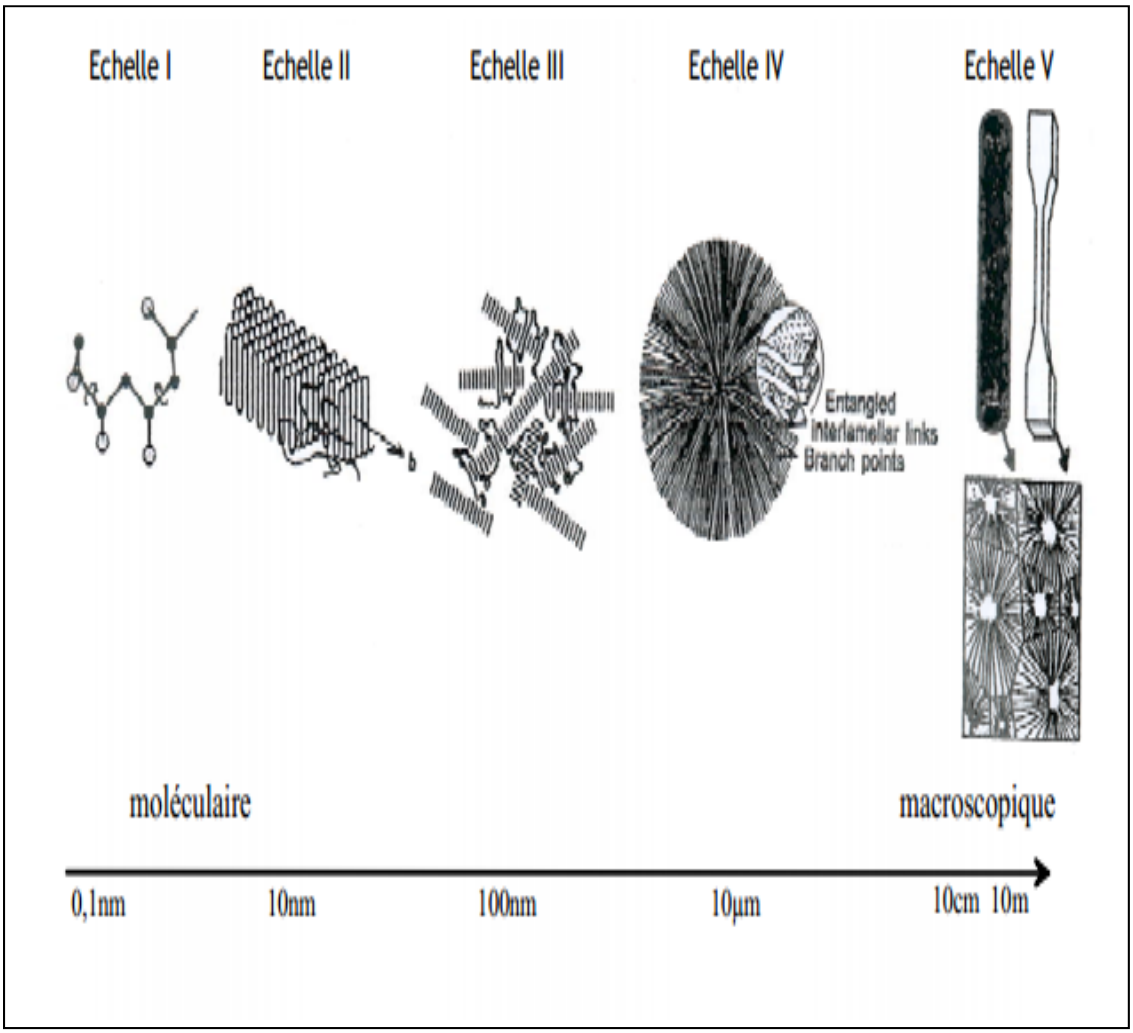

Figure 1.7 Représentation de la description multi-échelles du polyéthylène
Tirée de Doumige (2010, p. 8)

1.3 Nanocomposites

1.3.1 Définition

Les matériaux nanocomposites sont constitués de renforts dont les dimensions sont de l'ordre du nanomètre, et d'une matrice qui protège ces renforts et leur transmet les efforts mécaniques. En fait, l'ajout de renforts nanométriques dans une matrice polymère permet d'améliorer ses propriétés mécaniques, diélectriques, thermiques et optiques.

1.3.2 Interphase

L'aire spécifique de l'interface (matrice/ renfort) est très élevée dans les nanocomposites. Cette interface peut modifier les propriétés de la matière (Utracki et Kamal, 2002). La Figure 1.8 (Lewis, 2004) représente la variation du volume du renfort A occupé par l'interphase AB en fonction du diamètre du renfort A dans la matrice B.

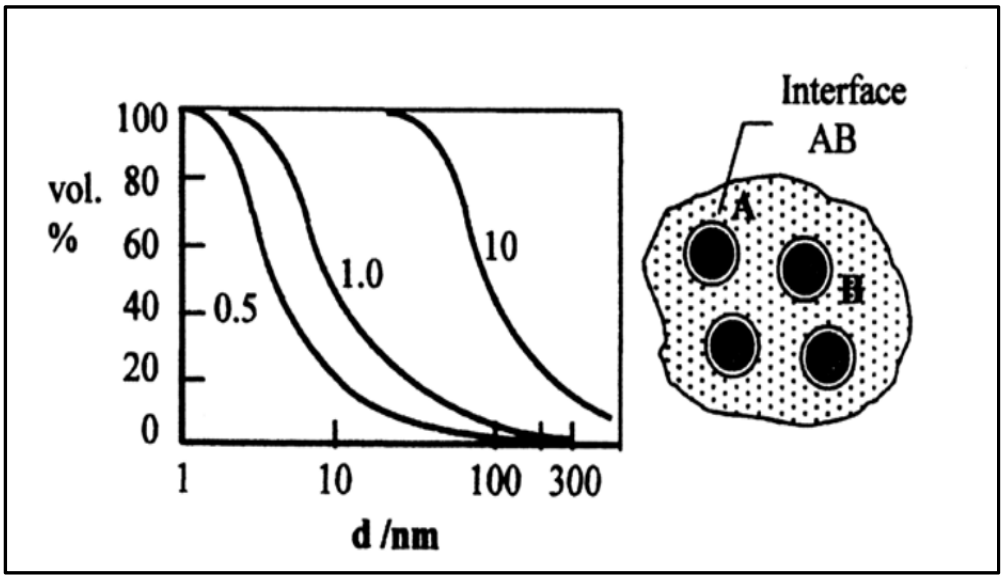

Figure 1.8 Évolution du pourcentage du volume du renfort A occupé par l'interphase AB en fonction du diamètre du renfort A
Tirée de Lewis (2004, p. 740)

1.3.3 Structure des nanocomposites

Selon la dispersion des renforts argileux au sein de la matrice du polymère, il existe trois catégories de structures (Ambid, 2007):

- Composite conventionnel: lorsque les nanocharges sont dispersées sous forme de particules primaires ou d'agrégats, dont la taille est d'un ordre micrométrique (Figure 1.9 a).
- Composite intercalé: lorsque les nanocharges sont dispersées sous forme de feuillets intercalés par l'insertion des chaînes polymère (d_{001}<8 nm). Cependant, les feuillets argileux ne sont pas complètement séparés (Figure 1.9 b).
- Composite exfolié: lorsque les nanocharges sont dispersées dans la matrice à l'échelle nanométrique (d_{001}>8 nm), les feuillets argileux sont individuellement séparés (Figure 1.9 c). En pratique, cet état exfolié est difficile à obtenir. IL demande un grand contrôle de plusieurs paramètres et à toutes les échelles.

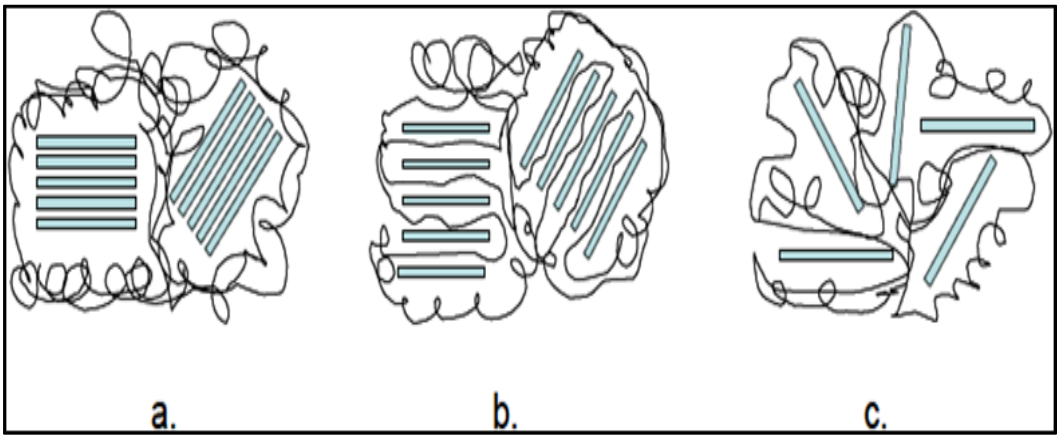

Figure 1.9 Différentes structures de nanocomposites polymère / argile:
(a) Microcomposite; (b) Nanocomposite intercalé; (c) Nanocomposite exfolié
Tirée de Ambid (2007, p. 24)

1.4 Techniques d'élaboration des nanocomposites

On distingue au moins trois méthodes principales de préparation des nanocomposites: La polymérisation in situ, l'intercalation en solution et le mélange à l'état fondu.

1.4.1 Polymérisation in situ

Les premiers nanocomposites élaborés par le procédé de polymérisation in situ ont étés réalisés par les laboratoires de recherche de Toyota. Cette technique est basée sur l'introduction des nanoargiles dans un monomère en solution. Durant la réaction de polymérisation, les monomères diffusent entre les feuillets argileux et les chaines de polymères se développent, ainsi, entre ces derniers (Figure 1.10 (Gloaguen et Lefebvre, 2007)). Cela conduit à une augmentation importante de la distance interlamellaire d_{001}.

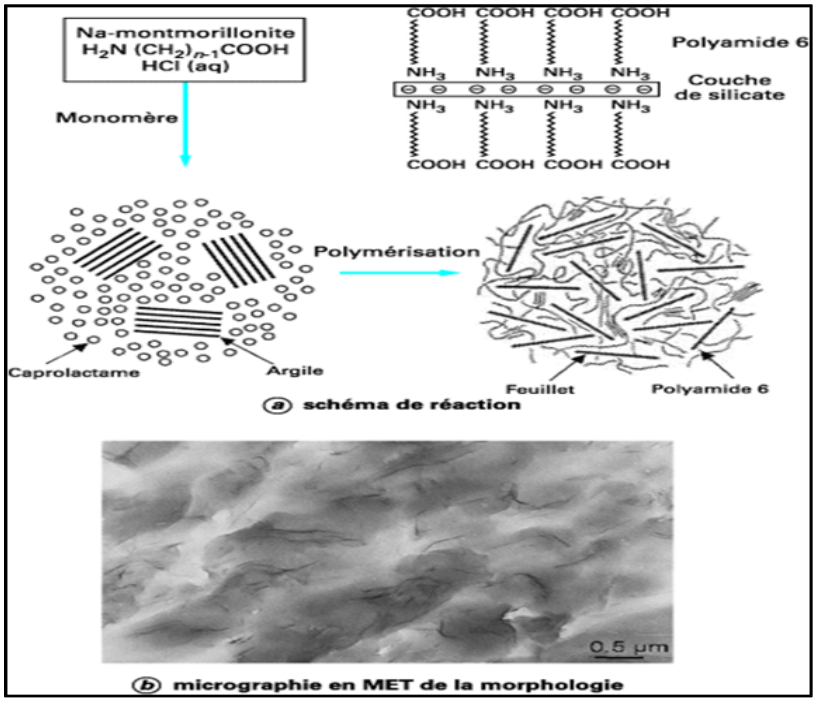

Figure 1.10 Schéma de différentes étapes de la formation du nylon/argile nanocomposites par polymérisations in situ
Tirée de Gloaguen and Lefebvre (2007, p. NM 3050-7)

1.4.1 Intercalation en solution

Cette méthode consiste en l'introduction de l'argile dans un solvant. Le polymère est introduit après le gonflement de l'argile, et à la fin du procédé le solvant est évaporé. Dans cette technique le choix du solvant est un facteur important. Il doit, en fait, être capable à la fois de solubiliser le polymère, et d'exfolier les feuillets argileux (Figure 1.11 (Gloaguen et Lefebvre, 2007)).

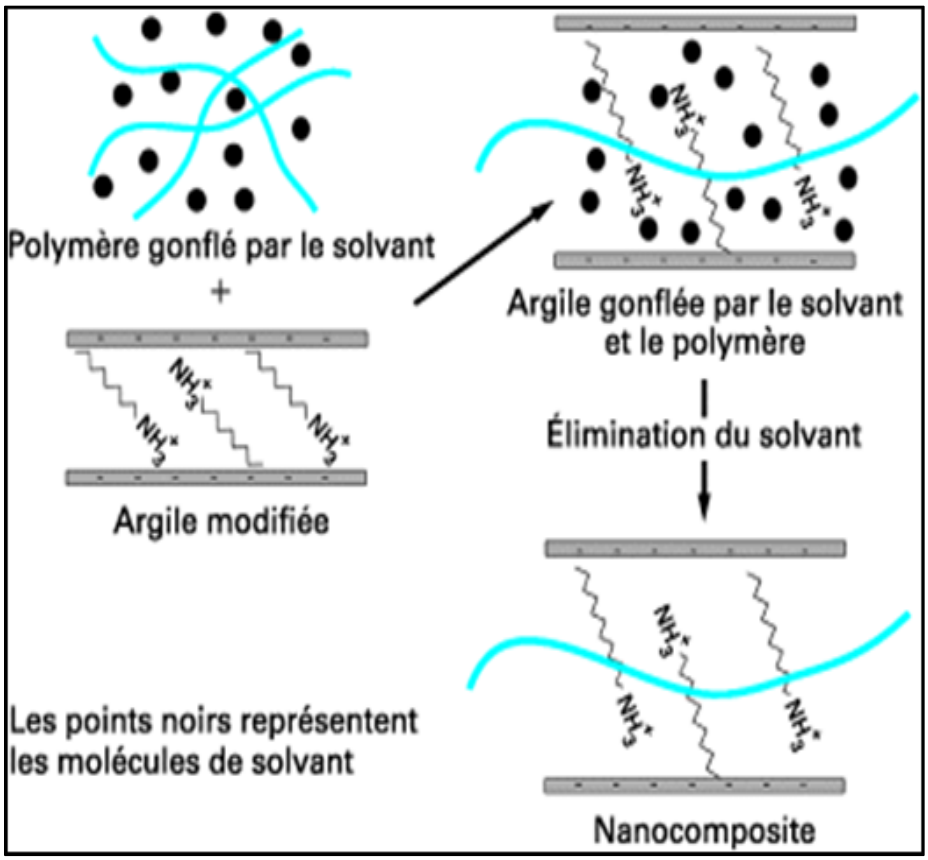

Figure 1.11 Formation de nanocomposites par mélange en solution
Tirée de Gloaguen and Lefebvre (2007, p. NM 3050-8)

1.4.2 Mélange à l'état fondu

Dans cette technique l'argile est directement mélangée avec le polymère à l'état fondu (Figure 1.12 (Gloaguen et Lefebvre, 2007)). En fait, cette méthode comporte d'énormes avantages économiques et environnementaux, puisqu'elle n'utilise pas le solvant, et le procédé habituel de mise en œuvre des polymères n'est pas modifié ou changé. Dans le cadre de ce travail, la technique du mélange à l'état fondu est employée pour élaborer de nanocomposite de polyéthylène en utilisant une extrudeuse bivis.

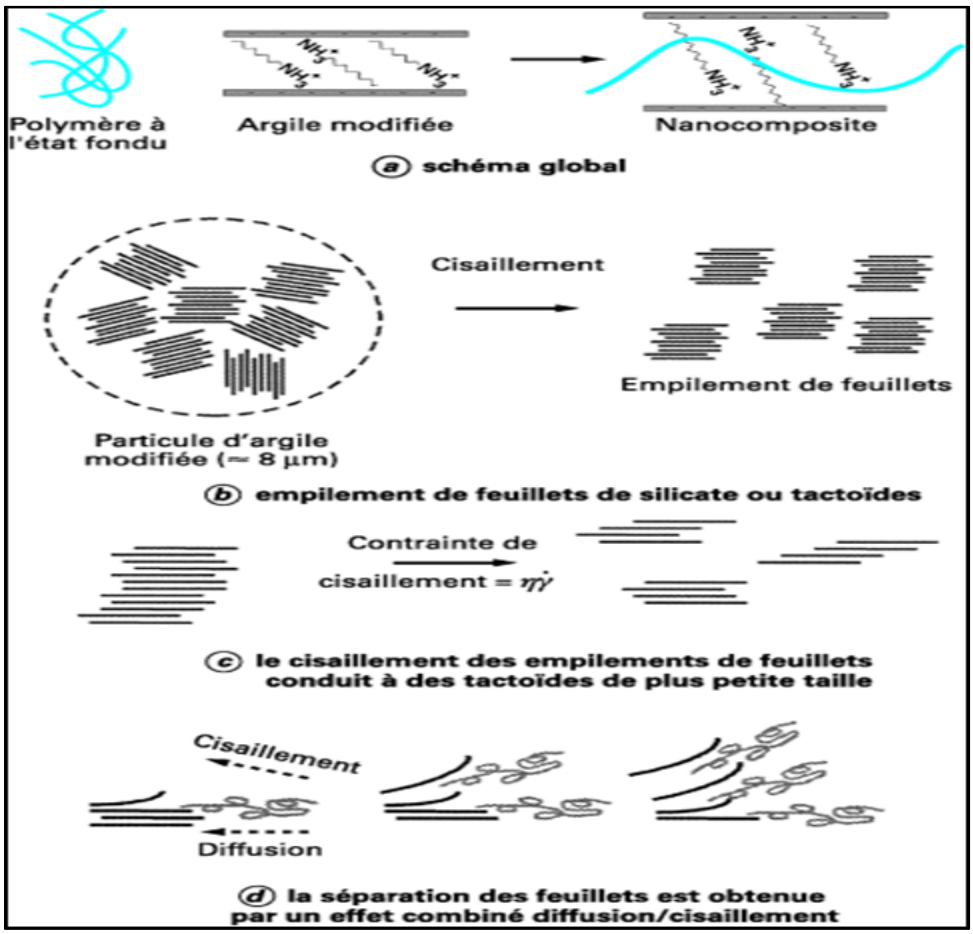

Figure 1.12 Schéma de l'élaboration de nanocomposites par mélange à l'état fondu
Tirée de Gloaguen and Lefebvre (2007, p. NM 3050-9)

1.5 Compatibilisation des nanocomposites

Szasdi et al. (Százdi et al., 2005) ont réalisé des nanocomposites de polymère par la technique du mélange à l'état fondu, et ont utilisé comme compatibilisant, le polypropylène greffé anhydride maléique (PP-g-MA). Ces auteurs ont expliqué l'existence d'une interaction entre le surfactant et le groupement anhydride maléique. Par ailleurs, Xu et al. (Xu et al., 2003) ont étudié l'effet des taux de greffage sur l'amélioration de l'intercalation entre les feuillets d'argile. D'autres auteurs, comme K.H. Wang et al (Wang et al., 2001), ont étudié l'influence du taux de greffage dans des nanocomposites LLDPE-g-MAH/O-MMT, et ont observé que l'exfoliation a lieu lorsque le taux de greffage est suffisamment supérieur à 0.1 % (Figure 1.13 (Wang et al., 2001)). M. Kato et al (Kato, Usuki et Okada, 1997), quant à eux, ils ont étudié le cas du polypropylène modifié. Ils ont, ainsi, proposé un mécanisme qui explique que la comptabilisation est initiée par l'adsorption des greffons polaires du polypropylène modifié par la surface de l'argile, et par la suite toute la chaîne polymère est entraînée entre les feuillets argileux, ce qui conduit à une augmentation de la distance interlamellaire.

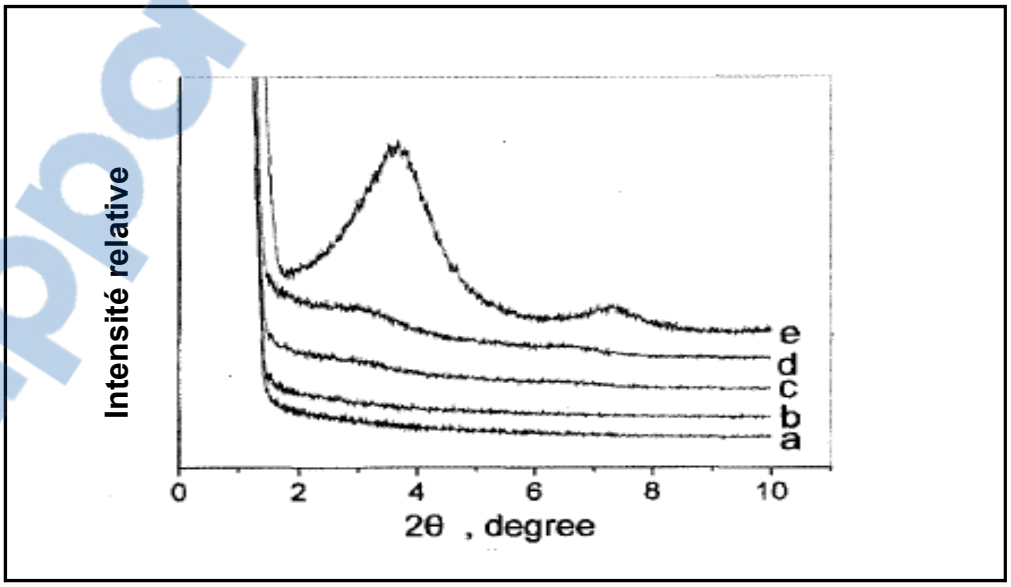

Figure 1.13 Effet du taux de greffage sur l'état de dispersion dans les nanocomposites LLDPE-g-MAH+5 wt % Closite 20A:

Rapport-Gratuit.com

(a) 0.29 wt %, (b) 0.22 wt %, (c) 0.11 wt %, (d) 0.07 wt %, (e) Closite 20A
Tirée de Wang (2001, p. 9824)

1.6 Propriétés mécaniques

Face aux composites conventionnels, de nombreuses recherches ont montré que les matériaux nanocomposites peuvent présenter des propriétés mécaniques améliorées. La présence des nanocharges lamellaires à la place des renforts traditionnels, conduit à une augmentation de rigidité et de la limite élastique à des taux de renfort encore plus bas. Un exemple de composites, souvent utilisé dans les industries automobiles, est le nylon 6 renforcé par de talc ou du verre de taille micrométrique. Comme illustré sur la Figure 1.14 (Yasue et al., 2000), il est clair que le polymère renforcé par des nanocharges, plutôt que par de microcharges, montre des propriétés mécaniques intéressantes, et pour des taux de charge faibles.

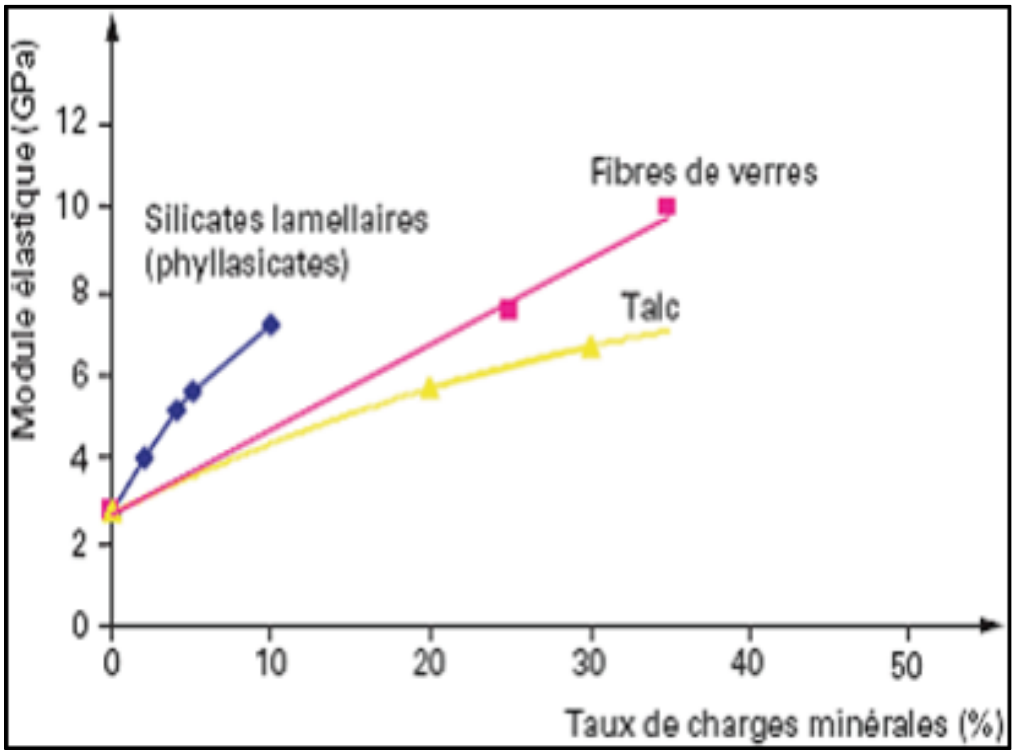

Figure 1.14 Influence du taux de charges minérales sur le module d'élasticité du Nylon 6
Tirée de Perez (2008, p. 39)

1.7 Propriétés thermomécaniques

Les propriétés thermomécaniques de différents types de polymères tels que le polydiméthylsiloxane (PDMS), le polystyrène (PS), le poly(méthyle méthacrylate) (PMMA) et le poly(4–vinylepyridine) (P4VP), ont été étudiées par Tsagaropoulos et Eisenberg (Tsagaropoulos et Eisenburg, 1995). La Figure 1.15 montre la présence de deux relaxations. La première a été reliée à la transition vitreuse, quant à la seconde relaxation, elle a été attribuée à des phénomènes de diffusion des chaînes polymères. On remarque clairement que l'intensité du pic diminue lorsque le taux des nanocharges augmente. Ceci peut être expliqué par le fait que la forte interaction entre le polymère et les nanoparticules limite la mobilité des chaînes polymères.

Pour conclure, il est évident que la microstructure a un effet sur les propriétés thermomécanique des nanocomposites.

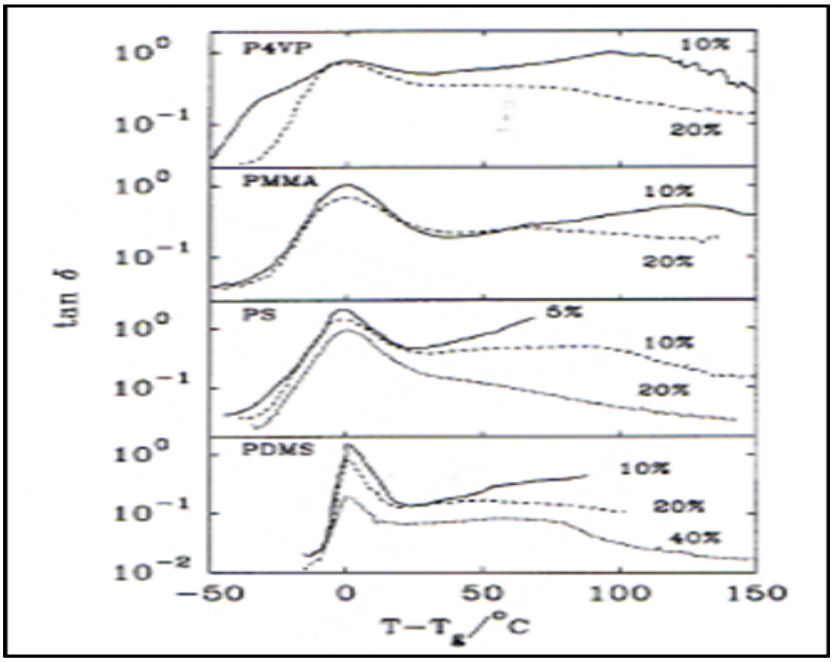

Figure 1.15 Évolution du tan (δ) en fonction de (T-Tg) pour différents nanocomposites avec différents taux de charge de silice
Tirée de Perez (2008, p. 40)

Rapport-gratuit.com
LE NUMERO 1 MONDIAL DU MÉMOIRES

1.8 Stabilité thermique

La stabilité thermique améliorée des matériaux nanocomposites est une propriété importante. Elle est mesurée par analyse thermogravimétrique (TGA). Cette technique consiste à mesurer l'évolution de la perte de masse de l'échantillon en fonction de l'augmentation de la température.

De nombreux travaux ont remarqué une amélioration de la tenue au feu des nanocomposites par rapport aux matrices polymères correspondantes. Certains auteurs, comme Qiu et al. (Qiu, Chen et Qu, 2006), ont étudié le cas du polyéthylène. Ils ont remarqué que l'ajout du MMT à la matrice vierge de polyéthylène augmente la température de décomposition du nanocomposite correspondant. La Figure 1.16 (Qiu, Chen et Qu, 2006) montre l'effet du taux de nanocharges argileuses sur la température de décomposition des nanocomposites LLDPE/MMT. Cette amélioration de la stabilité thermique a été, également, observée dans de nombreux types de nanocomposites (Wen et Wilkes, 1996; Zhu et al., 1999).

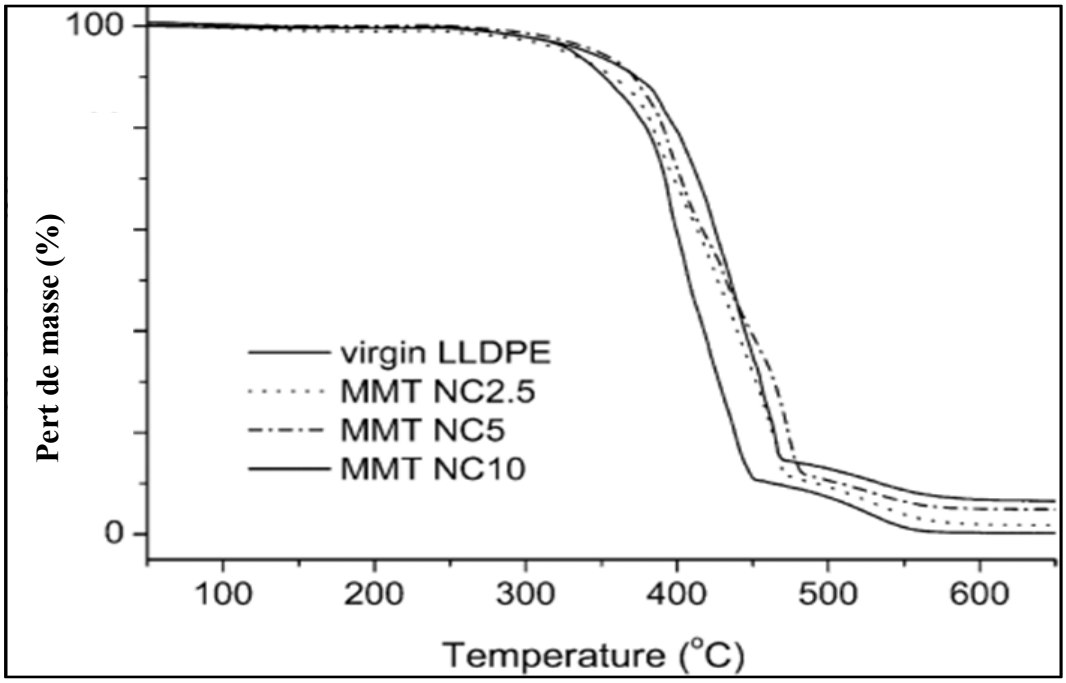

Figure 1.16 Évolution de la température de décomposition des nanocomposites LLDPE/MMT en fonction de taux de charge de MMT
Tirée de Qiu (2006, p. 926)

1.9 Propriétés diélectriques

Les diélectriques sont largement utilisés dans le domaine de l'isolation électrique. Notons, au passage; qu'un diélectrique est dit idéal si sa structure ne comporte pas de charges libres, tandis qu'un diélectrique réel en contient. Au niveau macroscopique un matériau diélectrique est caractérisé par sa constante diélectrique ε. Au niveau microscopique, il n'a que des charges dites liées. Ces dernières ne participent pas à la conduction à cause de leur mobilité qui est entravée, mais elles peuvent se déplacer sur de courtes distances sous l'effet du champ électrique: c'est la polarisation, qui est à l'origine de la permittivité des diélectriques.

1.9.1 Permittivité diélectrique

La polarisation P et le champ électrique E sont reliés, à travers la susceptibilité électrique χ du diélectrique, par la relation

$$P = \varepsilon_0 \chi E \tag{1.1}$$

où ε_0 est la permittivité du vide qui vaut $8.854.10^{-12}$ $F.m^{-1}$. L'induction électrique D d'un diélectrique, peut être exprimée par la relation

$$D = \varepsilon_0 E + P \tag{1.2}$$

Pour un champ électrique variable dans le temps on peut réécrire l'équation (1.2) tel que

$$D(t) = \varepsilon_0 E(t) + P(t) \tag{1.3}$$

On peut définir la fonction de réponse diélectrique f(t) qui représente la réponse d'un milieu diélectrique à une excitation électrique spécifique. Pour chacune des impulsions, on peut faire

la somme de toutes les polarisations et par la suite la polarisation peut s'exprimer sous la forme d'une convolution suivante

$$P(t) = \varepsilon_0 \int_0^{\infty} f(\tau)E(t-\tau)d\tau \tag{1.4}$$

La densité de courant totale J(t) traversant le diélectrique est donnée par l'équation (David, 2010)

$$J(t) = \sigma_c E(t) + \frac{\partial D(t)}{\partial t} \tag{1.5}$$

ou encore

$$J(t) = \sigma_c E(t) + \varepsilon_0 \frac{\partial}{\partial t}[E(t) + \int_0^{\infty} \mathrm{f}(\tau)\mathrm{E}(\mathrm{t}-\tau)\mathrm{d}\tau] \tag{1.6}$$

où σ_c est la conductivité du diélectrique.

Pour exprimer l'équation (1.6) dans le domaine des fréquences, il suffit d'appliquer la transformée de Fourier aux deux membres de l'équation. On a alors

$$J^*(\omega) = [\sigma_c + i\omega\varepsilon_0(1 + F^*(\omega))]E^*(\omega) \tag{1.7}$$

avec $F^*(\omega)$, la transformée de Fourier de f(t) définit tel que

$$F^*(\omega) = \int_0^{\infty} f(t)\exp(-i\,\omega t)dt \tag{1.8}$$

Cette fonction correspond donc à la transformée de Fourier de la susceptibilité. On a donc

$$\mathrm{F}^*(\omega) = \chi^*(\omega) = \chi'(\omega) - \mathrm{i}\chi''(\omega) \tag{1.9}$$

Plus explicitement, on peut réécrire l'équation (1.7) tel que

$$J(\omega) = [\sigma_c + i\omega\varepsilon_0(1 + \chi'(\omega) - i\chi''(\omega))]E^*(\omega) \tag{1.10}$$

ou encore

$$J(\omega) = [\sigma_c + \omega\varepsilon''(\omega) + i\omega\varepsilon'(\omega)]E(\omega) \tag{1.11}$$

dans laquelle on a posé

$$\varepsilon_0\big(1 + \chi'(\omega) - i\chi''(\omega)\big) = \varepsilon'(\omega) - i\varepsilon''(\omega) = \varepsilon^*(\omega) \tag{1.12}$$

χ' et χ'' sont les susceptibilités électriques réelles et imaginaires du milieu, et ε^* la permittivité complexe.

1.9.2 Mécanismes de polarisation

L'application d'un champ externe va entraîner la superposition de quatres mécanismes de polarisation (DUBOIS, 1998):

- La polarisation électronique : c'est lorsque sous l'effet d'un champ électrique E constant, le nuage électronique dans chaque atome a tendance à se déplacer légèrement par rapport au noyau, donnant lieu à un dipôle induit.
- La polarisation moléculaire: cette polarisation a lieu lorsque deux atomes sont liés par une liaison de valence, c'est l'atome possédant la plus grande électronégativité qui attire le plus le doublet électronique, et sera par conséquent chargé négativement. Tandis que l'autre atome portera la charge positive. L'ensemble se comporte, alors, comme un dipôle.
- La polarisation interfaciale: cette polarisation apparait lorsqu'on est en présence de deux matériaux possédant des permittivités et des conductivités différentes. Quand

on met ces matériaux en contact, les charges libres peuvent se concentrer aux interfaces.

- La polarisation d'orientation: Pour une molécule qui possède un moment dipolaires permanent, si on l'applique un champ électrique, cette molécule s'orient dans le sens du champ électrique appliqué.

La Figure 1.17 illustre ces différents types de mécanismes de polarisation.

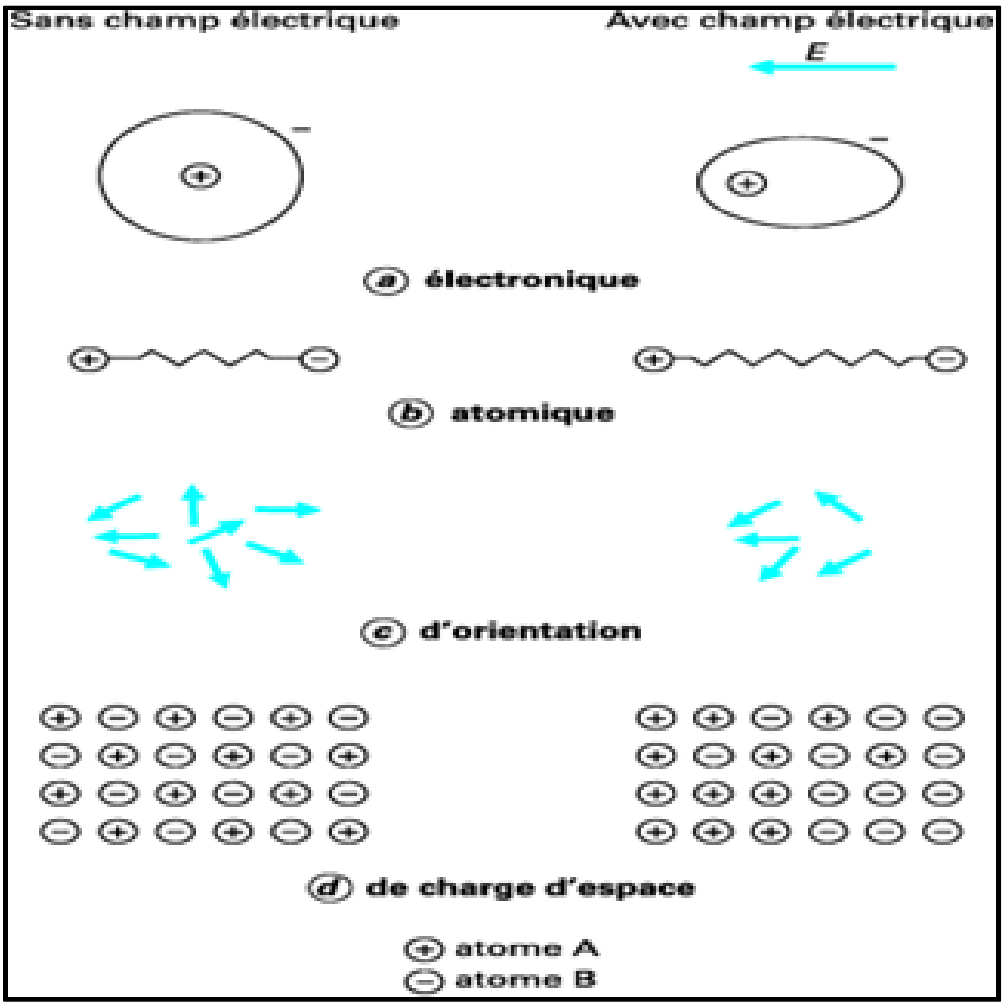

Figure 1.17 Schéma représente les différents types de polarisation
Tirée de Dubois (1998, p. E 1850-4)

1.9.3 Relaxation de Debye

Le modèle de Debye permettant d'exprimé la permittivité diélectrique complexe relie à polarisation d'orientation et intérfaciale est donné par la relation (Debye, Debye et Debye, 1929):

$$\varepsilon^* = \varepsilon_\infty + \frac{\varepsilon_S - \varepsilon_\infty}{1+\omega^2\tau^2} - i\frac{(\varepsilon_S - \varepsilon_\infty)}{1+\omega^2\tau^2} \tag{1.8}$$

où ε_s est la permittivité statique, ε_∞ est la permittivité à fréquence infinie, τ est le temps de relaxation de Debye, et $\omega = 2\ \pi f$ (f étant la fréquence). L'évolution en fonction de la fréquence de la partie réelle et imaginaire de la permittivité diélectrique complexe du modèle de debye est illustrée par la Figure 1.18 (Rigaud, Morucci et Chauveau, 1995).

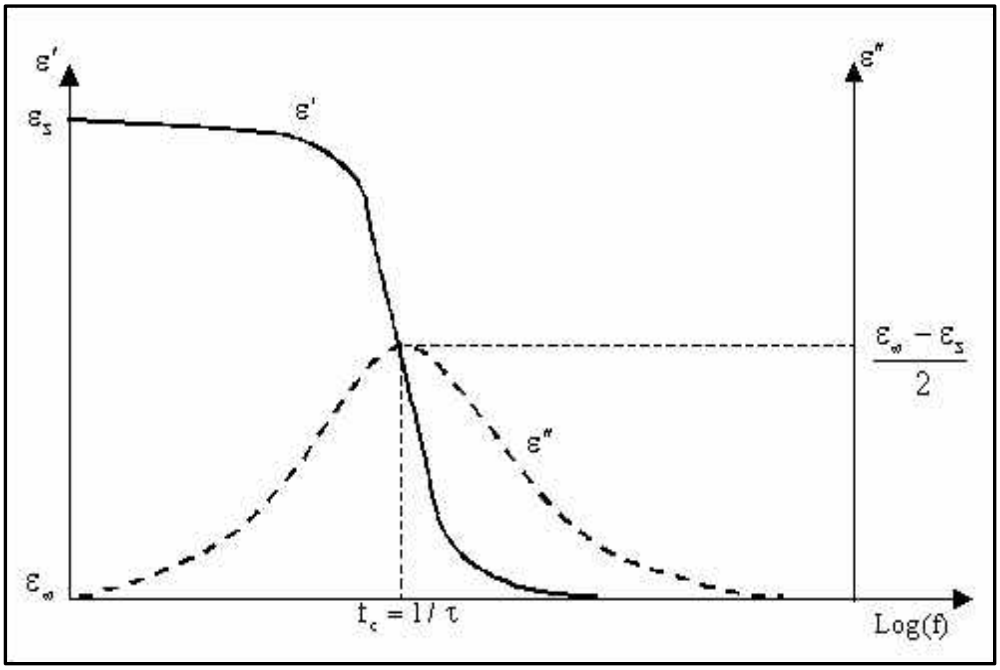

Figure 1.18 Évolution en fonction de la fréquence de la partie réelle
et imaginaire de la permittivité diélectrique complexe
Tirée de Rigaud (1995, p.257)

1.9.4 Relaxation dans les polymères

Dans le cas des polymères, le modèle de Debye n'est pratiquement jamais en accord avec les résultats expérimentaux. Dans ce type des matériaux, le modèle empirique le plus utilisé pour décrire les relaxations diélectriques est celui de Havriliak–Negami (Havriliak et Negami, 1966; 1967). La permittivité diélectrique s'écrit donc sous la forme suivante:

$$\varepsilon(\omega) = \varepsilon_{\infty} + \frac{\Delta\varepsilon}{(1 + (i\omega\tau_{HN})^{\alpha})^{\beta}} \tag{1.9}$$

où $\Delta\varepsilon$ représente la force diélectrique de la relaxation, et ε_{∞} la permittivité à fréquence infinie. τ_{HN} étant le temps de relaxation de Havriliak–Negami, et $\omega = 2\pi f$: la pulsation. α est un paramètre de forme décrivant l'élargissement symétrique des spectres de relaxation. Quant à β, c'est un paramètre exprimant l'élargissement asymétrique des spectres de relaxation. On trouve, dans la littérature, d'autres modèles empiriques décrivant le comportement de la susceptibilité (ou permittivité) complexe (Diaham, 2007).

Tomer a étudié la réponse diélectrique dans les nanocomposites polyéthylène/argile (Tomer et al., 2011), il a remarqué la présence de deux pics de relaxation (Figure 1.19). La relaxation à basse fréquence est attribué à une polarisation de type Maxwell-Wagner-Sillars, tandis que la relaxation détectée à haute fréquence est reliée à la polarisation dite dipolaire. L'auteur a mis en évidence le fait que ces relaxations sont reliées à la présence de l'argile et du comptabilisant, puisqu'aucun pic n'a été détecté dans le cas du polyéthylène vierge.

Des auteurs comme Böhning et al. ont étudié la relation structure-réponse diélectrique, pour le cas des nanocomposites Poly(propylene-*graft*-maleic anhydride)/argile (Böhning et al., 2005). Ils ont trouvé que l'état de la dispersion des feuillets argileux jouait un grand rôle dans la détermination des propriétés diélectriques finales des nanocomposites. Comme le montre clairement la Figure 1.20, il existe une relation entre le degré de dispersion et le taux de relaxation de Maxwell-Wagner-Sillars. En effet, ce paramètre augmente lorsque la qualité de la dispersion des nanoargiles dans la matrice polymère est améliorée. Pour plus de détails, le lecteur est invité à se reporter à l'article # 1 de cette thèse.

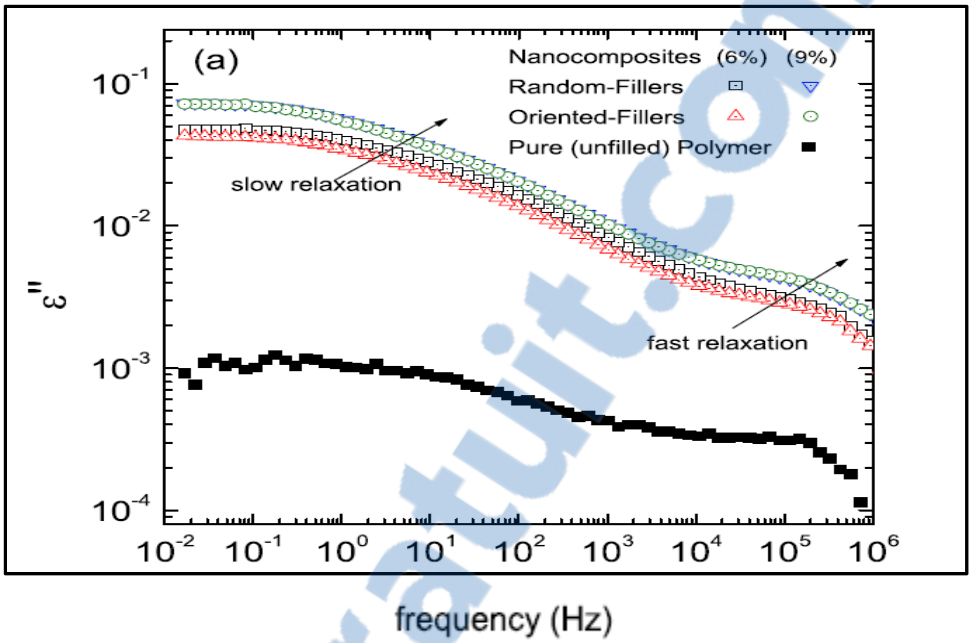

Figure 1.19 Variation de la perte diélectrique ε″ en fonction de la fréquence des systèmes PE et PE/nanoargile nanocomposites à la température ambiante
Tirée de Tomer (2011, p. 074113-6)

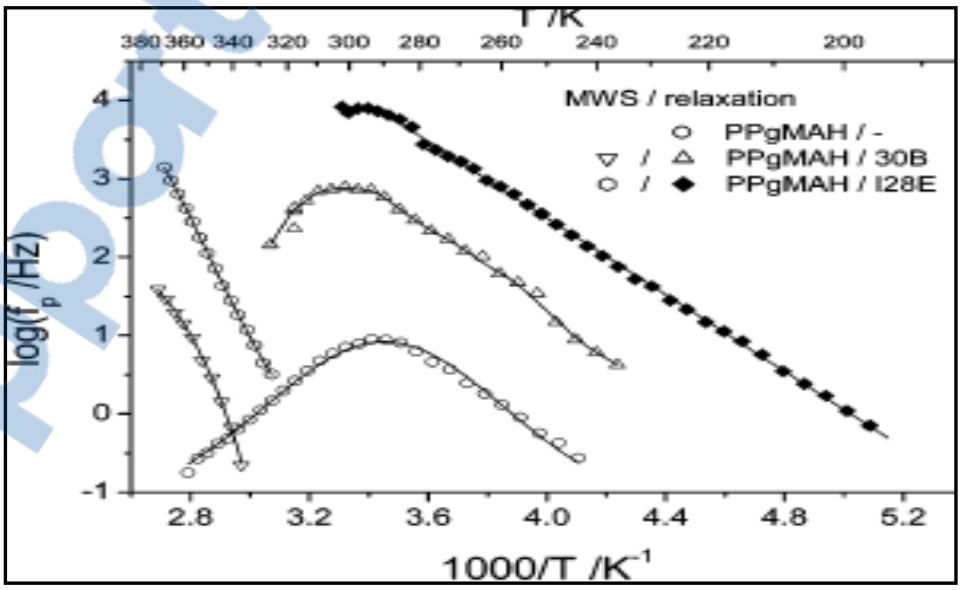

Figure 1.20 Évolution du taux de relaxation en fonction de l'inverse de la température des systèmes Poly(propylene-*graft*-maleic anhydride) et ses nanocomposites
Tirée de Böhning (2005, p. 2772)

Rapport-Gratuit.com

1.9.5 Rigidité diélectrique

La rigidité diélectrique d'un isolant solide diminue avec l'augmentation de la température, de la fréquence, ou de la durée d'application du champ électrique. Notons qu'il existe différents mécanismes de claquage (Barber et al., 2009b). On distingue, d'abord, le claquage intrinsèque (appelé, également, claquage électrique pur), qui se produit sous l'effet des fortes collisions des ions et des électrons, accélérés par le champ électrique appliqué, avec les atomes de l'isolant. Le deuxième type de mécanisme est le claquage par avalanche, il se produit lorsque sous l'action d'un champ électrique, les électrons entrent en collision avec les atomes et les ionisent, puis les électrons libérés entrent, à leur tour, en collision avec d'autres atomes et les ionisent. La multiplication des électrons libérés se poursuit jusqu'à ce qu'ils arrivent à l'anode. Un autre type de mécanisme peut également avoir lieu, il s'agit du claquage dit thermique. Ce dernier se développe sous l'effet d'une haute tension appliquée à un diélectrique, les pertes diélectriques sous forme de chaleur augmentent la température du diélectrique jusqu'à l'endommagent de l'isolant suivie d'un claquage.

En général, dans les diélectriques solides le claquage est accompli par la formation de plusieurs canaux de décharge, appelés quelquefois arborescence, comme le montre la Figure 1.21 (Tilmatine, 2006).

Figure 1.21 Arborescence observée dans un isolant solide
Tirée de Tilmatine (2006, p. 12)

Green et al (Green et al., 2011) ont montré que les mélanges de polyéthylène haute densité (HDPE) et de polyéthylène basse densité (LDPE) (cristallisés dans des conditions isothermes), peuvent présenter des rigidités diélectriques élevées (avec un facteur de 15 %) en comparaison avec le polyéthylène réticulé (XLPE), utilisé généralement dans l'isolation du câble HT. La Figure 1.22 (Green et al., 2011) illustre une comparaison entre le mélange LDPE/HDPE avec LDPE et XLDPE. Il est évident que le mélange LDPE/HDPE, préparé par un refroidissement contrôlé ou par trempe montre des performances meilleures par rapport à LDPE ou XLPE.

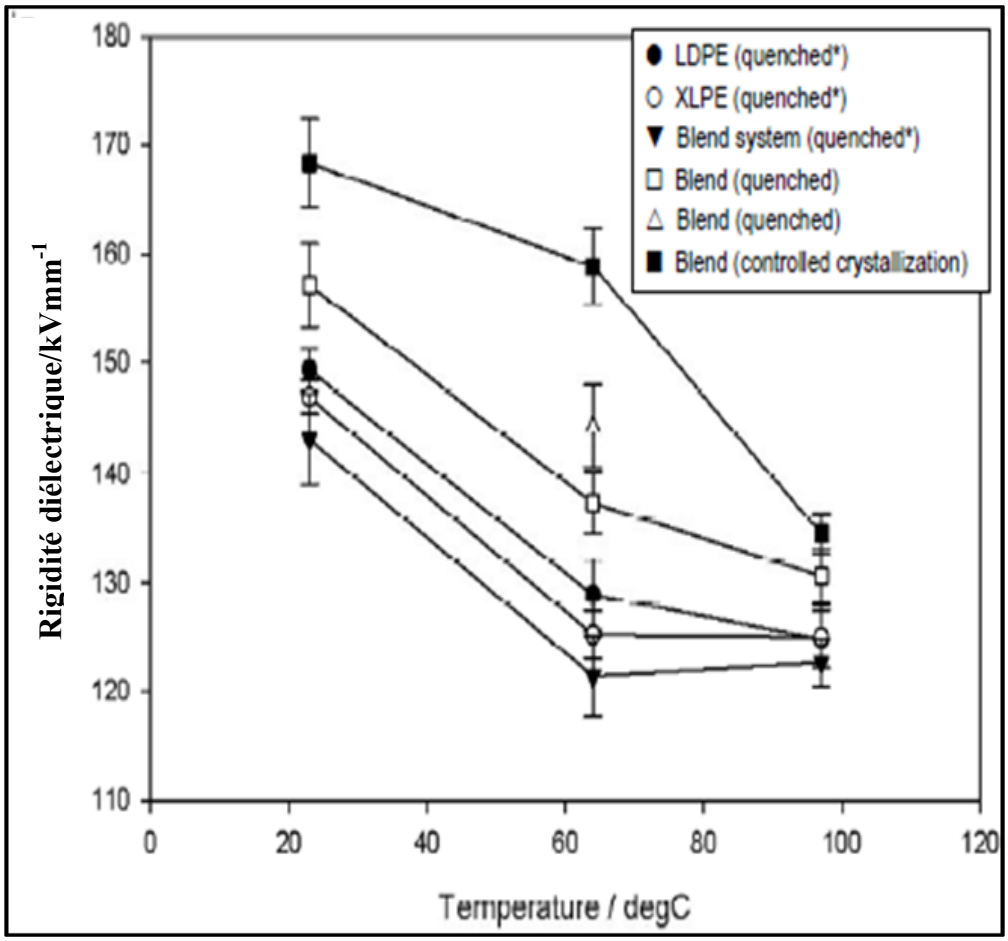

Figure 1.22 Variation de la rigidité diélectrique des systèmes LDPE/HDPE, LDPE et XLPE
Tirée de Green (2011, p. 38) (Green et al., 2011)

Rapport-gratuit.com
LE NUMERO 1 MONDIAL DU MÉMOIRES

Par ailleurs, Green et al (Green et al., 2008) ont préparé des matériaux nanocomposites à partir d'une matrice de polyéthylène et d'un mélange maître (MB) commercial de polyéthylène/nanoargile, en utilisant une extrudeuse à vis unique. Les auteurs ont remarqué que la rigidité diélectrique des matériaux nanocomposites a été élevée en comparaison avec celle du polyéthylène seul et que cette dernière augmente avec le taux des nanocharges (Figure1.23).

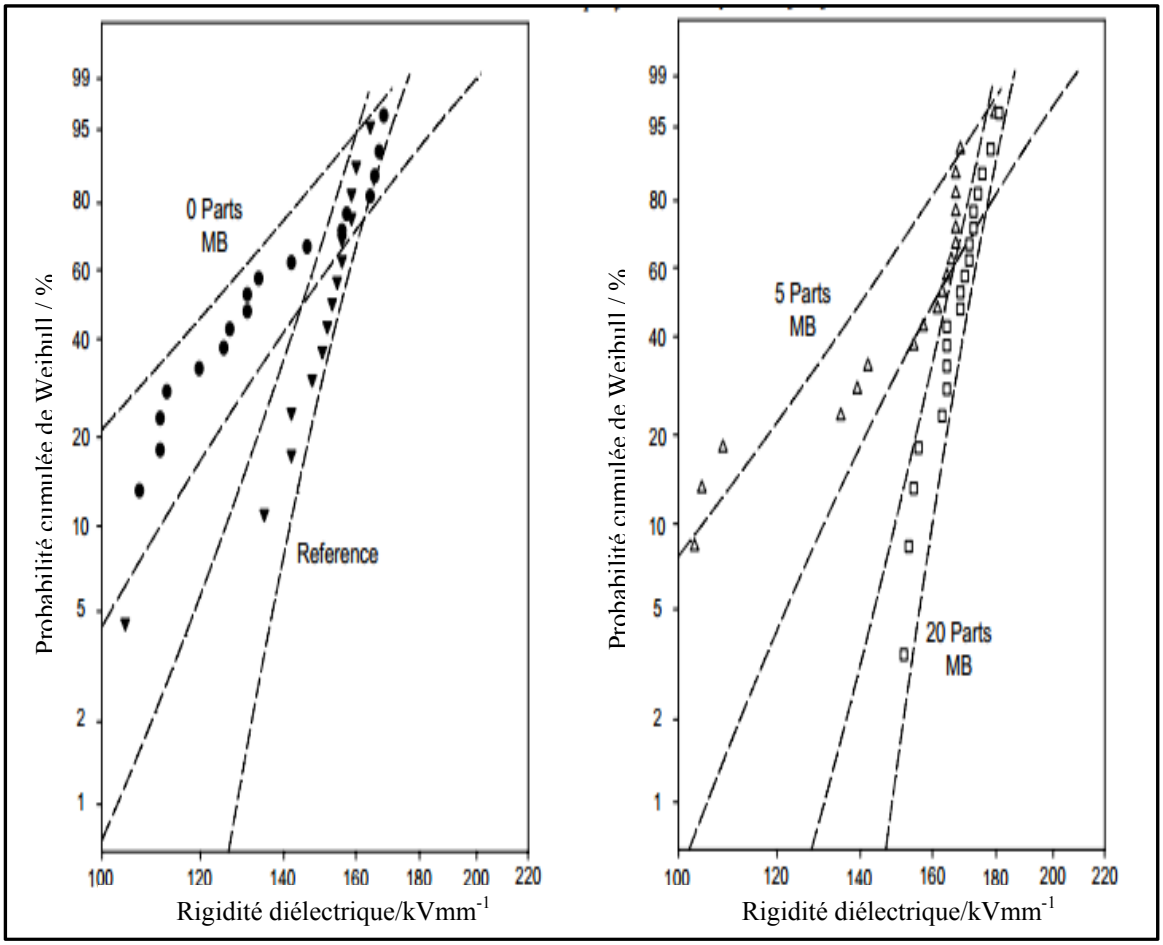

Figure 1.23 Variation de la rigidité diélectrique des systèmes PE/nanoargile nanocomposites
Tirée de Green (2008, p. 140)

CHAPITRE 2

MATÉRIAUX ET MÉTHODOLOGIE

2.1 Matériaux et procédé de fabrication

Dans cette étude, le polyéthylène linéaire basse densité (LLDPE), le polyéthylène basse densité (LDPE) et le polyéthylène haute densité (HDPE), ont été utilisés comme matrices thermoplastiques. Quant au renfort, il est formé par l'argile montmorillonite organo-modifié (O-MMT), qui est utilisé sous forme d'un mélange maître (LLDPE/O-MMT, nanoMax ® LLDPE, Nanocor). Il contient 50 % massique d'argile O-MMT et 50 % massique de LLDPE. Afin d'optimiser la dispersion et aider l'exfoliation des feuillets argileux dans la matrice de polyéthylène, des agents compatibilisants ont été introduits. Il s'agit des polyéthylènes modifiés M603 et E226. Le Tableau 2.1 récapitule les informations techniques données par le fournisseur concernant les matériaux utilisés dans cette recherche.

Tableau 2.1 Propriétés physiques des matériaux utilisés

Matériau	Indice de fluidité (g/10 min)	Masse volumique (g/cm^3)	Nom commercial	Fournisseur
LLDPE	1.0	0.917	FPS117-D	Nova Chemicals
LDPE	0.75	0.919	LF-Y819	NOVAPOL
HDPE	10.5	0.948	DGDP-6097	DOW
LLDPE-g-MA	24	0.940	M603	DuPont
PE-g-MA	1.75	0.930	E226	DuPont
Mélange maître	-	-	nanoMax®-LLDPE Masterbatch	Nanocor

Pour élaborer des nanocomposites à partir d'une matrice polyéthylène et d'un mélange maître commercial, nous avons opté, dans ce projet, pour la technique du mélange à l'état fondu utilisant une extrudeuse à double vis co-rotatives (Haake Polylab Rheomex OS PTW16, D = 16mm, L/D = 40). Dans un premier temps, tous les composants (LDPE, HDPE, LLDPE, mélange maitre et Compatibilisant), ont été déshydratés à l'étuve pendant 48 heures à une température de 40 °C. Ils ont été mélangés, ensuite, manuellement selon la formulation désirée pendant deux minutes. Enfin, ce mélange a été incorporé dans l'extrudeuse à double vis co-rotatives, dont la vitesse est fixée à 140 tours/minutes. Le profil de la température utilisé dans cette étude se situe à 140 °C- 180 °C, depuis la trémie jusqu'à la filière. Quant au débit d'entrée de l'extrudeuse, il est de l'ordre de 1kg/h, et le nombre du passe choisi est égal à 1. Le cordant sorti de l'extrudeuse est découpé en granules, qui sont par la suite moulées en plaque à l'aide d'une presse chauffante, sous une pression de 5Mpsi et une température de 178 °C. Un résumé du procédé utilisé pour fabriquer les nanocomposites est schématisé dans la Figure 2.1.

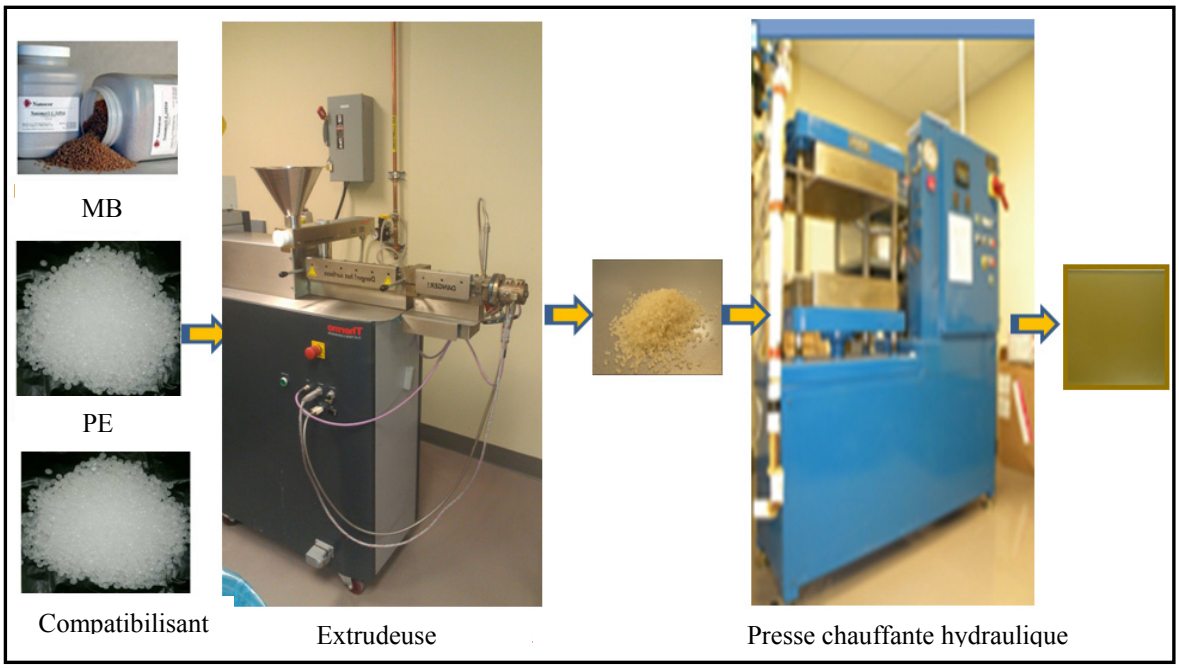

Figure 2.1 Schéma représentant le procédé d'élaboration des nanocomposites par la technique du mélange à l'état fondu

2.2 Analyse morphologique

Pour décrire la microstructure des matériaux nanocomposites et évaluer la dispersion d'argile, deux principales techniques sont utilisées. Il s'agit de la diffraction des rayons X (DRX) et la microscopie électronique à balayage (MEB) ou à transmission (MET) (Alexandre et Dubois, 2000; Sinha Ray et Okamoto, 2003).

2.2.1 Diffraction des rayons X (XRD)

La diffraction des rayons X (DRX) est une technique rapide permettant de distinguer les structures intercalée et exfoliée des matériaux nanocomposites. Elle permet, en fait, de suivre l'évolution de la distance interlamellaire. Pour les nanocomposites argileux, en DRX, le déplacement du pic représentant le plan basal (001) vers les plus petits angles explique l'augmentation de la distance interlamellaire d_{001}, qui traduit la présence d'une structure intercalée. Par ailleurs, la structure exfoliée se caractérise par la disparition du pic du plan cristalophraphique (001). Toutefois, cette absence de pic de diffraction n'affirme pas toujours l'obtention d'une structure exfoliée. Une des raisons pouvant expliquer cette disparition de pic, est qu'aux très petits angles ou pour un taux de charge très faible, le pic de diffraction est indétectable. L'observation en microscopie électronique à balayage ou à transmission est, alors, nécessaire pour confirmer qu'une telle absence de pic de diffraction est attribuée à la structure exfoliée.

L'appareil de DRX utilisé est un PANanalytical X'Pert Pro. La tension accélératrice et l'intensité de l'appareil ont été fixées à 40 kv et 45 mA respectivement. Un rayonnement K_{α}, de longueur d'onde $\lambda = 1.5418$ Å, a été produit par l'anticathode de cuivre. Les mesures sont réalisées en mode transmission.

2.2.2 Microscopie électronique à balayage (MEB)

Le microscope électronique à balayage est utilisé pour observer l'état de dispersion des nanoargiles au sein de la matrice polymère, et pour obtenir des informations sur la

morphologie des nanocomposites. L'appareil utilisé est un Hitachi S4700, et les échantillons ont été d'abord refroidis à une température de -120 °C et coupés avec des couteaux en verre dans un microtome cryogénique.

2.2.3 Microscopie électronique à transmission (MET)

La microscopie électronique à transmission est une technique qui permet d'observer directement la répartition des plaquettes argileuses de montmorillonite au sein de la matrice. En effet, dans une micrographie en transmission, le contraste sombre est relié aux feuillets argileux tandis que le contraste clair représente la matrice polymère. Les principales difficultés de la microscopie électronique sont la préparation de l'échantillon et la représentativité des résultats, puisque la surface à observer est très petite.

2.2.4 Microscopie optique (MOP)

Les propriétés morphologiques à grande échelle ont été caractérisées en utilisant un microscope optique (CE, NMM-800TRF) attaché à une caméra couleur (LEMEX). Les observations ont été réalisées à un grossissement de 200x en mode de transmission. Tous les échantillons ont été préparés sous forme de film d'une épaisseur de 200 µm.

2.2.5 Microscope à force atomique (AFM)

Le microscope à force atomique (AFM) est employé pour évaluer l'état de surface du polyéthylène et ses nanocomposites à l'échelle atomique. Le principe de fonctionnement d'AFM est basé sur la mesure des forces d'interaction (force de Van der Waals, forces magnétiques, forces électrostatiques…), entre la pointe et les atomes d'un matériau. Les échantillons ont été préparés sous forme d'un film d'une épaisseur de 200 µm. Un équipement de type nanocsope est utilisé pour réaliser les mesures par AFM en utilisant le mode "Tapping".

2.3 Propriétés thermiques

2.3.1 Analyse thermique par DSC

La calorimétrie différentielle à balayage (DSC en anglais) est utilisée pour contrôler et analyser un certain nombre de paramètres. Entre autres, on peut citer la température vitreuse (T_g), la température de cristallisation (T_c,) la température de fusion (T_m), le taux de cristallinité et la sensibilité à l'oxydation. Par ailleurs, cette technique utilise un appareillage qui requiert un étalonnage rigoureux. L'échantillon est pesé et mis dans une capsule d'aluminium (il est recommandé d'utiliser des masses entre 5 mg à 15 mg), ensuite une capsule vide est utilisée comme référence. La Figure 2.2 (Perez, 2008) montre clairement le schéma de principe de cette technique.

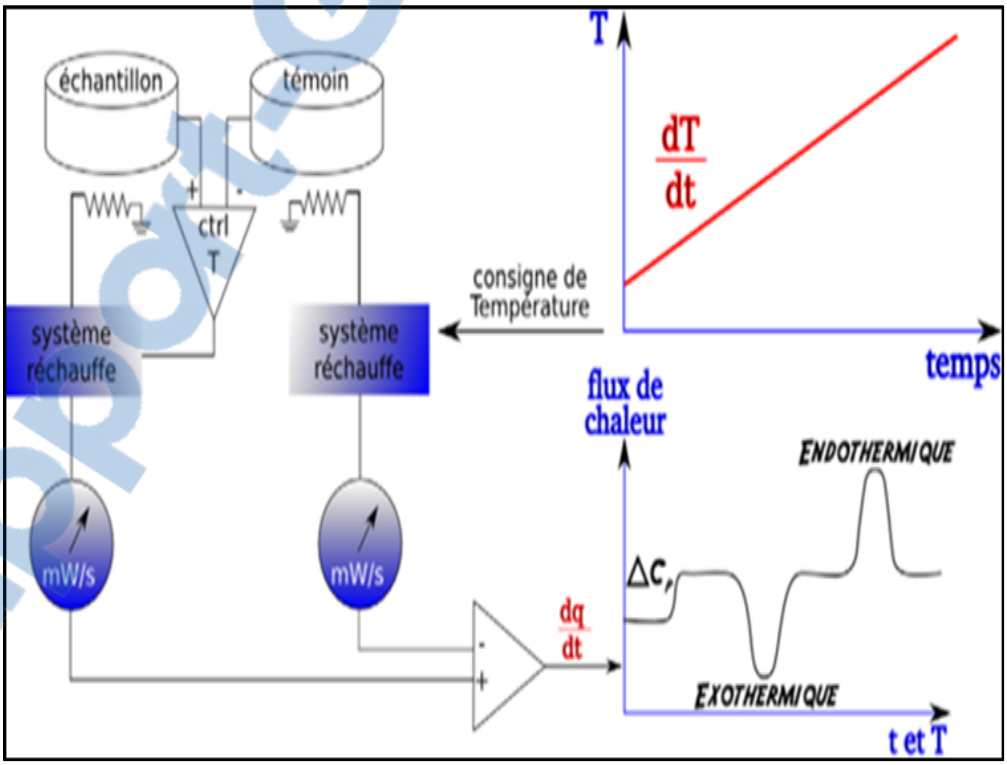

Figure 2.2 Schéma représentant le principe de mesure par DSC
Tirée de Perez (2008, p. 61)

RapportGratuit.com

2.3.2 Analyse thermogravimétrique (ATG)

Pour mesurer la variation de masse d'un échantillon en fonction de la température dans une atmosphère contrôlée, on utilise la technique dite de thermogravimétrie (Thermo–Gravimetric Analysis, TGA). Le principe de fonctionnement de cette technique est illustré sur la Figure 2.3 (SAWI, 2010).

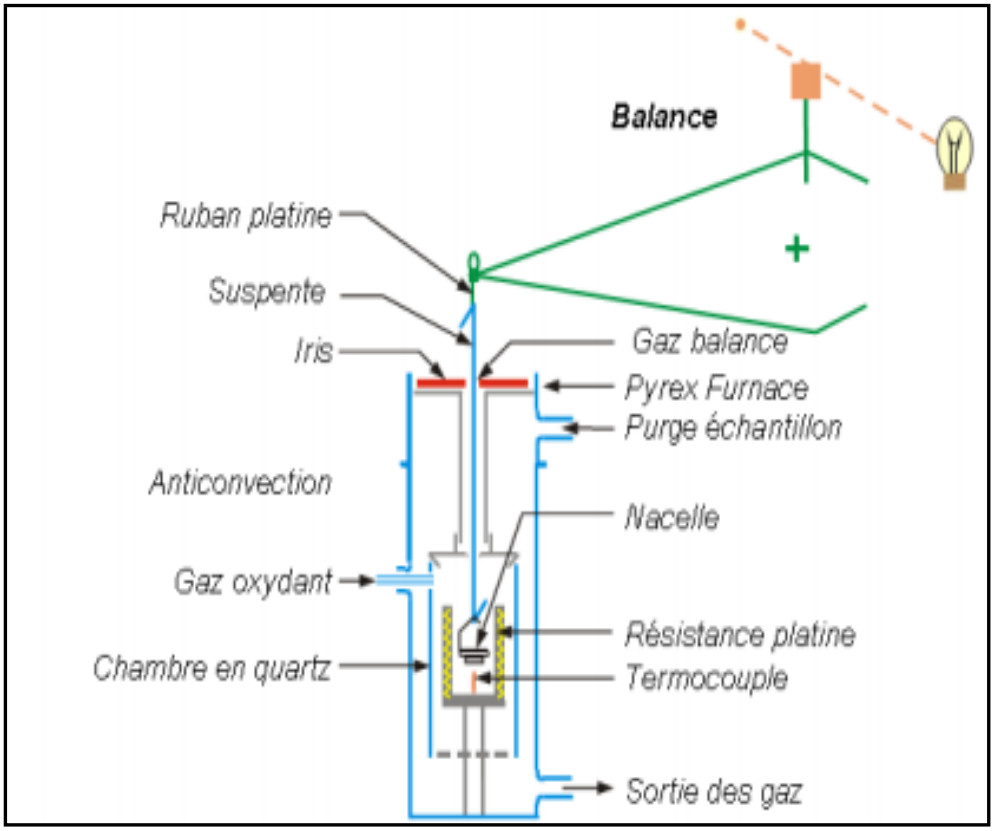

Figure 2.3 Principe de mesure par Analyse Thermo–Gravimétrique (TGA)
Tirée de Sawi (2010, p. 62)

2.4 Analyse mécanique dynamique par DMTA

Le comportement mécanique dynamique a été mis en évidence par des mesures de module dynamique des matériaux soit en fonction de la température, ou en fonction de la fréquence.

Les mesures ont été effectuées en utilisant l'appareil d'analyse thermomécanique dynamique DMTA (Figure 2.4).

Figure 2.4 Analyse Thermomécanique Dynamique DMTA

Le module de la contrainte dynamique sinusoïdale est représenté par le module complexe

$$E^* = E' + iE'' \tag{2.1}$$

où E' représente le module élastique qui mesure l'élasticité ou la possibilité de stocker l'énergie, et E'' est le module de perte (ou visqueux) qui caractérise la viscosité du matériau ou la possibilité de dissiper de l'énergie. La capacité d'amortissement est mesurée par le facteur d'amortissement ou de perte

$$\tan\delta = \frac{E''}{E'} \tag{2.2}$$

Les relaxations présentées dans le matériau sont identifiées par l'évolution soit en fonction de la température ou de la fréquence de ces paramètres (E', E'' *et* $\tan\delta$).

Rapport-gratuit.com
LE NUMERO 1 MONDIAL DU MÉMOIRES

2.5 Mesures diélectriques

2.5.1 Spectroscopie diélectrique

Le principe de mesure de la spectroscopie diélectrique se base sur l'application d'une tension sinusoïdale superposée à la tension nominale. Cette technique consiste à mesurer la valeur efficace du courant induit et le déphasage entre la tension et ce courant (Figure 2.5).

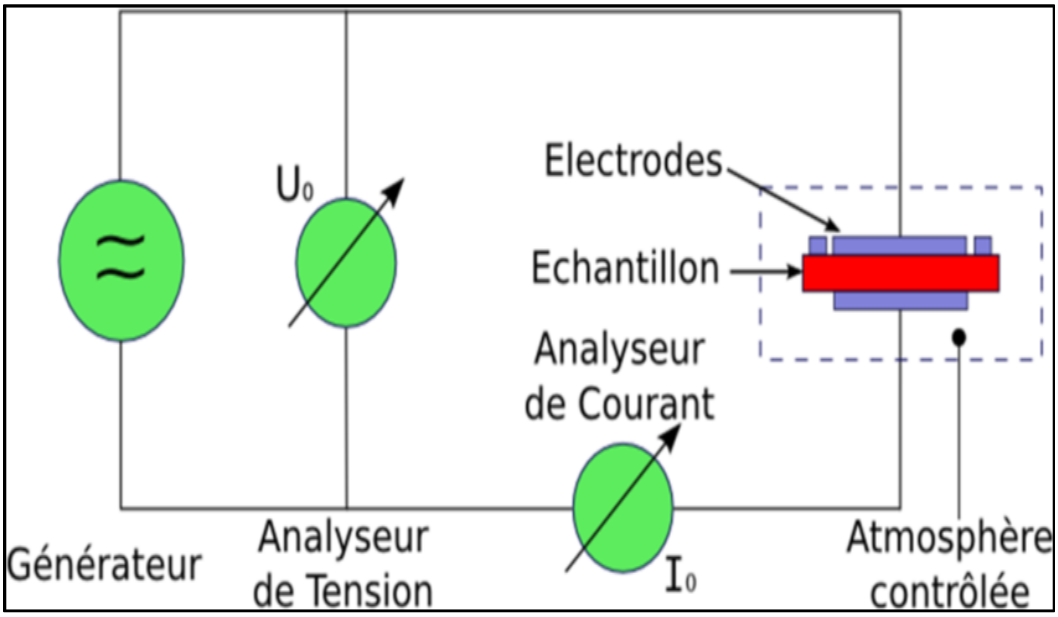

Figure 2.5 Principe de mesure en spectroscopie diélectrique
Tirée de Perez (2008, p. 66)

Les mesures de spectroscopie dans le domaine fréquentiel ont été réalisées en utilisant un Novocontrol alpha-N sur un intervalle de fréquence de 10^{-2} Hz à 10^{6} Hz. L'appareil est équipé d'un système de control de température. Une tension alternative maximale de 3V est appliquée entre les bornes de l'échantillon.

2.5.2 Mesure de rigidité diélectrique

Pour mesurer la rigidité diélectrique, un testeur d'huile du type Baur (Figure 2.6) a été utilisé. Les mesures ont été effectuées selon la norme ASTM D 149. L'échantillon a été immergé dans un bain d'huile minérale (Voltesso N35), et placé entre deux électrodes sphériques de 12.5 mm de diamètre. La tension appliquée à 60 Hz a été augmentée linéairement par un pas de 2 kV/s (de 0 V jusqu'à la rupture du diélectrique testé).

Figure 2.6 Testeur d'huile utilisé pour une mesure de rigidité diélectrique

Les données de la rigidité diélectrique ont été analysées en utilisant la distribution statistique de Weibull. Cette loi, à deux paramètres, peut être exprimée par la relation suivante:

$$P(E) = 1 - \exp[-(\frac{E}{\propto})^{\beta}] \tag{2.3}$$

où P est la probabilité cumulée de Weibull, α et β sont les paramètres d'échelle et de forme de la distribution respectivement, et E représente la rigidité diélectrique. Selon la norme IEEE 930-2004, la probabilité cumulée associée à chaque échantillon est donnée par:

$$P(i,n) = \frac{i-0.44}{n+0.25} \tag{2.4}$$

où i représente l'ième valeur du champ de claquage dans les données expérimentales classées par ordre croissant, et n désigne le nombre total d'échantillons.

CHAPITRE 3

ARTICLE I: LDPE/HDPE/Clay Nanocomposites: Effects of Compatibilizer on the Structure and Dielectric Response

B. Zazoum, E. David and A.D. Ngô

Département de génie mécanique (Mechanical Engineering Department), École de technologie supérieure (ETS), 1100 Notre-Dame Ouest, Montréal QC H3C 1K3, Canada

Article publié dans la revue « Journal of Nanotechnology» en Septembre 2013.

Volume 2013, Article ID 138457, 10 pages
http://dx.doi.org/10.1155/2013/138457

Abstract

PE/clay nanocomposites were prepared by mixing a commercially available premixed polyethylene/O-MMT masterbatch into a polyethylene blend matrix containing 80 wt % low density polyethylene and 20 wt % high density polyethylene with and without anhydride modified polyethylene (PE-MA) as the compatibilizer using a co-rotating twin-screw extruder.

In this study, the effect of nanoclay and compatibilizer on the structure and dielectric response of PE/clay nanocomposites has been investigated. The microstructure of PE/clay nanocomposites was characterized using wide-angle X-ray diffraction (WAXD) and a scanning electron microscope (SEM). Thermal properties were examined using differential scanning calorimetry (DSC). The dielectric response of neat PE was compared with that of PE/clay nanocomposite with and without the compatibilizer. The XRD and SEM results showed that the PE/O-MMT nanocomposite with the PE-MA compatibilizer was better dispersed. In the nanocomposite materials, two relaxation modes are detected in the dielectric losses. The first relaxation is due to a Maxwell-Wagner-Sillars interfacial polarization, and the

second relaxation can be related to dipolar polarization. A relationship between the degree of dispersion and the relaxation rate f_{max} of Maxwell-Wagner-Sillars was found and discussed.

3.1 Introduction

There has been growing interest in polymer/nanoclay nanocomposites in recent years because of their outstanding properties at low loading levels as compared with conventional composites. It has been observed that adding small quantities of nanoclay to some thermoplastics as a reinforcing filler to form nanocomposite materials has not only led to more improved mechanical and thermal properties, but also to an enhancement of the dielectric strength and partial discharge resistance (AWAJI et al., 2009; Chen et Chen, 2009; Han et al., 2001; Hotta et Paul, 2004; Kawasumi et al., 1997; Kim et al., 2009; Kornmann, Lindberg et Berglund, 2001; Tan et Yang, 1998; Utracki et Kamal, 2002; Zhao et He, 2006). However, the understanding of the role of the interfaces of the nanofillers with the molecular mobility mechanism is still rather unsatisfactory.

Although there are different processing methods for preparing nanocomposites, the most widely used technique is the melt-compounding method using a twin-screw extruder, because this technique features economic benefits and ecological advantages. The main challenge in the fabrication of nanocomposites is dispersion of the individual clay platelets into the polymer matrix, due to the incompatibility of hydrophobic matrix with hydrophilic nanoclay (Osman, Rupp et Suter, 2005). Rendering clay platelets more hydrophobic requires a surface treatment, which is accomplished via ion-exchange reactions with cationic surfactants using quaternary alkyl ammonium cations (Zhang et al., 2005). For more polar polymers, such as nylon, a surface treatment of layered silicate with an alkyl-ammonium surfactant is sufficient to facilitate exfoliation of the nanofiller within the polymer matrix in some process conditions. However, in the case of polyethylene, which is a non-polar material, it is necessary to use compatibilizers as maleic anhydride modified polyethylene PE-g-MA, to facilitate the exfoliation process. There are two parameters that contribute to achieving the exfoliation of layered silicates: (1) maleic anhydride content and (2) molecular weight. In general, maleic anhydride modified polyethylene PE-g-MA possess these two required factors, and is widely used as compatibilizer for preparing polyethylene/clay nanocomposites. The most commonly

used techniques for evaluating the quality of the dispersion of the nanoclay within the polymer matrix are scanning electron microscopy (SEM), transmission electron microscopy (TEM) and X-ray diffraction (XRD). Only few publications in this field report the use of dielectric methods, which are able to characterize the level of dispersion and can be combined with microscopic measurements (Böhning et al., 2005; Davis et al., 2004; Noda et al., 2005; Purohit et al., 2011; Tomer et al., 2011).

Polyethylene is one of the polyolefins that used most extensively as ground-wall insulation for medium- to high-voltage applications, and especially for cable insulation, due to its desirable electrical insulating properties, including low relative permittivity ε', low dielectric loss ε'' and high dielectric breakdown strength.

Only a few works have focused on the structure / dielectric response relationship of polyethylene blend nanocomposites. The main objective of this paper is to examine the effect of nanoclay and compatibilizer on the structure and dielectric response of PE/clay nanocomposites prepared by melt-compounding using a co-rotating twin-screw extruder, and to understand the relationship between these two properties.

3.2 Experiment

3.2.1 Materials

The matrix consisted of low-density polyethylene (LDPE, LF-Y819-A, NOVA Chemicals) with a melt flow index (MFI) of 0.75 g/10 min. and a density of 0.919 g/cm^3, and high-density polyethylene (HDPE, DGDP-6097 NT 7, DOW) with a melt flow index (MFI) of 10.5 g/10 min. and a density of 0.948 g/cm^3. The compatibilizer was anhydride modified polyethylene (PE-MA, E226, Dupont) with a melt flow index (MFI) of 1.75 g/10 min. and a density of 0.930 g/cm^3. A commercially available masterbatch of LLDPE/O-MMT (NanoMax) containing 50 wt % organo-modified Montmorillonite (O-MMT) was supplied by Nanocor.

3.2.2 Preparation of nanocomposites

The blend of LDPE/HDPE was fixed at a weight ratio of 80/20. The LDPE, HDPE, PE-MA and the commercial masterbatch of LLDPE/O-MMT were dried at 40 °C in a vacuum oven for a minimum of 48 hrs prior to extrusion. Nanocomposites were prepared by an extrusion process using a co-rotating twin-screw extruder (Haake Polylab Rheomex OS PTW16, D = 16 mm, L/D = 40) coupled with a Haake Metering Feeder to control the feed rate. The temperature profile used in this study was 170 °C - 180 °C from hopper to die, the feed rate was fixed at 1kg/h and the screw speed was set at 140 rpm. All materials were manually pre-mixed before introduction into the twin-screw extruder. The pellets that were obtained after extrusion were press-molded using an electrically heated hydraulic press to form thin plates (1.2-mm thick). The molding temperature and pressure were 178 °C and 5 MPa respectively. A summary of the compositions of the PE/clay nanocomposites used in this paper is collected in Table 3.1.

Tableau 3.1 Sample formulation and designation

Sample designation	**LLDPE (wt %)**	**LDPE/HDPE (wt %)**	**PE-MA (wt %)**	**O-MMT (wt %)**
MB	50	-	-	50
PE	-	100	0	0
PE/O-MMT	5	90	0	5
PE/O-MMT/PE-MA	5	80	10	5

3.3 Characterization and measurements

3.3.1 Differential scanning calorimetry (DSC)

Thermal parameters (melting temperature, crystallization temperature and crystallinity) of neat PE, PE/O-MMT and PE/O-MMT/PE-MA nanocomposites were determined using a Perkin-Elmer DSC Pyris 1 instrument. The calibration of the DSC was performed using indium. All samples had the same weight (approximately 5.0 mg), and the PE and its nanocomposites were heated from 30 °C to 180 °C during each run at a heating rate of 10 °C/min. in nitrogen atmosphere. The endothermic and exothermic diagrams were recorded as a function of temperature.

3.3.2 X-ray diffraction (XRD)

X-ray diffraction (XRD) was employed in order to assess the degree of dispersion and exfoliation or intercalation state of the nanoclay in the polymer matrix. XRD patterns were identified using a diffractometer (PANanalytical X'Pert Pro) with Kα radiation at a wavelength λ of 1.5418 Å, operated at an accelerating voltage of 40 kV and an electrical current of 45 mA. The scanning was conducted from 2° to 9°, with a scan rate of 0.6°/min. The intercalate spacing d_{001} was calculated using Bragg's law:

$$2\,d\,\sin\theta = \lambda \tag{3.1}$$

where d, θ and λ represent the interlayer distance of the clay, the measured diffraction angle and the wavelength, respectively.

3.3.3 Microscopical Observations

The morphology of the samples was examined using a Hitachi scanning electron microscope (SEM). The samples were first cut in a microtome (Ultraculeika) equipped with a glass knife,

Rapport-Gratuit.com

and then coated with a 2-nm thick layer of platinum in order to avoid electrostatic charging during microscopic observations. The operating voltage was fixed at the lowest possible voltage (5 kV) in order to prevent polymer damage and maintain high-resolution images.

3.3.4 Dielectric Relaxation Spectroscopy

Dielectric relaxation spectroscopy experiments were carried out using a Novocontrol alpha-N in the 10^{-2} to 10^{5} Hz frequency domain at temperatures of 30, 40, 50, 60 and 70 °C. The temperature was controlled using a Novotherm system with a stability of 0.5 °C.

Prior to all dielectric spectroscopy measurements, the samples measuring 40 mm in diameter and 1.20 mm in thickness were dried at 50 °C in a vacuum oven for 24 hrs, and then sandwiched between two gold-plated electrodes measuring 40 mm in diameter to form a parallel-plate geometry capacitor.

The complex dielectric permittivity is given by:

$$\varepsilon^*(\omega) = \varepsilon'(\omega) - i\varepsilon''(\omega) \tag{3.2}$$

where $\varepsilon'(\omega)$represents the real part, $\varepsilon''(\omega)$ represents the imaginary part and $\omega = 2\pi f$ represents the angular frequency.

The experimental dielectric data can be fitted into the Havrialk-Negami equation as shown below:

$$\varepsilon^* = \varepsilon_\infty + \sum_{i=1}^{n} \frac{\Delta\varepsilon_i}{(1 + (i\omega\tau_i)^{\alpha_i})^{\beta_i}} \tag{3.3}$$

where ε_∞ represents the high frequency permittivity, $\Delta\varepsilon_i$ represents the ith dielectric relaxation strength, τ_i represents the relaxation time of the ith relaxation, n represents the number of relaxation processes and α_i and β_i ($0<\alpha\leq1$, $\alpha\beta\leq1$) represent the shape parameters describing symmetric and asymmetric broadening of the relaxation spectra. At low

frequency, the influence of the charge carrier fluctuations must be taken into consideration. The complex permittivity can then be expressed as:

$$\varepsilon^* = \varepsilon_\infty + \sum_{i=1}^{n}[\frac{\Delta\varepsilon_i}{(1+(i\omega\tau_i)^{\alpha_i})^{\beta_i}}] + \frac{\sigma_0}{\varepsilon_0(i\omega)^s} \tag{3.4}$$

By using equations (3.2), (3.3) and (3.4), the real part $\varepsilon'(\omega)$ and the imaginary part $\varepsilon''(\omega)$ of the complex dielectric permittivity $\varepsilon^*(\omega)$ can be written as:

$$\varepsilon'(\omega) = \varepsilon_\infty + \sum_{i=1}^{n}[\frac{\Delta\varepsilon_i\cos(\beta_i\varphi_i)}{(1+2(\omega\tau_i)^{\alpha_i}\sin\left(\frac{\pi(1-\alpha_i)}{2}\right)+(\omega\tau)^{2\alpha_i})^{\beta_i/2}}] + \frac{\sigma_o\omega^{-s}}{\varepsilon_0}\cos(\frac{\pi s}{2}) \tag{3.5}$$

and

$$\varepsilon''(\omega) = \sum_{i=1}^{n}[\frac{\Delta\varepsilon_i\sin(\beta_i\varphi_i)}{(1+2(\omega\tau_i)^{\alpha_i}\sin\left(\frac{\pi(1-\alpha_i)}{2}\right)+(\omega\tau)^{2\alpha_i})^{\beta_i/2}}] + \frac{\sigma_o\omega^{-s}}{\varepsilon_0}\sin(\frac{\pi s}{2})$$

where

$$\varphi_i = \tan^{-1}[\frac{(\omega\tau_i)^{\alpha_i}\cos\left(\frac{\pi(1-\alpha_i)}{2}\right)}{1+(\omega\tau_i)^{\alpha_i}\sin\left(\frac{\pi(1-\alpha_i)}{2}\right)}] \tag{3.6}$$

where σ_o represents dc conductivity and s represents an adjustable parameter. In the case of pure electronic dc conductivity, s = 1.

Rapport-gratuit.com
LE NUMERO 1 MONDIAL DU MÉMOIRES

3.4 Results and discussion

3.4.1 Thermal Properties

Differential scanning calorimetry (DSC) was used to measure the melting temperatures, crystallization temperatures and fusion enthalpy ΔH_F. The degree of crystallinity was calculated as expressed by the following equation:

$$\% \chi = \frac{\Delta H_F}{\Delta H_F^0 (1-\varphi)} \tag{3.7}$$

where ΔH_F represents the heat of fusion (J/g), ΔH_F^0 represents the theoretical heat of fusion of 100 % crystalline PE (293 J/g) and φ represents the weight fraction of O-MMT in the composites.

The melting and crystallization curves of neat polyethylene and its nanocomposites are depicted in Figure 3.1 and Figure 3.2 respectively. The thermal parameters derived from these curves are shown in Table 3.2. Differential scanning calorimetry (DSC) thermograms revealed two different peak temperatures, with the first melting temperature related to LDPE and the second melting temperature related to HDPE. The melting point peak of LLDPE was not detected due to the low concentration of LLDPE in the nanocomposites. The DSC results clearly showed that the melting temperature, crystallization temperature and crystallinity of PE/O-MMT and PE/O-MMT/PE-MA are almost the same as those of neat PE. This behavior suggests that the presence of the organoclay did not create a nucleating effect. The same results were found by Morawiec et al. (Morawiec et al., 2005).

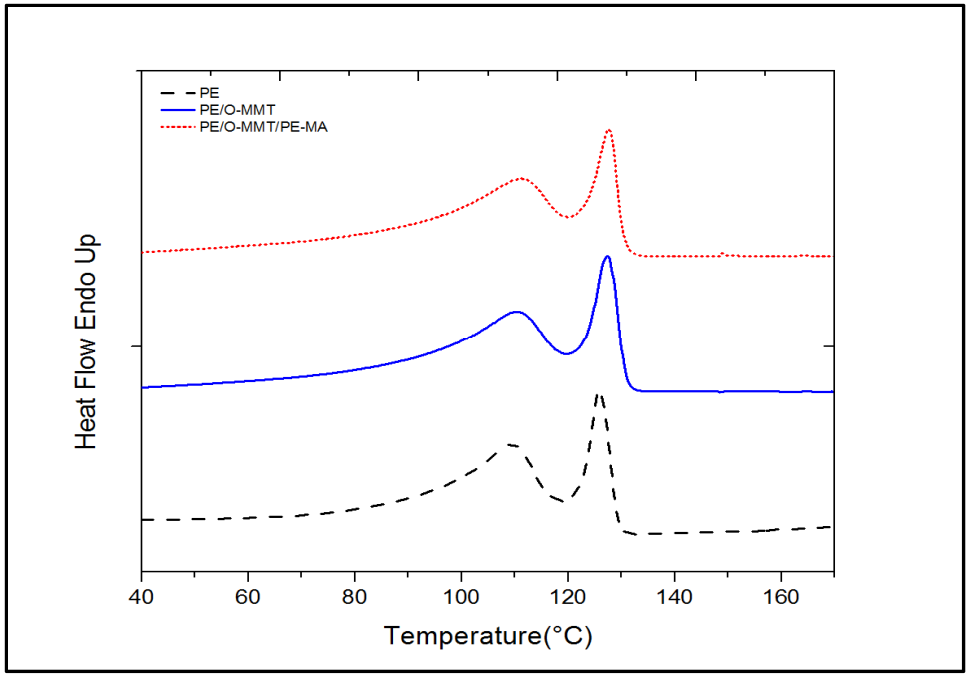

Figure 3.1 DSC heating thermograms of neat PE, PE/O-MMT and PE/O-MMT/PE-MA nanocomposites

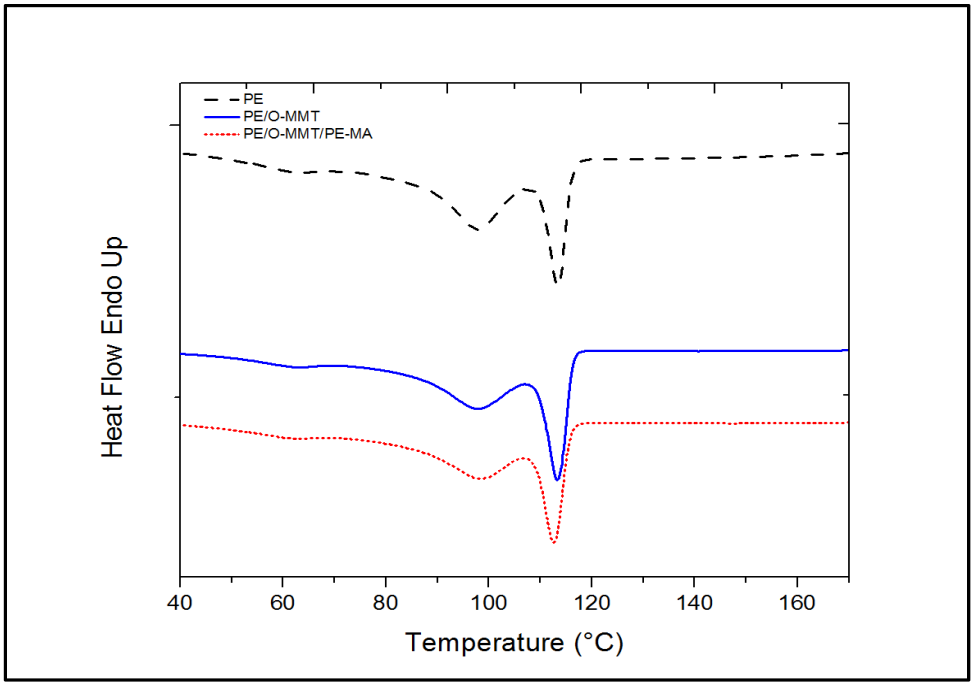

Figure 3.2 DSC cooling thermograms of neat PE, PE/O-MMT and PE/O-MMT/PE-MA nanocomposites

Tableau 3.2 DSC data for PE and its nanocomposites

Samples	LDPE (T_m, °C)	HDPE (T_m, °C)	LDPE (T_c, °C)	HDPE (T_c, °C)	Heat of fusion (J/g)	Crystallinity (%)
PE	109.4	125.8	97.3	113.5	115.8	39.5
PE/O-MMT	110.6	127.4	97.4	113.4	114.4	41.1
PE/O-MMT/PE-MA	110.9	127.7	98.8	112.7	113.7	40.8

3.4.2 Wide-angle X-ray diffraction (WAXD)

Figure 3.3 shows the X-ray diffraction spectra for the O-MMT masterbatch, PE/O-MMT and PE/O-MMT/PE-MA nanocomposites. The diffraction peak for the O-MMT masterbatch is approximately $2\theta = 3.13°$, which corresponds to a d_{001} value of 2.82 nm calculated using the Bragg law (Table 3.3). When the O-MMT masterbatch was diluted with pure PE to create PE/O-MMT nanocomposites, the diffraction peak was found to shift to a smaller angle of 2.93°, indicating the increase in d_{001} spacing of the galleries of the organoclay. This improvement in the dispersion was due to the processing conditions for the fabrication of nanocomposites. For the ternary nanocomposites PE/O-MMT/PE-MA, the diffraction peak was observed at a lower angle of 2.73°, corresponding to an increase in intercalate spacing d_{001} to 3.25 nm. On the other hand, the reduction in the diffraction intensity accompanied by the broadening of the basal peak in the PE/O-MMT/PE-MA nanocomposites suggests that the degree of dispersion of the nanoclay within the polymer matrix was improved, and these compatibilized nanocomposites contain a significant proportion of exfoliated nanoclay in the

final nanocomposites. This is due to the polar interactions between the maleic anhydride groups in the PE-MA and the OH groups of clay which lead to a formation of a covalent bond between clay and compatibilizer (Dumont et al., 2007) and helps polymer chains to penetrate the galleries of the organoclay easily (Gopakumar et al., 2002; Hotta et Paul, 2004). Since PE-MA has a high molecular weight (low melt index) the shear stress was significant, which led to an increase in the delamination of the clay platelets (Hasegawa et al., 1998; Hasegawa et al., 2000; Kato, Usuki et Okada, 1997; Kawasumi et al., 1997; Maiti et al., 2002; Manias et al., 2001; Nam et al., 2001; Wang et al., 2006).

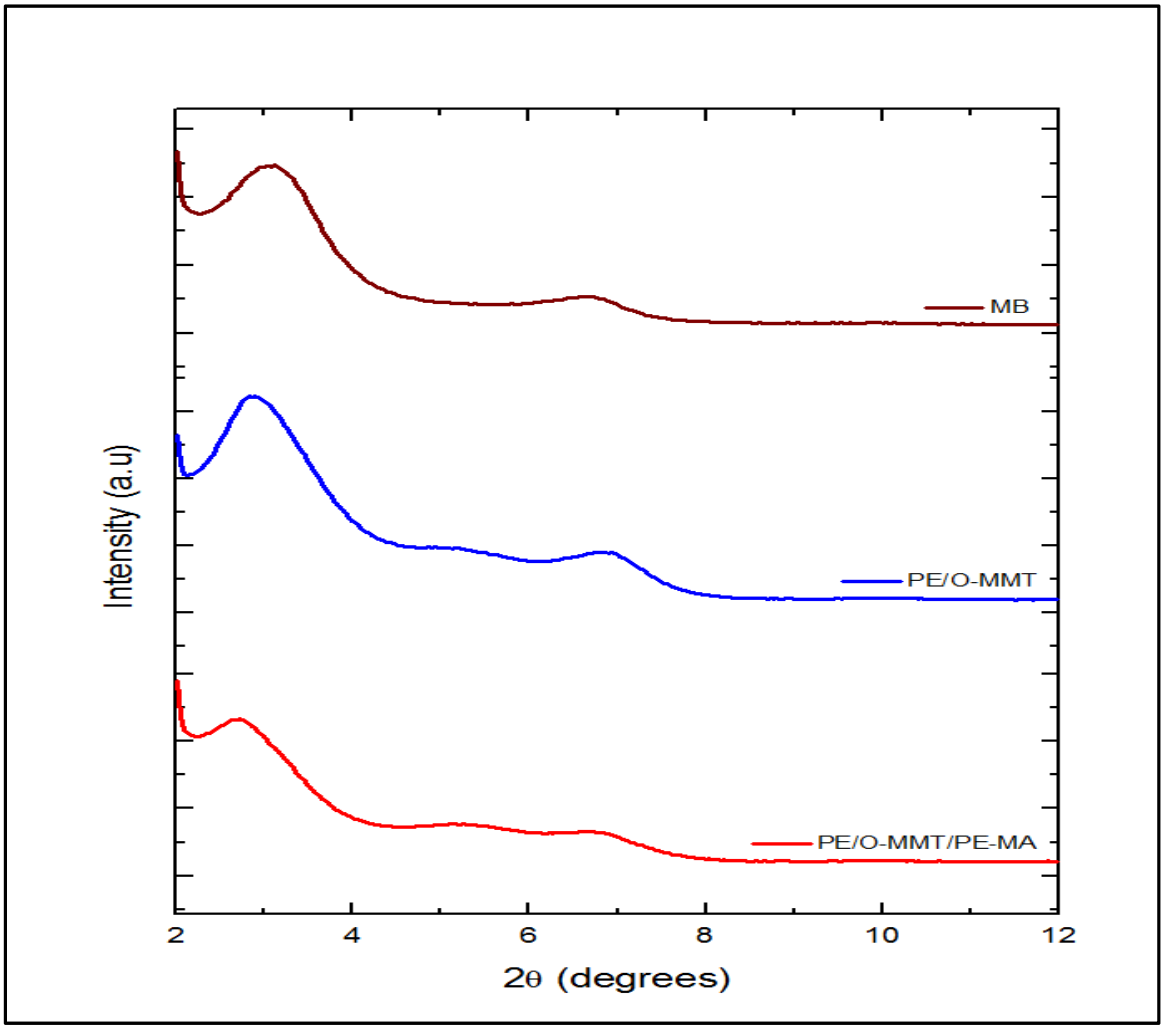

Figure 3.3 X-ray diffraction patterns for MB and PE nanocomposites with and without compatibilizer

Tableau 3.3 2θ and d_{001} data for the different nanocomposites

Sample	**2θ (°)**	**d_{001} (nm)**
MB	3.13	2.82
PE/O-MMT	2.93	3.02
PE/O-MMT/PEMA	2.72	3.25

3.4.3 Morphological characterizations by SEM

In order to confirm the XRD results, the morphology of the nanocomposites was observed using a scanning electronic microscopy (SEM). Figure 3.4 shows the morphology of neat PE (Figure 3.4 (a)), PE/O-MMT (Figure 3.4 (b)) and the ternary nanocomposites PE/O-MMT/PE-MA (Figure 3.4(c)) at a magnification of 5,000. For PE/O-MMT nanocomposites, the existence of the clay aggregates or tactoids can be seen at the micrometer level, and therefore, the morphology is not homogeneous, which reveals a poor intercalated/exfoliated structure. However, when the compatibilizer was added, it was observed that the density and size of the aggregates decreased, which indicates that the dispersion of nanoclays within the polymer matrix is much better. This is consistent with the higher intercalate spacing d_{001} and the reduction in the diffraction intensity accompanied by the broadening of the peak observed in the XRD results (Figure 3.3 and Table 3.3).

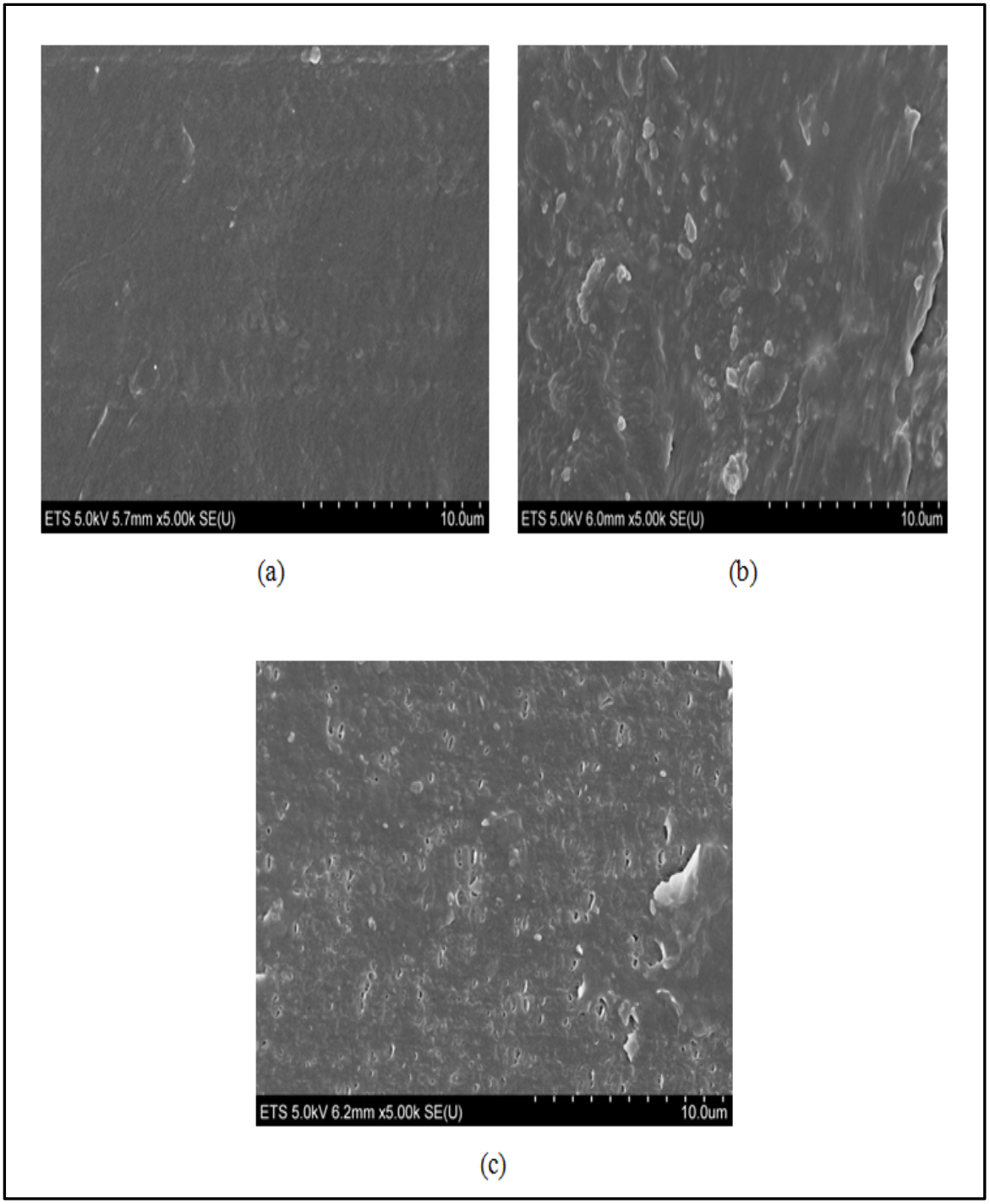

Figure 3.4 Representative SEM micrographs for a) neat PE, b) PE/O-MMT and c) PE/O-MMT/PE-MA

3.4.4 Broadband dielectric spectroscopy

Polyethylene is classified as a non-polar polymer with low dielectric permittivity. In general, this type of material exhibits no notable or significant ionic, interfacial or dipolar polarization, being characterized by low flat dielectric losses. As observed from Figure 3.5 (a), the relative permittivity (ε') of neat PE remains essentially constant in the 10^{-2} to 10^{5} frequency range, showing a small decrease when the temperature is increased. The slight decrease in (ε') at higher temperatures can be related to a combination of water evaporation and a decrease in the density (Tomer et al., 2011). While, the dielectric loss (ε'') of neat PE at low frequency (Figure 3.5 (b)) shows a significant increase, which can be attributed to the contribution of charge carriers leading to various forms of conductivity and electrode polarization (Kremer et Schönhals, 2003). This is the so-called low-frequency dispersion. As expected, no relaxation process is detected in this material.

For PE/O-MMT nanocomposites, Figure 3.6 shows the frequency dependence of relative permittivity (ε') and dielectric loss (ε'') at various temperatures. It can be seen that the relative permittivity (ε') shows two sharp decreases (Figure 3.6 (a)), corresponding to the two peaks in the dielectric losses (ε'') (Figure 3.6 (b)). This indicates that the nanocomposites exhibited two dielectric relaxation processes. It is evident that the (ε'') peaks observed in PE/O-MMT nanocomposites are due to the addition of nanoclay, because no dielectric relaxations were observed for the neat PE. The peaks of the relaxation processes presented in the nanocomposites were shifted to higher frequencies as the temperature was increased. This change shows that the relaxation processes exhibited thermal activation behavior.

In order to clearly show the relaxation processes observed in PE/O-MMT nanocomposites, the dielectric loss (ε'') was plotted as a function of the frequency and temperature in a 3D representation (Figure 3.7). Two relaxation modes were observed in the dielectric losses. The first relaxation was detected at low frequency, and it is attributable to a Maxwell-Wagner-Sillars polarization associated with the blocking of charges at the interfaces between two inhomogeneous phases with different conductivity, such as the polymer matrix and the silicates filler (Laredo et al., 2003; Le Huy et Rault, 1994; McCall et Anderson, 1960). The

second relaxation, which was detected at high frequency, can be attributed to dipolar polarization associated with the polar characteristic of the intercalant that was used for surface treatment of montmorillonite clay.

The experimental data related to the dielectric loss (ε'') for PE/O-MMT nanocomposites were fitted into the Havrialk-Negami function (Figure 3.8.), and the optimum dielectric parameters are shown in Table 3.4.

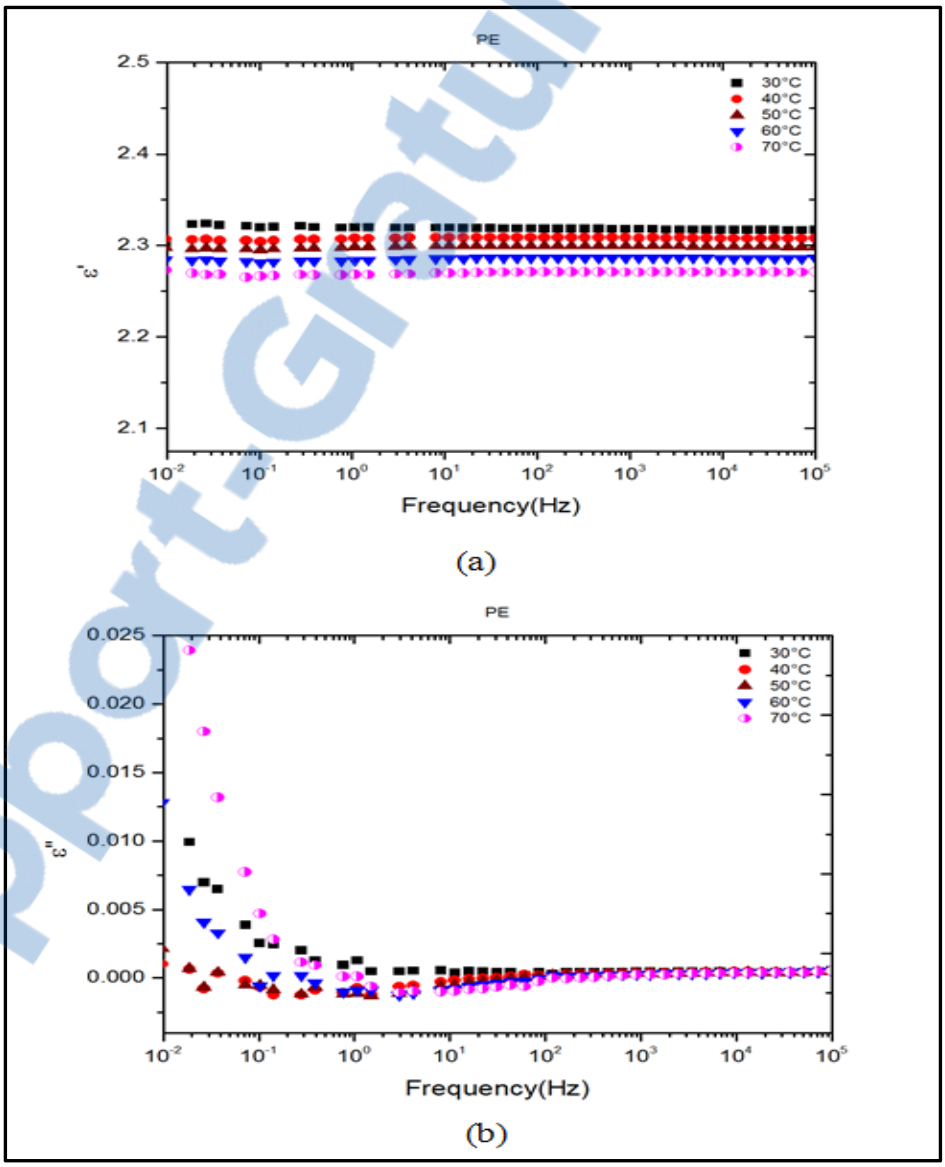

Figure 3.5 Relative permittivity ε' (a) and dielectric loss ε'' (b) versus frequency at various temperatures observed for the neat PE blend

Rapport-Gratuit.com

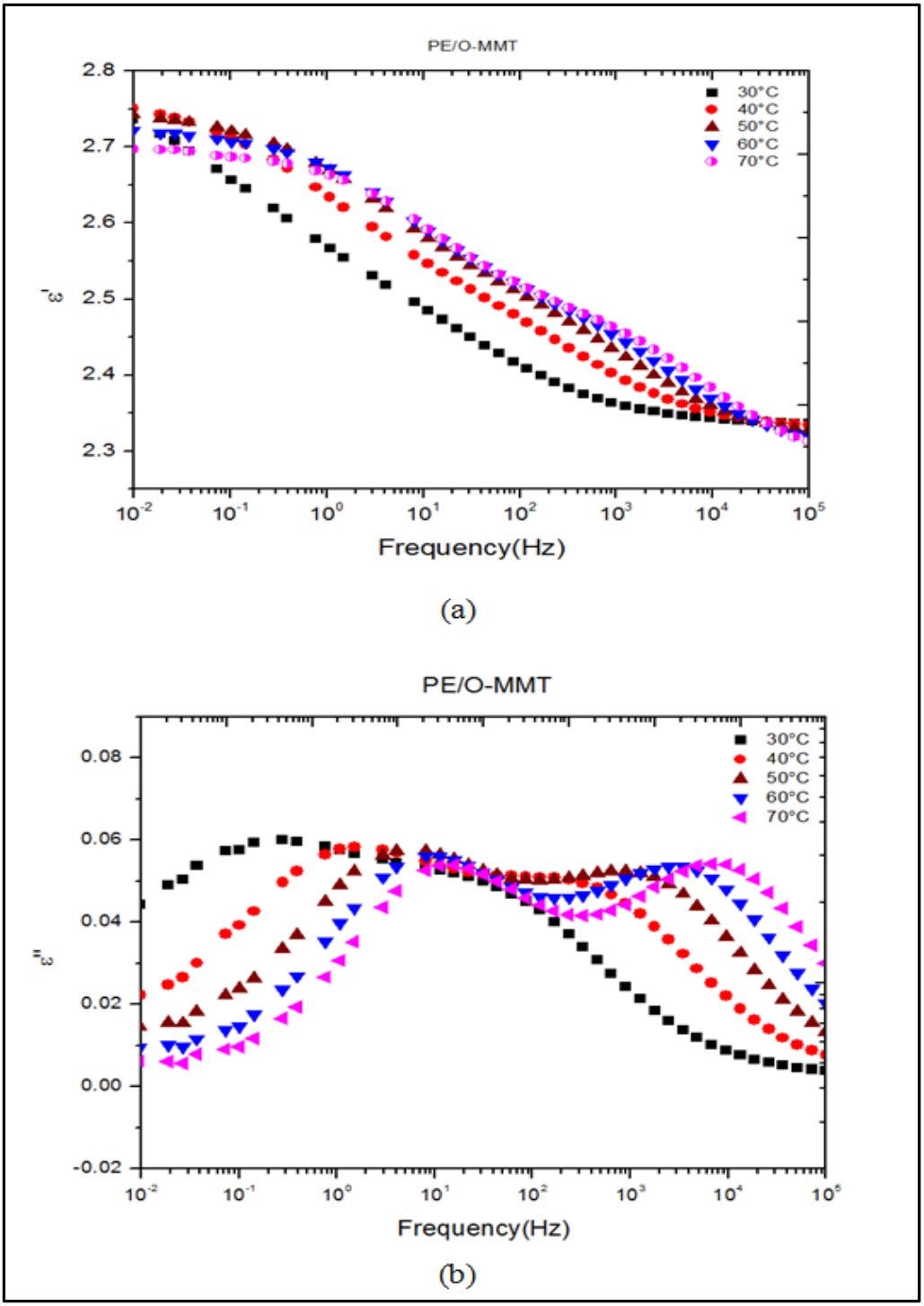

Figure 3.6 Relative permittivity ε' (a) and dielectric loss ε'' (b) for PE/O-MMT nanocomposites versus frequency at different temperatures

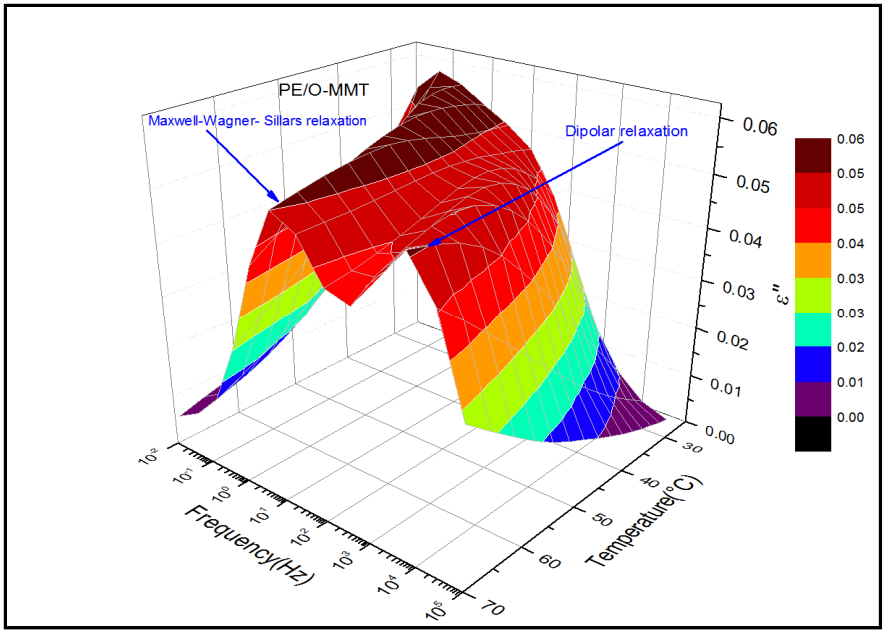

Figure 3.7 Dielectric loss ε″ for PE/O-MMT nanocomposites versus frequency at various temperatures, Plotted in 3D representation

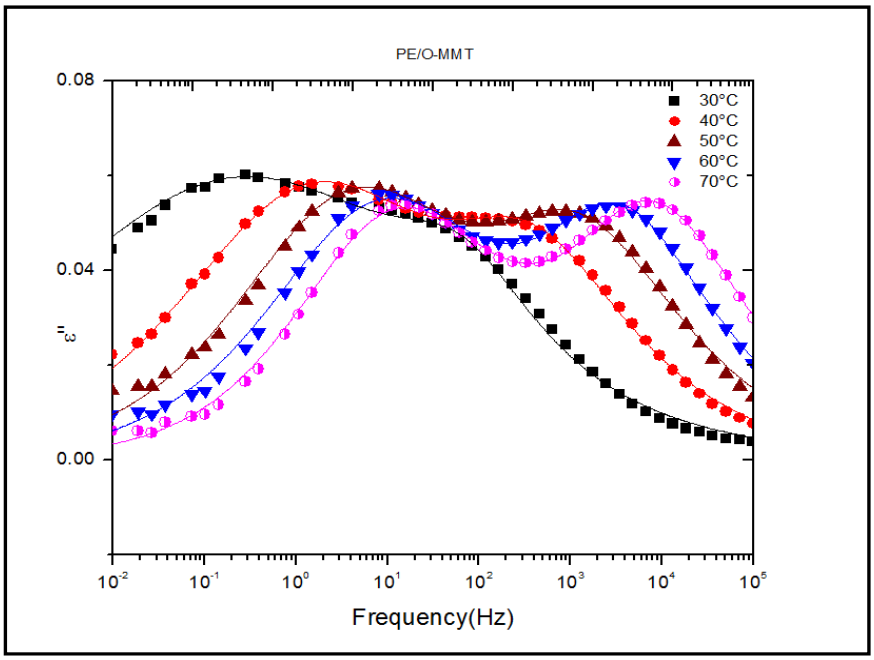

Figure 3.8 Dielectric loss ε″ for PE/O-MMT nanocomposites versus frequency at different temperatures with the optimum fitting curves for the Havrialk-Negami equation

Rapport-gratuit.com
LE NUMERO 1 MONDIAL DU MÉMOIRES

Tableau 3.4 Optimum fit parameters for MWS and dipolar relaxations in Figure 3.8

MWS Polarization				
T(° C)	α_1	β_1	$\Delta\varepsilon_1$	τ_1(s)
30	0.29	1.00	0.50	0.56
40	0.43	1.00	0.32	0.11
50	0.48	1.00	0.27	0.04
60	0.49	0.98	0.26	0.02
70	0.55	0.89	0.23	0.01
Dipolar Polarization				
T(° C)	α_2	β_2	$\Delta\varepsilon_2$	τ_2(s)
30	0.79	0.87	0.05	260E-5
40	0.67	0.63	0.14	60.8E-5
50	0.62	0.70	0.18	17.7E-5
60	0.67	0.68	0.18	6.45E-5
70	0.63	0.81	0.19	2.35E-5

Figure 3.9 shows the frequency dependence of the permittivity (ε') (Figure 3.9 (a)) and the dielectric loss (ε'') (Figure 3.9 (b)) for PE/O-MMT/PE-MA. As observed for PE/O-MMT, the two relaxation processes are also presented for these compatibilized nanocomposites. It can be seen that the relaxation peaks are more thermally activated in PE/O-MMT/PE-MA than in PE/O-MMT.

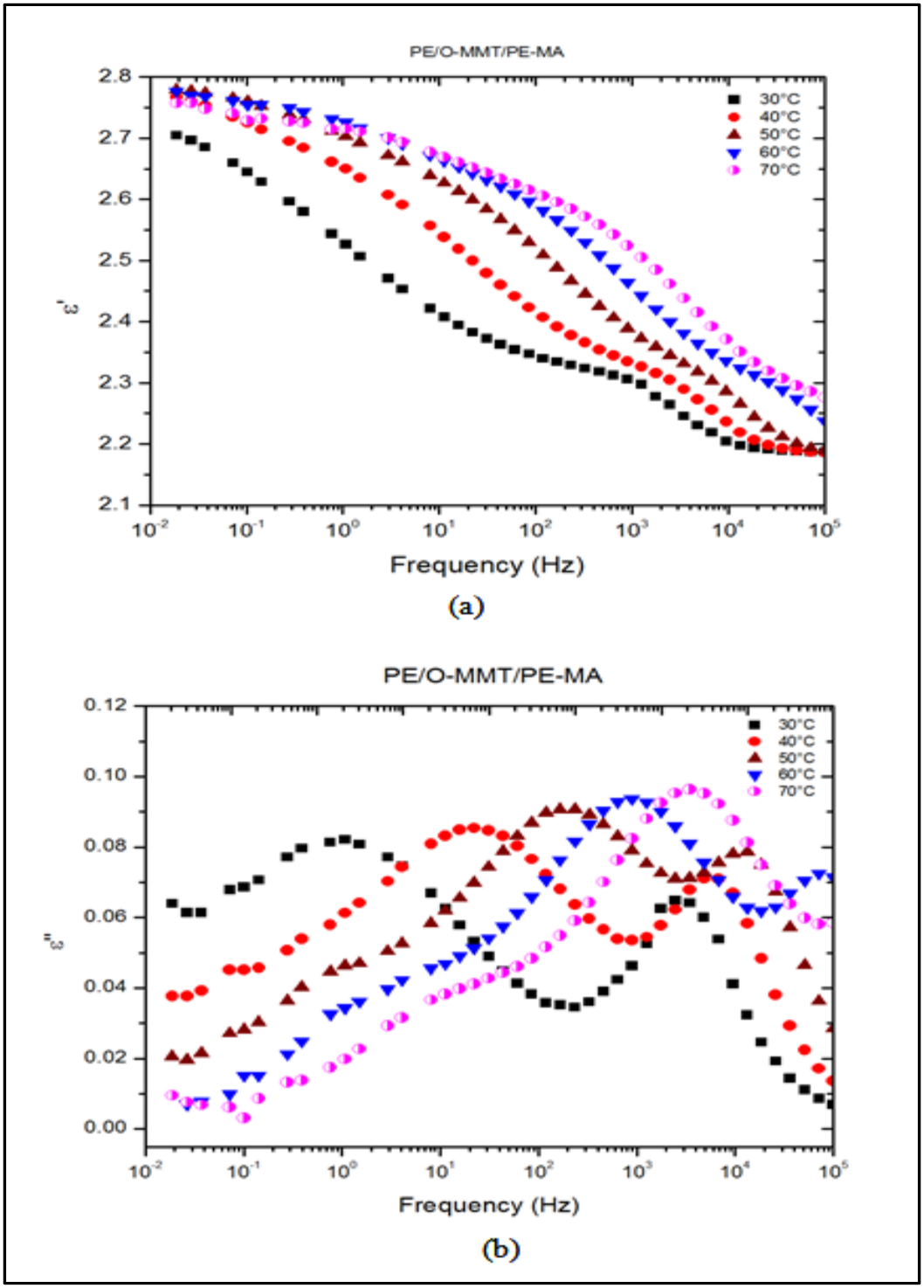

Figure 3.9 Relative permittivity ε' (a) and dielectric loss ε'' (b) for PE/O-MMT/PE-MA nanocomposites versus frequency at different temperatures

In order to study the temperature dependence of both relaxation processes for the PE/O-MMT nanocomposites, the relaxation rate f_{max} of the Maxwell-Wagner-Sillars and dipolar polarization processes were plotted versus inverse temperatures, as shown in Figure 3.10. The data were found to be in agreement with the Arrhenius equation:

$$f_{max}(T) = f_{\infty}\exp(-\frac{E_A}{k_{\beta}T}) \tag{3.8}$$

where f_{∞} represents the pre-exponential factor, E_A represents the activation energy and k_{β} represents the Boltzmann constant. It can be seen that both processes follow Arrhenius' law, with activation energies of 1.2 eV and 1.6 eV for the Maxwell-Wagner-Sillars and dipolar relaxation, respectively.

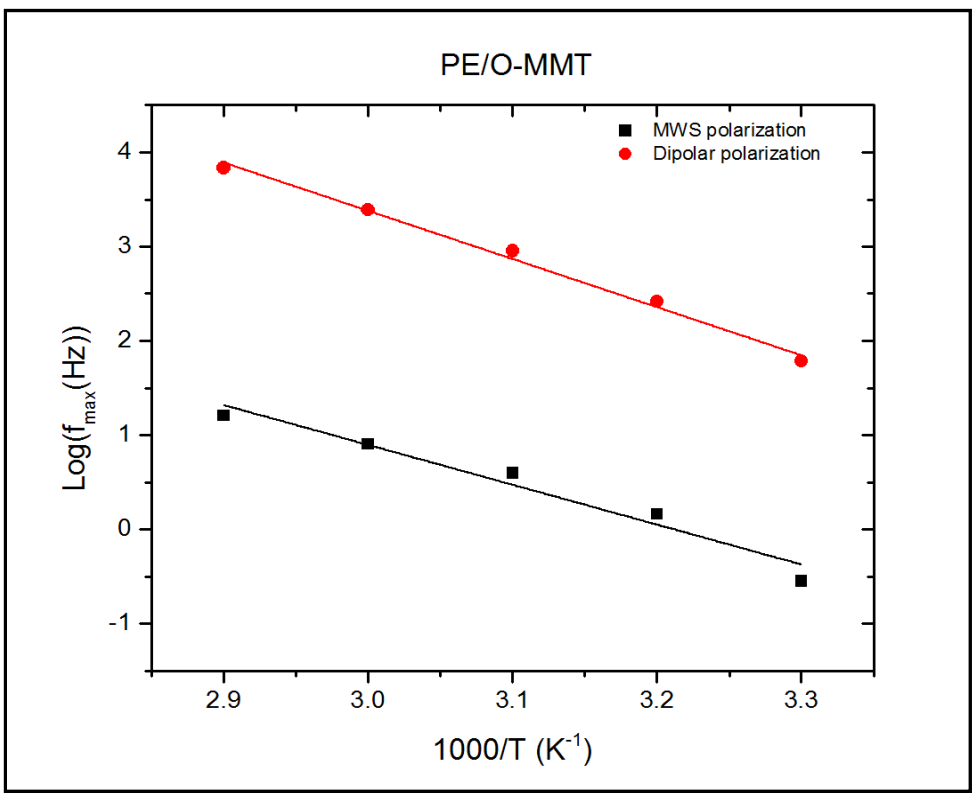

Figure 3.10 Relaxation rate f_{max} as a function of inverse temperature for the two relaxation modes observed in PE/O-MMT nanocomposites. The solid lines represent best fits for the Arrhenius function

It is evident from Figure 3.11 that the values of the relaxation rate f_{max} of Maxwell-Wagner-Sillars are significantly influenced by the structure of the nanocomposites, with the values of f_{max} being higher in the well-dispersed PE/O-MMT/PE-MA nanocomposites than in the PE/O-MMT nanocomposites. In order to better understand the relationship between the structure and the relaxation rate f_{max} of the Maxwell-Wagner-Sillars relaxation process, Böhning et al (Böhning et al., 2005) suggest that f_{max} is inversely proportional to the mean distance d between separated nanoclay layers

$$\frac{f_{max2}}{d_1} \approx \frac{f_{max1}}{d_2} \tag{3.9}$$

Accordingly, the improvement in the degree of dispersion in PE/O-MMT/PE-MA nanocomposites obtained with the addition of the compatibilizer leads to a decrease in the mean distance between the clay layers, and consequently, an increase in the relaxation rate f_{max} for the Maxwell-Wagner- Sillars process.

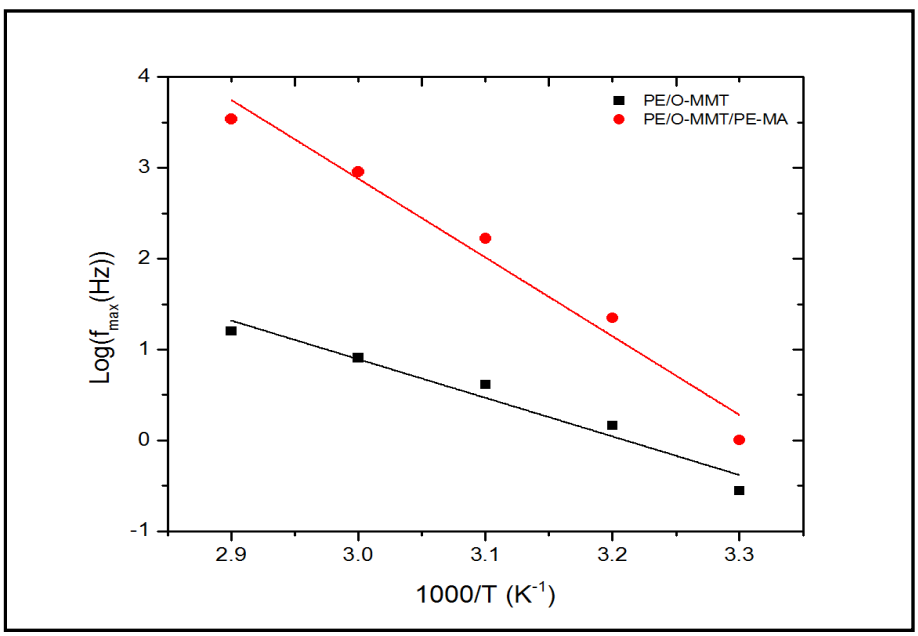

Figure 3.11 Relaxation rate f_{max} as a function of inverse temperature for the MWS relaxation rate observed in PE/O-MMT and PE/O-MMT/PE-MA nanocomposites. The solid lines represent best fits for the Arrhenius function

3.5 Conclusion

A commercially available premixed polyethylene/O-MMT masterbatch was used in this study to prepare PE/O-MMT nanocomposites using a co-rotating twin-screw extruder.
The quality of dispersion was improved by the incorporation of anhydride modified polyethylene (PE-MA) as the compatibilizer. This is due to the fact that PE-MA helps polymer chains to penetrate the galleries of the organoclay easily. No relaxation processes were observed in the neat PE, but two thermally activated relaxation modes were observed in the nanocomposite materials: a low-frequency relaxation that can be attributed to an interfacial process, and a high-frequency relaxation that is related to a dipolar polarization process. It was observed that the relaxation rate of the Maxwell-Wagner-Sillars process increased as the degree of dispersion increased. This correlation shows that broadband dielectric spectroscopy can be used as a macroscopic tool to evaluate the quality of dispersion in nanocomposite materials.

Acknowledgment

The authors are grateful for the financial support revived from the National Sciences and Engineering Research Council of Canada (NSERC).

CHAPITRE 4

ARTICLE II: Correlation Between Structure and Dielectric Breakdown in LDPE/HDPE/Clay Nanocomposites

B. Zazoum, E. David and A.D. Ngô

Département de génie mécanique (Mechanical Engineering Department), École de technologie supérieure (ETS), 1100 Notre-Dame Ouest, Montréal QC H3C 1K3, Canada

Article publié dans la revue «ISRN Nanomaterials» en Mars 2014

Volume 2014, Article ID 612154, 9 pages

http://dx.doi.org/10.1155/2014/612154

Abstract

Cross-linked polyethylene (XLPE) is commonly used in medium/high voltage insulation due to its excellent dielectric properties and acceptable thermo-mechanical properties. To improve both electrical and thermal properties to a point that would possibly avoid the need for crosslinking, nanoclay fillers can be added to polymer matrix to form nanocomposites materials. In this paper, PE/clay nanocomposites were processed by mixing a commercially available premixed polyethylene/O-MMT masterbatch into a polyethylene blend matrix containing 80 wt % low density polyethylene LDPE and 20 wt % high density polyethylene HDPE with and without compatibilizer using a co-rotating twin-screw extruder. Various characterization techniques were employed in this paper, including optical microscopy, AFM, TEM, TGA, DMTA and dielectric breakdown measurements in order to understand the correlation between structure and short-term dielectric breakdown strength.

4.1 Introduction

Polyethylene is the insulation dielectric material of choice because of its high dielectric strength coupled with low dielectric loss, in addition to lending itself to easy processing. Furthermore, polyethylene and polyethylene blends can be extensively recycled, making it a suitable candidate for replacing its cross-linked counter-part, which has limited recyclability.

With conventional composite material, the filler is large or micrometric in size. It has been reported that adding micro-filler has a negative effect on dielectric breakdown strength (Shen et al., 2007) due to the enhancement of the electric field around the aggregated filler particles, leading to decreased breakdown strength. To overcome these limitations, nanocomposite was used as an alternative to replace conventional composite (Artbauer, 1996; Chen et Davies, 2000; Hosier, Vaughan et Swingler, 2002; Ieda, 1980; Job et al., 2003; Lewis, 1994; 2004; Schneuwly et al., 1998; Shen et al., 2007; Sun, Zhang et Wong, 2005; Tuncer, Nettelblad et Gubañski, 2002; Tuncer et al., 2009; Venkatasubramanian et al., 2007; Vorob'ev, 1980; Zakrevskii et al., 2003). Adding a nanoparticle to the polymer matrix resulted in a decrease in the internal electric field due to the reduction in particle size (Ma et al., 2005). It has also been suggested that adding nanoclay can significantly decrease charge accumulation, which leads to increase dielectric breakdown strength (Montanari et al., 2004). In nanocomposites, the interface between the nanoclay and the polymer matrix is very large, compared to that of composite or microcomposite materials. Several authors have reported that interface region plays an essential role in improving the insulating performance of nanodielectric materials (David et al., 2013; Gao et al., 2009; Green et al., 2008; Hoyos et al., 2008b; Junguo et al., 2008; Tanaka, Montanari et Mulhaupt, 2004; Tomer et al., 2011).

In this paper, a blend of 80 wt% of LDPE and 20 wt% of HDPE was used as a matrix. The nanocomposite was prepared by melt compounding the polymer matrix with nanoclay filler using a co-rotating twin-screw extruder.

Only a few studies have focused on the structure-dielectric breakdown correlation in polyethylene/clay nanocomposites (Green et al., 2008). To understand this relationship, microscopic observation, thermal behavior and dynamic mechanical thermal analysis, as well as short-term dielectric breakdown have been studied.

4.2 Experiment

4.2.1 Materials

Low density polyethylene LDPE (LF-Y819-A) with a melt flow index of 0.75 g/10 min and a density of 0.919 g/cm^3 was supplied by NOVA, Canada, while high density polyethylene HDPE (DGDP-6097 NT 7) with a melt flow index of 10.5 g/10 min and a density of 0.948 g/cm^3 was purchased from DOW, USA. The compatibilizer was anhydride modified polyethylene PE-MA (Fusabond E226) with a melt flow index of 1.75 g/10 min and a density of 0.930 g/cm^3, supplied by DuPont Canada. A masterbatch of LLDPE/O-MMT (NanoMax) obtained from Nanocor containing 50 wt % of organo-modified Montmorillonite (O-MMT) and 50 wt % of linear low density polyethylene LLDPE.

4.2.2 Preparation of nanocomposites

The LDPE, HDPE, PE-MA and the LLDPE/O-MMT masterbatch were dried in a vacuum oven at 40 °C for a minimum of 48 hrs. Nanocomposites were prepared by melt compounding using a co-rotating twin screw extruder (Haake Polylab Rheomex OS PTW16, D = 16 mm, L/D = 40). The screw speed was set at 140 rpm and the feed rate was at 1kg/h, while the hopper-to-die temperature profile was 170 °C - 180 °C. The ingredients were manually pre-mixed before being fed into the twin-screw extruder. After extrusion, the pellets were press-molded to form thin plates with a thickness of 590 µm using an electrically heated hydraulic press. The compositions and sample designations for the prepared nanocomposites are listed in Table 4.1.

Rapport-Gratuit.com

Tableau 4.1 Samples formulation and designation

Samples designation	LLDPE (wt %)	LDPE/HDPE (wt %)	PE-MA (wt %)	O-MMT (wt %)
MB	50	-	-	50
PE	-	100	0	0
PE/O-MMT	5	90	0	5
PE/O-MMT/PE-MA	5	80	10	5

4.3 Characterization and measurements

4.3.1 Optical Microscope

The morphological properties were carried out using an optical microscope (CE, NMM-800TRF) with a color camera (LEMEX) attached. Observations were realized at a lens magnification of 200X in transmission mode. All samples were prepared as a thin film with a thickness of 200 µm.

4.3.2 Atomic Force Microscope (AFM)

Microstructures of polyethylene/clay nanocomposites were evaluated using an Atomic Force Microscope (DiNanoScope, Vecco, USA) in tapping mode. The images of the surface topography were then analysed using the Nanoscope (R) III software, Version 5.30r.sr3. The nanoclay appeared brighter than the polyethylene matrix. Samples with a thickness of 590 µm were used, and all measurements were carried out at ambient conditions.

4.3.3 Transmission electron microscope (TEM)

The quality of dispersion of the nanoclays in the polymer matrix was examined by transmission electron microscope (TEM). Ultra-thin sections with a thickness of 50-80 nm were cut from the molded plaque of PE/O-MMT and PE/O-MMT/PE-MA nanocomposites at -120 °C using an ultramicrotome equipped with a diamond knife. The samples were then examined using a high resolution FEM Tecnai G2 F20 with accelerating voltage of 200 kV.

4.3.4 TGA Characterization

Thermogravimetric analysis (TGA) of PE and its nanocomposites was performed on a PYRIS Diamond TG-DTA. The heating process was executed out from 50 to 700 °C at a 10 °C/min heating rate. All measurements were carried out under air and nitrogen atmosphere to evaluate the thermal oxidation and the thermal degradation of the materials, respectively. The nanoclay loading of the nanocomposites materials was also evaluated using this technique.

4.3.5 Dynamic Mechanical Analysis by DMTA

The thermo-mechanical properties of the neat PE blend and its nanocomposites were obtained using a dynamic mechanical thermal analysis (DMTA).
Dynamic stress σ and strain ε are given by:

$$\sigma = \sigma_0 \sin(\omega t + \delta) \qquad (4.1)$$
$$\varepsilon = \varepsilon_0 \sin(\omega t)$$

where ω is the angular frequency and δ is the phase angle.
The complex modulus E^* is given by:

$$E^* = E' + iE'' \qquad (4.2)$$

Rapport-gratuit.com
LE NUMERO 1 MONDIAL DU MÉMOIRES

where the real part E' reflects the elastic energy stored in the material. The imaginary part E'' describes the energy dissipated.
The loss factor *tan δ* is the damping performance, and is represented by:

$$\tan\delta = \frac{E''}{E'} \tag{4.3}$$

Rectangular geometry specimens with a 14 mm length, a 7 mm width and a 1mm thickness were used. All the specimens were cut from the compression-molded plaques. The measurements were carried out in dual cantilever mode at a fixed frequency of 1 Hz and a strain of 0.02 %. The samples were clamped with a 20 cN.m torque in order to achieve reproducible results, and were all cooled down with liquid nitrogen to -30 °C, and then kept for 10 minutes at that temperature.
Storage modulus E' and loss modulus E'' of PE and its nanocomposites were measured from -30 to 100 °C at a 5 °C /min heating rate. This slow heating rate was chosen in order to avoid having the material moving outside the thermodynamic equilibrium.

4.3.6 Dielectric Strength

The dielectric breakdown was measured according to the ASTM D 149 standard, using a BAUR DTA 100 device to hold both the samples and the surrounding medium. A sample with an average thickness of 590 µm was immersed in a mineral oil (Voltesso 35, ESSO Imperial Oil) and placed between two spherical electrodes 12.5 mm in diameter. A 60 Hz voltage was raised at a rate of 2 kV/s from 0 V until the sample failed.
The dielectric strength E depends on the electrical voltage at breakdown V and thickness of specimen *e*:

$$E = \frac{V}{e} \tag{4.4}$$

The dielectric strength data were processed using the two-parameter Weibull statistical distribution (Std-930, 2004). The Weibull statistical distribution in the case of two – parameters can be written as:

$$P(E) = 1 - \exp[-(E/\alpha)^{\beta}] \tag{4.5}$$

where P denotes the cumulative probability of electrical failure, E is the experimental dielectric strength, α is the scale parameter which represents the breakdown strength at the cumulative failure probability of 63.2 %, and finally, β is a shape parameter related to the scatter of data. According to the IEEE 930-2004 standard, the probability of failure *P (i,n)* associated with the E_i data can be approximated by:

$$P(i,n) = \frac{i-0.44}{i+0.25} \tag{4.6}$$

where i is the ith result when the breakdown values are sorted in ascending order and n denotes the number of data points. For this work, n = 20.

The commonly used 90 % confidence intervals were used to compare sets of data by verifying the overlapping of the confidence limits at the 63.2^{th} percentile.

4.4 Results and discussion

4.4.1 Optical Microscopy

Most studies have often used TEM to evaluate the quality of dispersion at high magnifications, while only few works have employed optical microscopy to investigate nanoclay morphologies at low magnifications (Ranade, D'Souza et Gnade, 2002). The optical microscopy images of the polyethylene blend and its nanocomposites are shown in Figure 4.1. In the PE/O-MMT nanocomposites, the presence of significant aggregates with varied dimensions was observed (Figure 4.1 (b)) which was not the case in the neat PE (Figure 4.1

(a)). When the compatibilizer was added, the number and size of aggregates were decreased (Figure 4.1 (c)). This is due to the well-dispersed nanoclay platelet in the polyethylene matrix under the effect of processing conditions and compatibilizer.

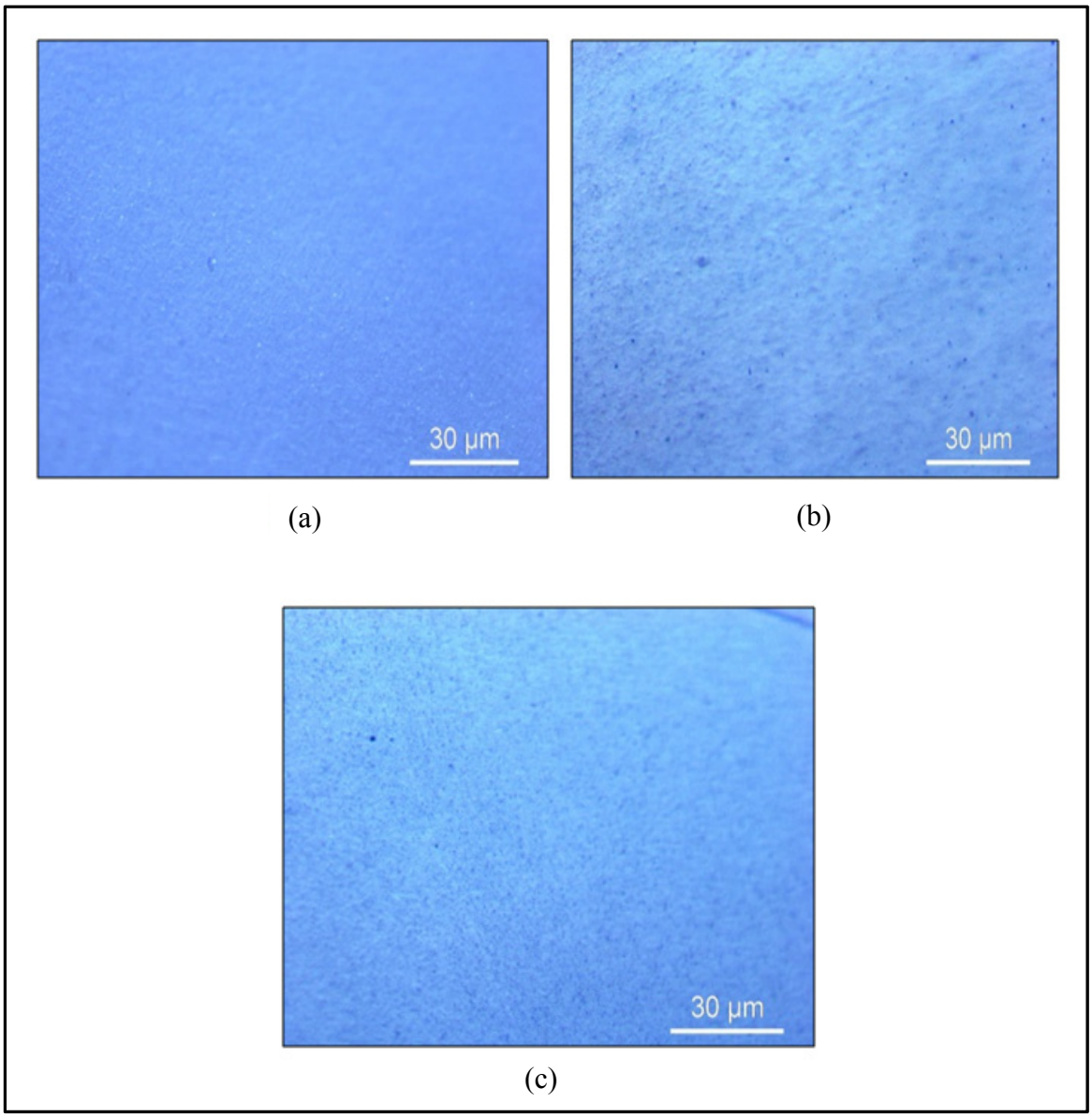

Figure 4.1 Optical microscope images of (a) neat PE, (b) PE/O-MMT and (c) PE/O-MMT/PE-MA

4.4.2 Surface Roughness

In this paper, AFM height images of PE, PE/O-MMT and PE/O-MMT/PE-MA were used in order to study the dispersion of nanoclay in the polymer matrix. The surface properties of neat PE and its two nanocomposites in 3D height image are shown in Figure 4.2. It can be seen that the surface of the neat PE (Figure 4.2 (a)) is relatively smooth in comparison with those of PE/O-MMT (Figure 4.2 (b)) and PE/O-MMT/PE-MA (Figure 4.2 (c)) nanocomposites. From the surface roughness data depicted in Table 4.2, it is evident that PE/O-MMT/PE-MA shows a decrease in the root mean squared R_q and average surface roughness R_a values when compared with PE/O-MMT. The decrease in surface roughness can be attributed to a decrease in aggregate size (Gaume et al., 2012). From the images, it can also be seen that in the compatibilized nanocomposites, the nanoclays are more oriented and structured on the surface. This is due to the good dispersion of nanoclay in PE/O-MMT/PE-MA nanocomposites (Hong et Rhim, 2012).

Tableau 4.2 Surface roughness data of PE and its nanocomposites

Nanocomposites	**R_a (average surface roughness) (nm)**	**R_q (root mean squared) (nm)**
PE	11.0	16.3
PE/O-MMT	13.5	25.4
PE/O-MMT/PE-MA	11.7	18.0

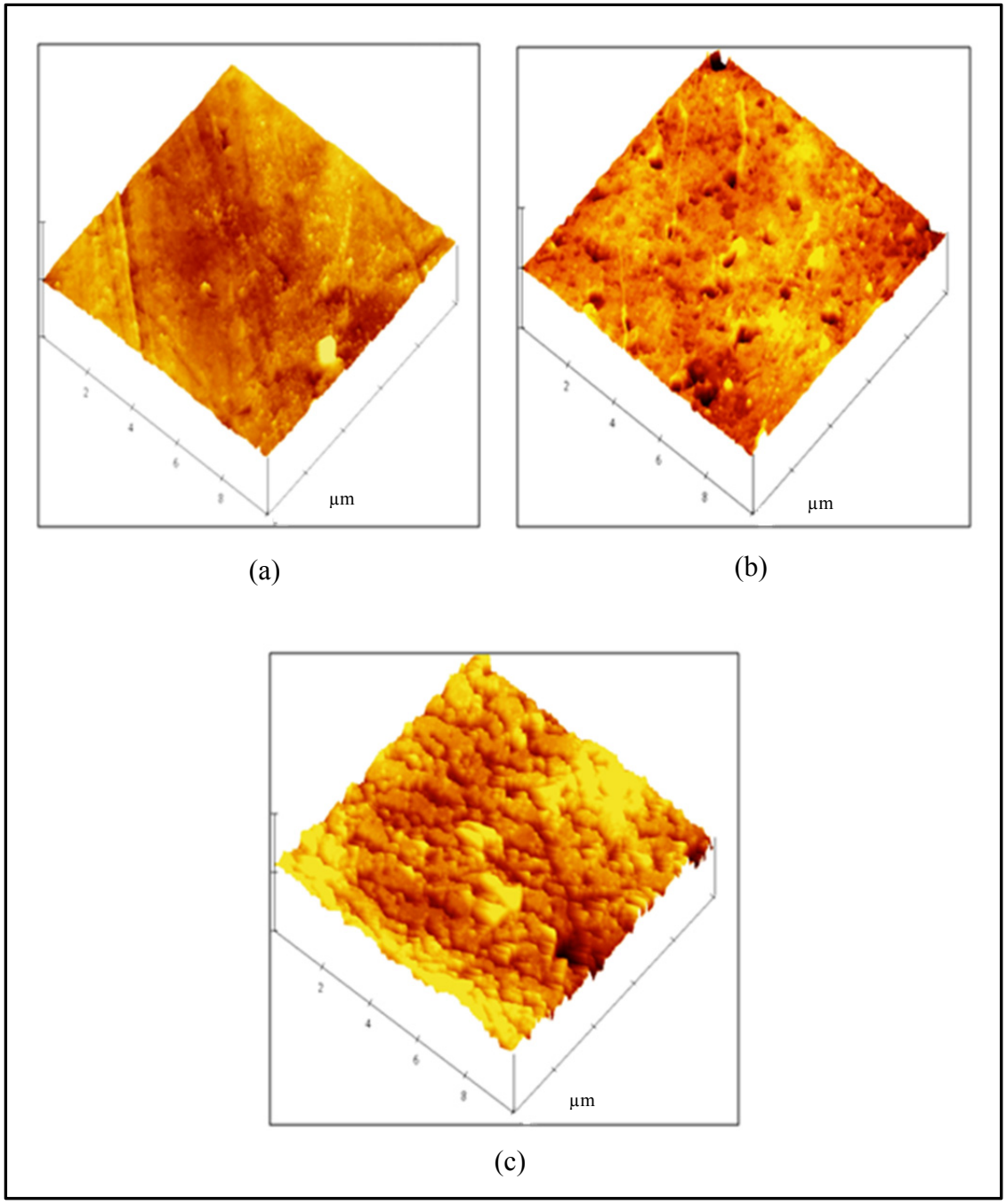

Figure 4.2 AFM height images of (a) neat PE, (b) PE/O-MMT and (c) PE/O-MMT/PE-MA

4.4.3 Clay Dispersion by TEM

Because of the small size of the region examined by TEM, the description of the quality of dispersion was qualitative. Low (I) and high (II) magnification TEM micrographs of PE/O-MMT and PE/O-MMT/PE-MA are shown in Figure 4.3. It can be seen that clay is presented as tactoids in the PE/O-MMT nanocomposites (Figure 4.3 (a)). When the compatibilizer was added, the microstructure of the nanocomposites was presented as a combination of intercalated and exfoliated nanoclay layers (Figure 4.3 (b)). A better dispersion of the clay platelets was achieved for PE/O-MMT/PE-MA than for the nanocomposites without a compatibilizer. This result is in agreement with our previous SEM and XRD measurements (Zazoum, David et Ngô, 2013).

4.4.4 Thermal Properties

Figure 4.4 shows the TGA curves for neat PE, and its nanocomposites PE/O-MMT and PE/O-MMT/PE-MA in air atmosphere. The thermal degradation parameters derived from these curves are given in Table 4.3. It is apparent from these results that the initial degradation temperatures for both nanocomposites are higher than for the neat PE. For PE/O-MMT/PE-MA the decomposition temperatures $T_{10\%}$ and $T_{50\%}$ at 10 % and 50 % weight loss, respectively, of these compatibilized nanocomposites were slightly higher than the PE/O-MMT nanocomposites. This improvement can be due to maleic anhydride polyethylene. It has been reported (Morawiec et al., 2005) that in the presence of this kind of compatibilizer, more intercalation/exfoliated layers can be formed in the polymer matrix, and that there is an improvement in the barrier action for diffusion of oxygen into the nanocomposites which can inhibit material decomposition in air.

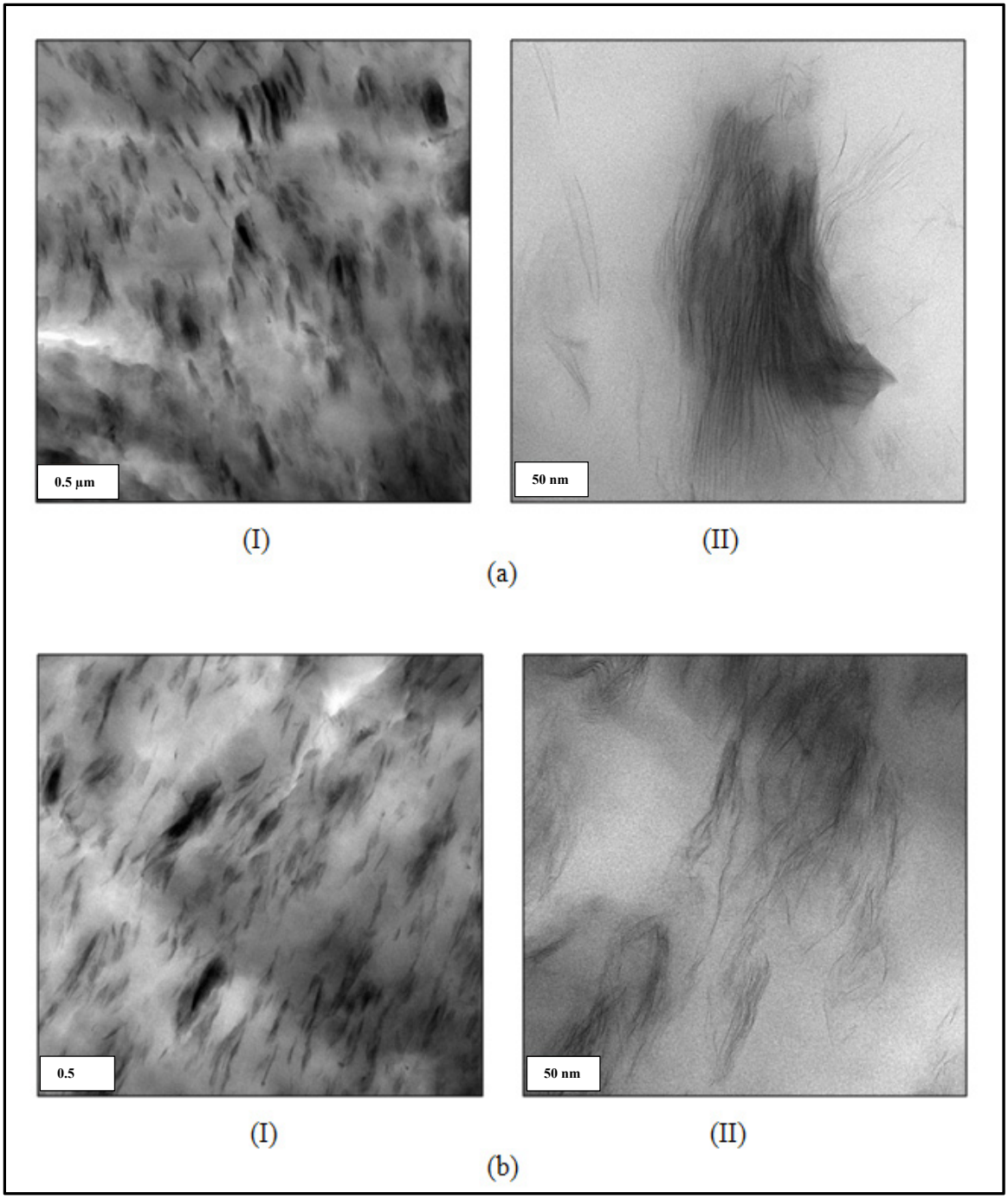

Figure 4.3 Low (I) and high (II) magnification TEM images of nanocomposites: (a) PE/O-MMT and (b) PE/O-MMT/PE-MA

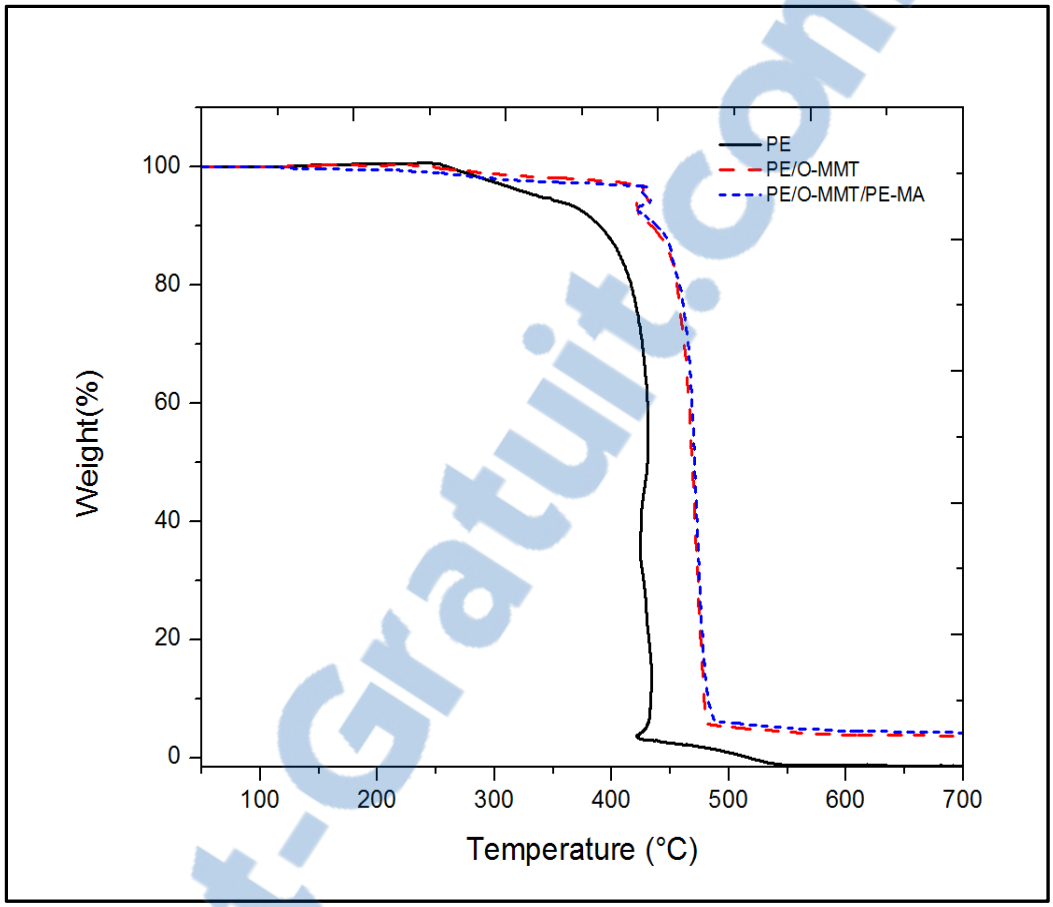

Figure 4.4 TGA decomposition curves of neat PE and its nanocomposites in air environment

Tableau 4.3 TGA data of PE and its nanocomposites in air atmosphere

Samples	**$T_{10\%}$ (°C)**	**$T_{50\%}$ (°C)**	**Loading (wt %)**
PE	389.38	430.00	0
PE/O-MMT	434.06	468.59	3.88
PE/O-MMT/PE-MA	440.16	471.63	3.89

Rapport-Gratuit.com

The thermal scans of PE, PE/O-MMT and PE/O-MMT/E226 nanocomposites in nitrogen atmosphere are shown in Figure 4.5 and the degradation temperatures as well as ash content are depicted in Table 4.4. These results show that the thermal stability of the nanocomposite materials is enhanced when compared to that of the neat PE. On the other hand, it can be seen that the TGA thermogram in nitrogen atmosphere related to PE/O-MMT nanocomposites is superimposed over that of PE/O-MMT/PE-MA.

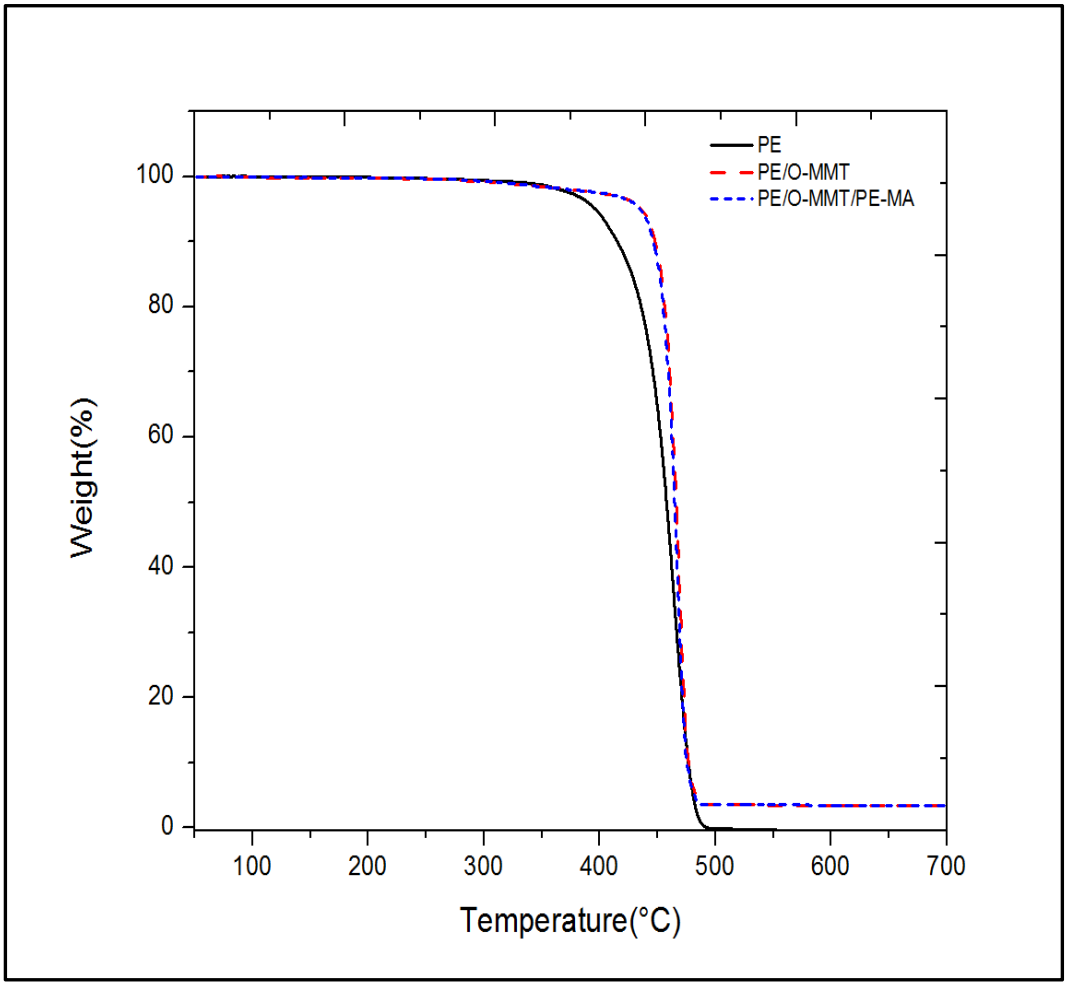

Figure 4.5 TGA decomposition curves of neat PE and its nanocomposites in a N_2 environment

Tableau 4.4 TGA data of PE and its nanocomposites in nitrogen atmosphere

Samples	$T_{10\%}$ (°C)	$T_{50\%}$ (°C)	Loading (wt %)
PE	413.75	456.40	0
PE/O-MMT	446.25	464.53	3.42
PE/O-MMT/PE-MA	448.28	466.56	3.40

4.4.5 Dynamic mechanical behavior

Thermo-mechanical analysis using DMTA was used to understand the evolution of the viscoelasticity of the nanocomposites over a wide range of temperatures. This technique provides better information on the quality of dispersion of the nanoclay filler in the polymer matrix (Lonkar et al., 2012; Venkatesh et al., 2012). The storage modulus E' and loss modulus E'' curves of PE and its nanocomposites are depicted in Figures 4.6 and 4.7, which show the variation of storage and loss modulus, respectively, as a function of temperature. It is evident that the E' of neat PE and its nanocomposites decreases with an increase in temperature. This is due to the increase in the molecular motion of the polymer chains when the temperature increases. As depicted in Table 4.5 and Table 4.6, it was found that the incorporated O-MMT improved the storage and loss modulus; at room temperatures (25 °C), the storage and loss moduli increased from 0.474 GPa and 0.054 GPa, respectively, in the neat PE blend to 0.561 GPa, and 0.071 GPa, respectively, in the PE/O-MMT nanocomposites. This noticeable improvement in the thermo-mechanical stability of these nanocomposites materials from low to high temperatures was caused by the strong interactions between the interface of exfoliated/interacted nanoclay layers and the polymer matrix (Vaia, Teukolsky et Giannelis, 1994). On the other hand, compatibilized nanocomposites showed slightly higher storage and loss moduli than nanocomposites without

Rapport-gratuit.com
LE NUMERO 1 MONDIAL DU MÉMOIRES

compatibilizer. These results clearly show that the storage modulus value is correlated with the quality of dispersion in nanocomposites materials (Lertwimolnun et Vergnes, 2005).

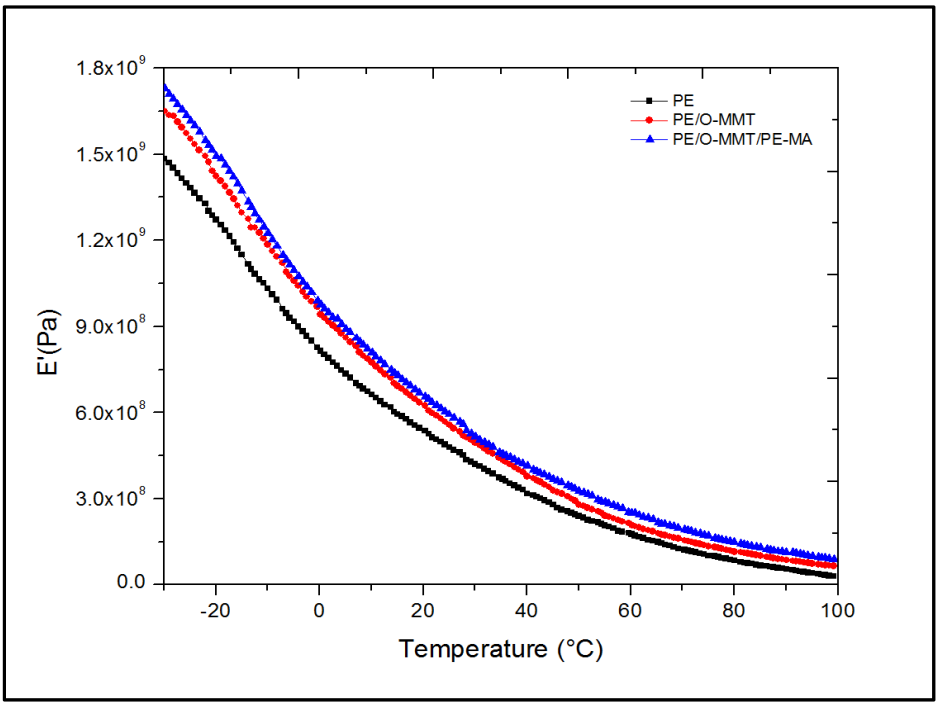

Figure 4.6 Storage modulus E′ of neat PE, PE/O-MMT and PE/O-MMT/PE-MA nanocomposites as function of temperature at 1 Hz

Tableau 4.5 Effect of O-MMT clay and compatibilizer on storage modulus *E′* at different temperatures

Storage Modulus, *E′* (GPa)			
Samples	**-30 °C**	**25 °C**	**90 °C**
PE	1.485	0.474	0.051
PE/O-MMT	1.651	0.561	0.095
PE/O-MMT/PE-MA	1.725	0.594	0.117

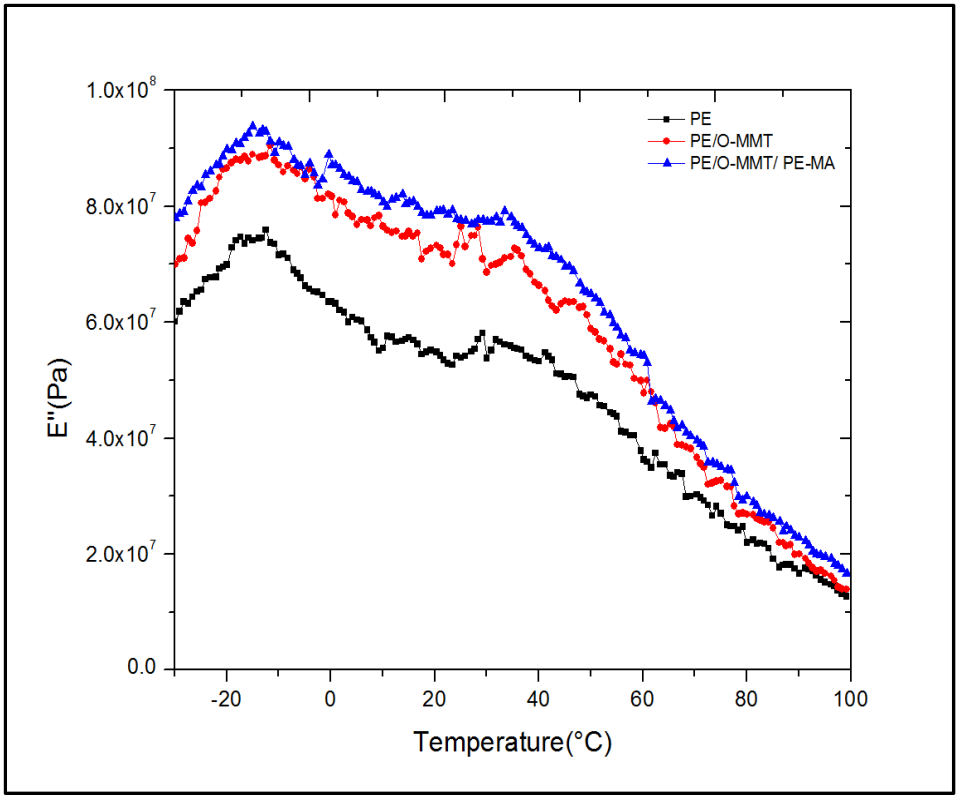

Figure 4.7 Loss modulus E″ of neat PE, PE/O-MMT and PE/O-MMT/PE-MA nanocomposites as function of temperature at 1 Hz

Tableau 4.6 Effect of O-MMT clay and compatibilizer on loss modulus *E″* at different temperatures

Loss Modulus, E″ (GPa)			
Samples	**-30 °C**	**25 °C**	**90 °C**
PE	0.060	0.054	0.017
PE/O-MMT	0.069	0.071	0.020
PE/O-MMT/PE-MA	0.076	0.077	0.023

4.4.6 Dielectric breakdown measurements

A typical image of a breakdown path for a PE/O-MMT sample in 2D and 3D presentation is shown in Figures 4.8 (a) and 4.8 (b), respectively. In addition, Figure 4.9 shows the Weibull cumulative failure probability plot for the dielectric strength of pure PE and its nanocomposites. As reported in Table 4.7, for PE, PE/O-MMT and PE/O-MMT/PE-MA, the scale parameters α were 70.3, 82.4 and 85.7 kV/mm, respectively, and the shape parameters β were 18.6, 13.2 and 10.8, respectively. It can clearly be observed from the scale parameter values α and from the confidence intervals that adding O-MMT to the polyethylene matrix leads to a noticeable increase in the material dielectric strength. This could be explained by the major role played by the interface between the PE matrix and the nanoclay particles, which could have an impact on the space charge distribution and charge densities. In turn, this probably led to a better distribution of the electrical stress (Nelson et Fothergill, 2004). When the compatibilizer was added to PE/O-MMT nanocomposites, a further improvement of the breakdown strength was noted. A possible explanation relates to the change of microstructure which occurred with the addition of the compatibilizer into the PE/O-MMT nanocomposites. This change of microstructure was already underlined by the microscopic observation results discussed above.

The shape parameter value β decreases when O-MMT is added to the PE matrix. With this parameter being an indication of the data's scattering, this could indicate either a non-uniform dispersion of the O-MMT or a partial exfoliation of the O-MMT (Hoyos et al., 2008a).

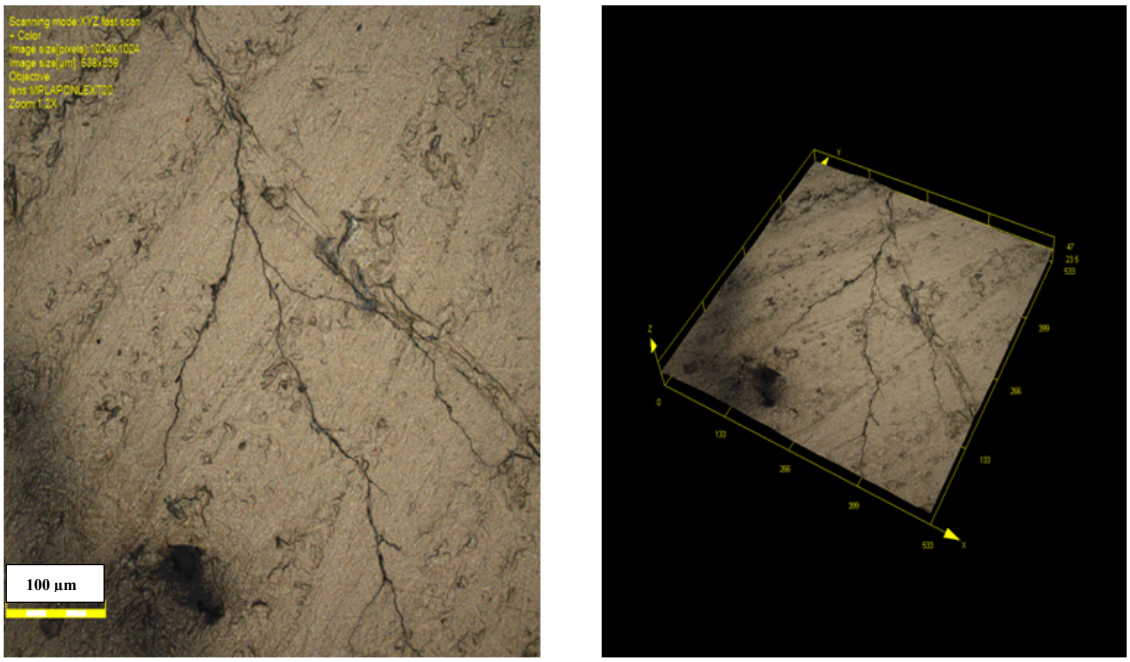

(a) (b)

Figure 4.8 Typical breakdown path for PE/O-MMT in (a) 2D and (b) 3D visualizations, observed by high resolution optical microscope

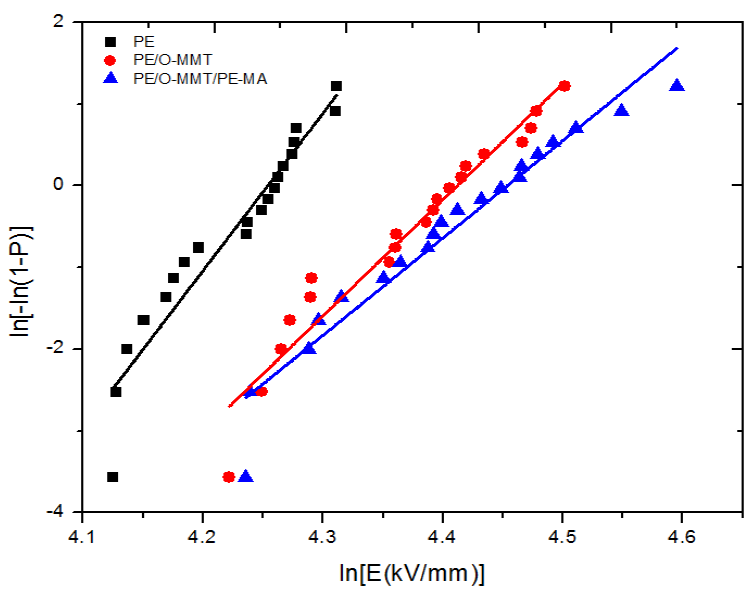

Figure 4.9 Weibull probability plot of dielectric strength of neat PE, PE/O-MMT and PE/O-MMT/PE-MA

Tableau 4.7 Weibull parameters for dielectric breakdown strength of PE and its nanocomposites

Samples	**α (kV/mm)**	**β**	**90 % confidence intervals for α (kV/mm)**
PE	70.3	18.6	[68.7, 71.7]
PE/O-MMT	82.4	13.2	[79.8, 84.7]
PE/O-MMT/PE-MA	85.7	10.8	[82.4, 88.7]

4.5 Conclusion

A commercial nanoclay masterbatch was used in this study to prepare PE/clay nanocomposites. The effect of O-MMT clay and compatibilizer on the structure and dielectric breakdown behaviour in PE was investigated. Microstructure characterizations by microscopic observation revealed that nanoclay layers were more intercalated/exfoliated in PE/O-MMT/PE-MA than in PE/O-MMT, thanks to presence of a compatibilizer. These results are in agreement with TGA and DMTA measurements. Dielectric strength measurements showed that in PE/O-MMT nanocomposites, significant improvements in dielectric breakdown strength can be reached, as compared to neat PE. When the compatibilizer was added to PE/O-MMT nanocomposites, a further improvement in breakdown strength was noticed. This may suggest a correlation between morphology and breakdown strength, and that dielectric characterization, especially breakdown strength and dielectric response (Zazoum, David et Ngô, 2013) measurements, can be exploited as an indirect technique for evaluating the degree of dispersion of nanoclay layers in polymer nanocomposites. Further studies will be necessary to confirm the results obtained.

Acknowledgment

The authors are grateful for the financial support from the National Sciences and Engineering Research Council of Canada (NSERC). TEM measurements were performed in FEMR at McGill University, Montreal, Canada. The authors thank Kelly Sears, Liu David and Jeannie Mui, for assistance with TEM.

Conflict of Interests

The authors declare that there is no conflict of interests regarding the publication of this paper.

CHAPITRE 5

ARTICLE III: Structural and Dielectric Studies of LLDPE/O-MMT Nanocomposites

B. Zazoum, E.David and A.D. Ngô
Département de génie mécanique (Mechanical Engineering Department), École de technologie supérieure (ETS), 1100 Notre-Dame Ouest, Montréal QC H3C 1K3, Canada
Article accepté dans la revue «Transactions on Electrical and Electronic Materials» en Juin 2014. Numéro de confirmation: 14-0044

Abstract

Nanocomposites made of linear low density polyethylene (LLDPE) and organo-modified montmorillonite (O-MMT) were processed by melt compounding from a commercially available premixed LLDPE/nanoclay masterbatch, at different nanoclay loadings, using a co-rotating twin-screw extruder. The morphological and dielectric properties of LLDPE/O-MMT nanocomposites were investigated to understand the structure-dielectric properties relationship in the nanocomposites. The microstructures of the materials were characterized by wide angle X-ray diffraction (WAXD), scanning electron microscopy (SEM), transmission electron microscopy (TEM) and atomic force microscopy (AFM). Initial findings by FTIR spectroscopy characterization indicated the absence of any chemical interaction between LLDPE and nanoclay during the extrusion process, while DSC showed that a 1% wt loading of nanoclay particles increases the degree of crystallinity of the nanocomposites samples. On the other hand, XRD, SEM, TEM and AFM indicated that nanoclay layers were intercalated or exfoliated in the LLDPE matrix. A correlation between the structure and dielectric properties of LLDPE/O-MMT nanocomposites was found and discussed.

Keywords: LLDPE/O-MMT nanocomposites, microstructure, dielectric response, breakdown strength.

Rapport-Gratuit.com

5.1 Introduction

Polyethylene is extensively used as ground wall insulation in high and medium voltage electric cables due to its good electrical insulating properties. However, many of its physical properties need to be improved in order to broaden its engineering application. It has been observed that adding a small amount of nanoclay to some thermoplastics as reinforcing fillers to form nanocomposites material lead not only to an improvement of the mechanical and thermal properties (Han et al., 2001; Hotta et Paul, 2004; Kawasumi et al., 1997; Utracki et Kamal, 2002), but also to an enhancement of the dielectric properties of these materials (AWAJI et al., 2009; Chen et Chen, 2009; Kim et al., 2009; Kornmann, Lindberg et Berglund, 2001; Tan et Yang, 1998; Zhao et He, 2006).

There are three typical different processing procedures for preparing nanocomposites: (1) in-situ polymerization, (2) solution blending, and (3) melt compounding. The latter is considered to be the most convenient and effective technique for producing nanocomposites, and uses twin-screw extruder. The procedure offers economic benefits and ecological advantages.

The morphology of polymer clay nanocomposites can be classified into three different structures: (1) unmixed nanocomposites, in which polymer chains do not penetrate between silicate layers; (2) intercalated nanocomposites, in which polymer chains are intercalated between silicate layers, and (3) exfoliated nanocomposites, in which the organoclay plates are separated by an average distance which depends on the organoclay plates concentration, and the individual silicate layers are randomly distributed in the polymer matrix. In this case, the X-ray diffraction does not show any 001 diffraction peak. The main problem in the fabrication of nanocomposites is the dispersion of the individual clay platelets into the polyethylene matrices due to the incompatibility of hydrophobic polyolefin with hydrophilic nanoclay (Osman, Rupp et Suter, 2005). To render clay platelets compatible with the polymer matrix, a surface treatment, which uses quaternary alkyl ammonium cations (Zhang et al., 2005), is completed via ion-exchange reactions with cationic surfactants.

The purpose of this paper is to examine the effect of nanoclay dispersion and to understand the relationship between the structure and dielectric properties of LLDPE/O-MMT nanocomposites.

5.2 Experiment

5.2.1 Materials

Linear low density polyethylene (LLDPE, FPs117, NOVA Chemicals), with a melt flow index (MFI) of 1 g/10 min and a density of 0.917 g/cm^3, was used as matrix. A commercial masterbatch of LLDPE/O-MMT (NanoMax) containing 50 wt % of organo-modified Montmorillonite (O-MMT) was supplied by Nanocor. Maleic anhydride grafted linear low density polyethylene (LLDPE-g-MA, Fusabond® M603, DuPont), having a density of 0.940 g/cm^3 and MFI of 25 g/10 min, was used as a compatibilizer.

5.2.2 Sample preparation

The LLDPE, M603 and commercial master-batch of LLDPE/O-MMT were dried at 40 °C in a vacuum oven for a minimum of 48 hrs prior to extrusion. Nanocomposites were prepared by an extrusion process using a co-rotating twin screw extruder (Haake Polylab Rheomex OS PTW16, D = 16mm, L/D = 40), coupled with a Haake Metering Feeder in order to control the feed rate. The temperature profile from hopper to die used in this study was 140 °C - 180 °C, the feed rate was fixed at 1 kg/h, and the screw speed was set at 140 rpm. All materials were pre-mixed manually before introduction into the twin-screw extruder.

The pellets obtained after extrusion were press-molded to form thin plates (590 µm thickness) using an electrically heated hydraulic press. The molding temperature and pressure were 178 °C and 5 MPa, respectively. A summary of the compositions of the LLDPE/clay nanocomposites used is collected in Table 5.1.

Rapport-gratuit.com
LE NUMERO 1 MONDIAL DU MÉMOIRES

Tableau 5.1 Samples formulation and designation

Samples designation	LLDPE (wt %)	O-MMT (wt %)	LLDPE-g-MA (wt %)
MB	50	50	0
LLDPE	100	0	0
LLDPE+1% O-MMT	99	1	0
LLDPE+3% O-MMT	97	3	0
LLDPE+3% O-MMT+10% M603	87	3	10
LLDPE+5% O-MMT	95	5	0

5.3 Characterization and measurements

5.3.1 X-ray diffraction (XRD)

The characterization of nanocomposite structure was performed using an X-ray diffractometer (PANanalytical X'Pert Pro) with Kα radiation (λ = 1.5418Å), at an accelerating voltage of 40 kV and an electrical current of 45 mA. The scanning was conducted from 2° to 9° with a step size of 0.0334° and the counting time was 200 ms per step. The intercalate spacing between the planes in the atomic lattice d_{001} was calculated by using Bragg's law:

$$2\,d\,\sin\theta = \lambda \tag{5.1}$$

5.3.2 Transmission electron microscopy (TEM)

The degree of dispersion of the nanoclays in the polymer matrix was examined by transmission electron microscopy (TEM). Ultra-thin sections of 50-80 nm in thickness were cut from the molded plaque of LLDPE/O-MMT nanocomposites at -120 °C, using an ultramicrotome equipped with a diamond knife. These samples were then examined using a high-resolution JEOL JEM-2100F TEM with an accelerating voltage of 200 kV.

5.3.3 Atomic force microscopy (AFM)

The morphological investigations of the LLDPE/clay nanocomposites were carried out using an Atomic Force Microscopy (DiNanoScope, Vecco, USA) in tapping mode. The images of the surface topography were then analyzed using the Nanoscope (R) III software, Version 5.30r.sr3. Samples with a thickness of 560 µm were used, and all measurements were carried out at ambient conditions.

5.3.4 Scanning electron microscopy (SEM)

The samples' micro-structure was examined using a Hitachi scanning electron microscopy (SEM). Samples were first embrittled in liquid nitrogen and then snapped off by hand and coated with a 2 nm platinum layer in order to avoid electrostatic charging during the microscopic observations.

5.3.5 Differential scanning calorimetry (DSC)

The thermal behavior of pure LLDPE and LLDPE/O-MMT nanocomposites was observed using a Perkin-Elmer Differential Scanning Calorimeter Pyris 1 instrument. The temperature calibration of the DSC was performed using indium. During each run, the LLDPE and its nanocomposites were heated from 30 °C to 180 °C, at a heating rate of 10 °C/min in nitrogen atmosphere.

5.3.6 Fourier transform infrared spectroscopy (FTIR)

Fourier transform infrared (FTIR) spectra were obtained using a Thermo Electron Nicolet 6700 FT-IR spectrometer instrument. Thin film samples were cut from the compression-molded sheet films. The measurements were carried out at a spectral resolution of 4 cm^{-1} in the 400-4000 cm^{-1} wavenumber range, with accumulations of 32 scans at room temperature. Spectra were collected in transmittance mode.

5.3.7 Dielectric relaxation spectroscopy

Dielectric relaxation spectroscopy experiments were carried out using a Novocontrol alpha-N Analyzer in the 10^{-2} to 10^{5} Hz frequency domain at temperatures of 40 °C. The temperature was controlled using a Novotherm system, with a stability of 0.5 °C.
The samples were sandwiched between two gold-plated electrodes measuring 40 mm in diameter to form a parallel-plate geometry capacitor.
The obtained complex dielectric permittivity is given by:

$$\varepsilon^*(\omega) = \varepsilon'(\omega) - i\varepsilon''(\omega) \tag{5.2}$$

where $\varepsilon'(\omega)$ represents the real part, $\varepsilon''(\omega)$ represents the imaginary part, and $\omega = 2\pi f$ is the angular frequency.

5.3.8 Dielectric breakdown strength

The dielectric breakdown field was measured according to the ASTM D 149 standard. The specimens were placed between two 12.5 mm hemispherical electrodes and held by a small applied pressure. The whole setup was immerged in mineral oil (Voltesso 35, ESSO Imperial Oil). The rate-of-rise was set to 2 kV/s, and a 60 Hz voltage was raised until the sample breakdown.

The two-parameter Weibull statistical distribution (Std-930, 2004) was used to treat the dielectric strength data. The Weibull statistical distribution in the case of two-parameters can be written as follows:

$$P(E) = 1 - \exp[-(E/\alpha)^{\beta}] \tag{5.3}$$

where P(E) denotes the cumulative distributive function of dielectric strength, E is the experimental dielectric strength, α is the scale parameter which represents the breakdown strength at P(α)=0.632, and finally, β is a shape parameter related to the data scattering. According to the IEEE 930-2004 standard, the experimental probability of failure P (i,n) associated with the E_i data can be approximated by:

$$P(i,n) = \frac{i-0.44}{i+0.25} \tag{5.4}$$

where i is the ith result when the breakdown values are sorted in ascending order, and n is the number of data points. In this paper, n = 20.

The commonly used 90 % confidence intervals have been used to compare sets of data by verifying the overlapping of the confidence limits at the 63.2^{th} percentile.

5.4 Results and discussion

5.4.1 X-ray diffraction (XRD) technique

Figure 5.1 shows the X-ray diffraction spectra of the O-MMT masterbatch (MB), LLDPE+3% O-MMT and LLDPE+3% O-MMT+10% M603 nanocomposites. The d_{001} diffraction peak for the O-MMT masterbatch is about 2θ = 3.13°, corresponding to a basal spacing d_{001} of 2.82 nm. When the O-MMT masterbatch was diluted with pure LLDPE, the diffraction peak was found to shift to a smaller angle, indicating the increase in d_{001} spacing of the galleries of the organoclay. For the ternary nanocomposites LLDPE+3% O-

MMT+10% M603, the reduction in the diffraction intensity and the disappearance of the basal peak suggested that O-MMT is exfoliated in the polymer matrix.

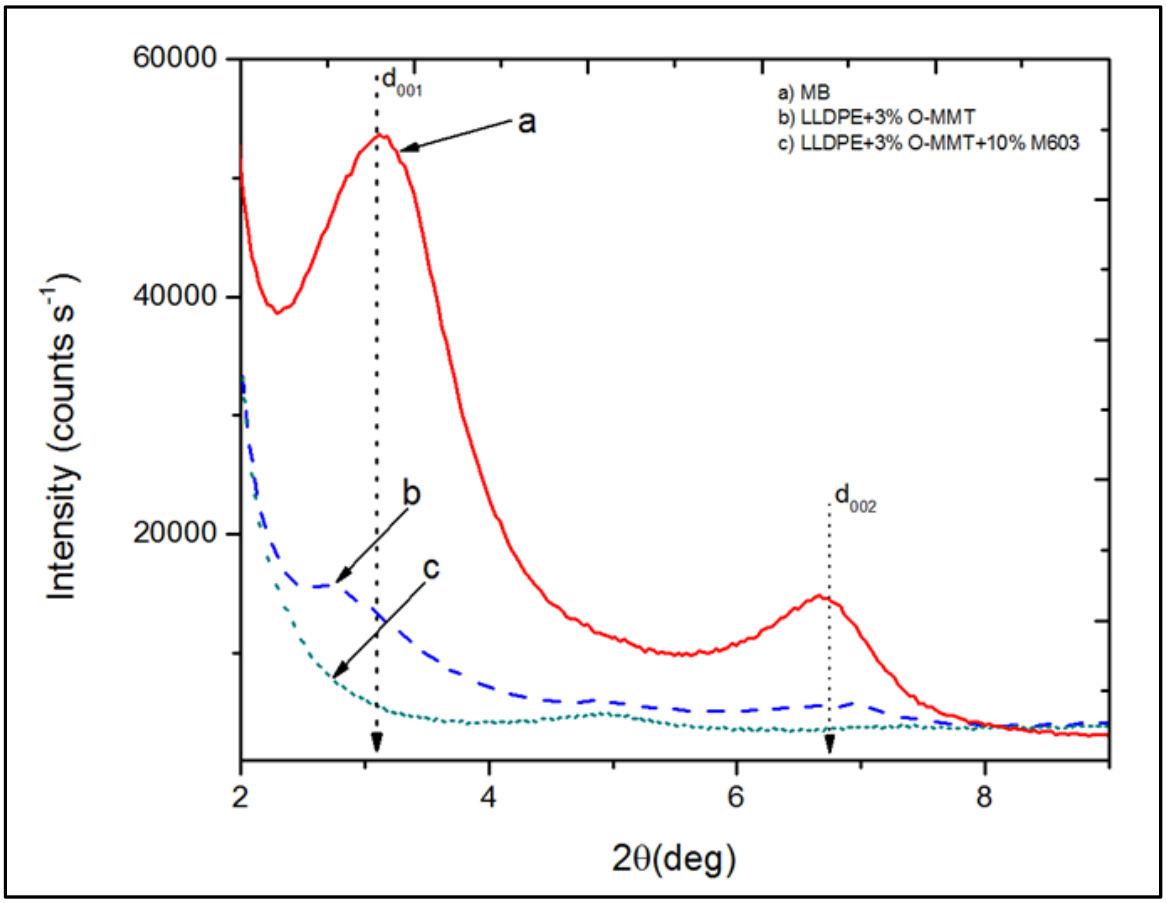

Figure 5.1 X-ray diffraction spectrum of LLDPE/clay nanocomposites

5.4.2 Microstructure of nanocomposites

Transmission electron microscopy was employed in order to directly visualize the nanocomposites' structure and to confirm XRD information about the quality of dispersion for silicate platelets in the polymer matrix. TEM micrographs of LLDPE+3% O-MMT and LLDPE+3% O-MMT+10% M603 are shown in Figure 5.2. It can be seen that clay is presented as tactoids in the LLDPE+3% O-MMT nanocomposites (Figure 5.2 (a)). Obviously, when the compatibilizer is added, the microstructure of the nanocomposites is

significantly improved, and it is presented as a combination of intercalated and exfoliated nanoclay layers (Figure 5.2 (b)).

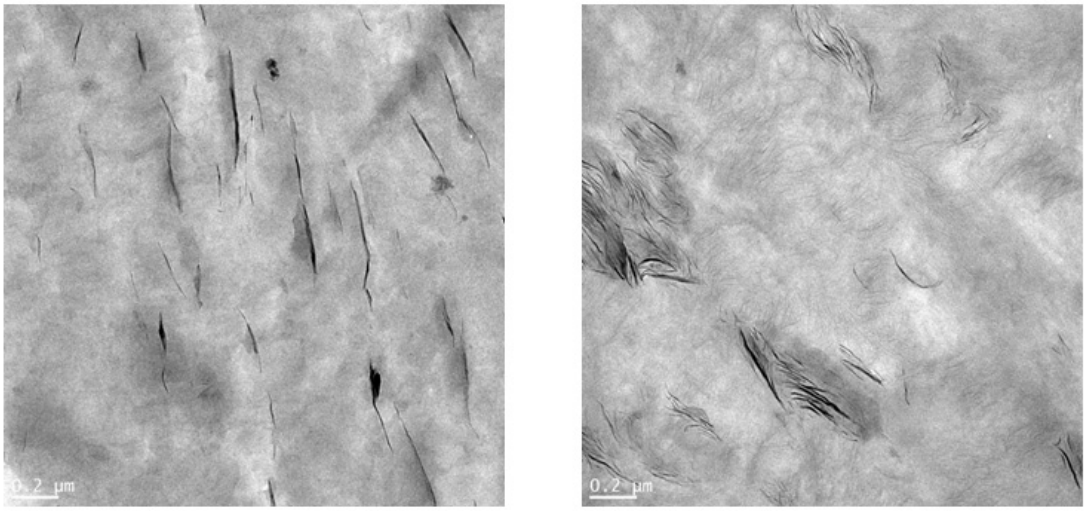

(a) (b)

Figure 5.2 TEM Micrographs of (a) LLDPE+3%O-MMT and
(b) LLDPE+3% O-MMT+10% M603

5.4.3 Atomic force microscopy

AFM height images of LLDPE+3% O-MMT and LLDPE+3% O-MMT+10% M603 were used in order to study the dispersion of nanoclay in the polymer matrix. The surface properties of these two nanocomposites in 3D height image are shown in Figures 5.3 (a) and 5.3 (b). From the images, the nanoclay appears brighter than the polyethylene matrix. It is obvious that in the compatibilized nanocomposites, the agglomerates are broken into small tactoids and the nanoclays are more homogeneously distributed in the polymer matrix. This leads to a reasonably good dispersion of nanoclay in LLDPE+3% O-MMT+10% M603 nanocomposites (Hong et Rhim, 2012). These obtained results are also well corroborated by XRD and TEM measurements.

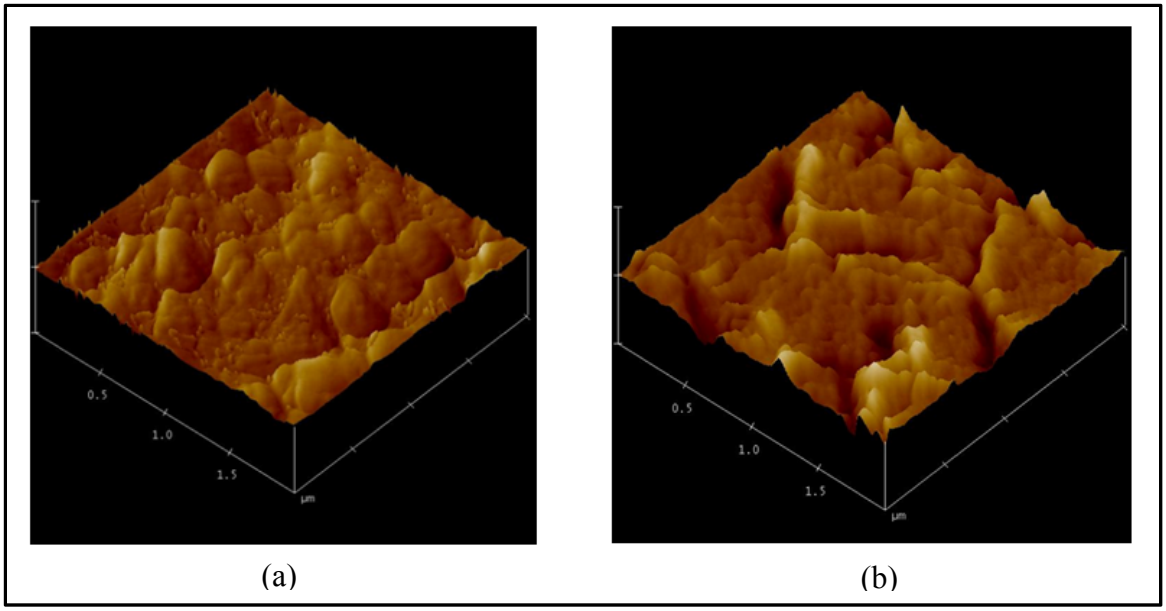

(a) (b)

Figure 5.3 AFM images of (a) LLDPE+3% O-MMT and
(b) LLDPE+3% O-MMT+10% M603 nanocomposites

5.4.4 Thermal Properties

Differential scanning calorimetry (DSC) was used to measure the melting temperature and the fusion enthalpy ΔH_F. The degree of crystallinity was calculated as

$$\% \chi = \frac{\Delta H_F}{\Delta H_F^0 (1-\varphi)} \tag{5.5}$$

where ΔH_F is the heat of fusion (J/g), ΔH_F^0 is the theoretical heat of fusion of 100 % crystalline LLDPE (293 J/g) and φ is the weight fraction of O-MMT.

DSC numerical data of LLDPE and its nanocomposites are reported in Table 5.2. It can be seen that the addition of nanoclay to the LLDPE matrix had no significant impact on the melting temperature for all the samples. However, the crystallinity of LLDPE/O-MMT samples was found to increase at concentrations of nanoclay of 1 wt %. This observation could be explained by the fact that nanoclay layers acted as nucleating agents and facilitated the crystal growth. On the other hand, the degree of crystallinity was found to slightly

decrease with further increases of nanoclay concentration (5 wt %). A possible explanation for this could be that intercalated nanoclay layers of O-MMT limit the growth of the polymer spherulites.

Tableau 5.2 DSC results for pure LLDPE and LLDPE/O-MMT nanocomposites

Samples	**Melting Point (°C)**	**Crystallinity (%)**
LLDPE	107.7	33.7
LLDPE+1% O-MMT	108.0	36.8
LLDPE+3% O-MMT	107.1	35.3
LLDPE+3%O-MMT+10% M603	107.1	35.2
LLDPE+5% O-MMT	107.7	34.0

5.4.5 FTIR Spectroscopy

Transmittance Fourier Transform Infrared Spectroscopy was used to quantify the possible thermal degradation and monitor the motion of molecular chain of pure LLDPE and LLDPE/O-MMT nanocomposites.

Figure 5.4 shows the infrared spectra of LLDPE (0 run), LLDPE (1 run) and LLDPE/O-MMT (1 run) nanocomposites with different O-MMT contents. Comparing the infrared spectra of LLDPE (0 run) with that of LLDPE (1 run) indicates the absence of any oxidation phenomena during the one-run extrusion process. The binary nanocomposites LLDPE/O-MMT show only the characteristic peaks for both pure LLDPE and O-MMT. The absence of any new peaks indicates the absence of any chemical reactions between the nanoclay and polymer matrix.

Rapport-Gratuit.com

O-MMT has characteristic peaks at 464 cm^{-1}, 521 cm^{-1} and 1047 cm^{-1}; these bands are related to Si-O bending, Al-O stretching and Si-O stretching, respectively (Madejová, 2003). It can be seen that the intensity of the Si-O stretching band increased as the nanoclay content increased. Vaia et al. (Vaia, Teukolsky et Giannelis, 1994) showed that around 1469 cm^{-1}, the CH_2 rocking band is related to the polymer chain motion, and the shift of this peak to the higher wave number indicates a decrease in the polymer chain mobility. The fact that the characteristic peak of the CH_2 rocking band in LLDPE/O-MMT nanocomposites with 5 wt % of nanoclay content was shifted to higher wavenumber (1471 cm^{-1}) compared to that in pure LLDPE (1469 cm^{-1}) can be explained by the fact that the additional 5 wt % of nanoclay, slowed down the chain motion and therefore decreased the crystallinity. This is in agreement with DSC results.

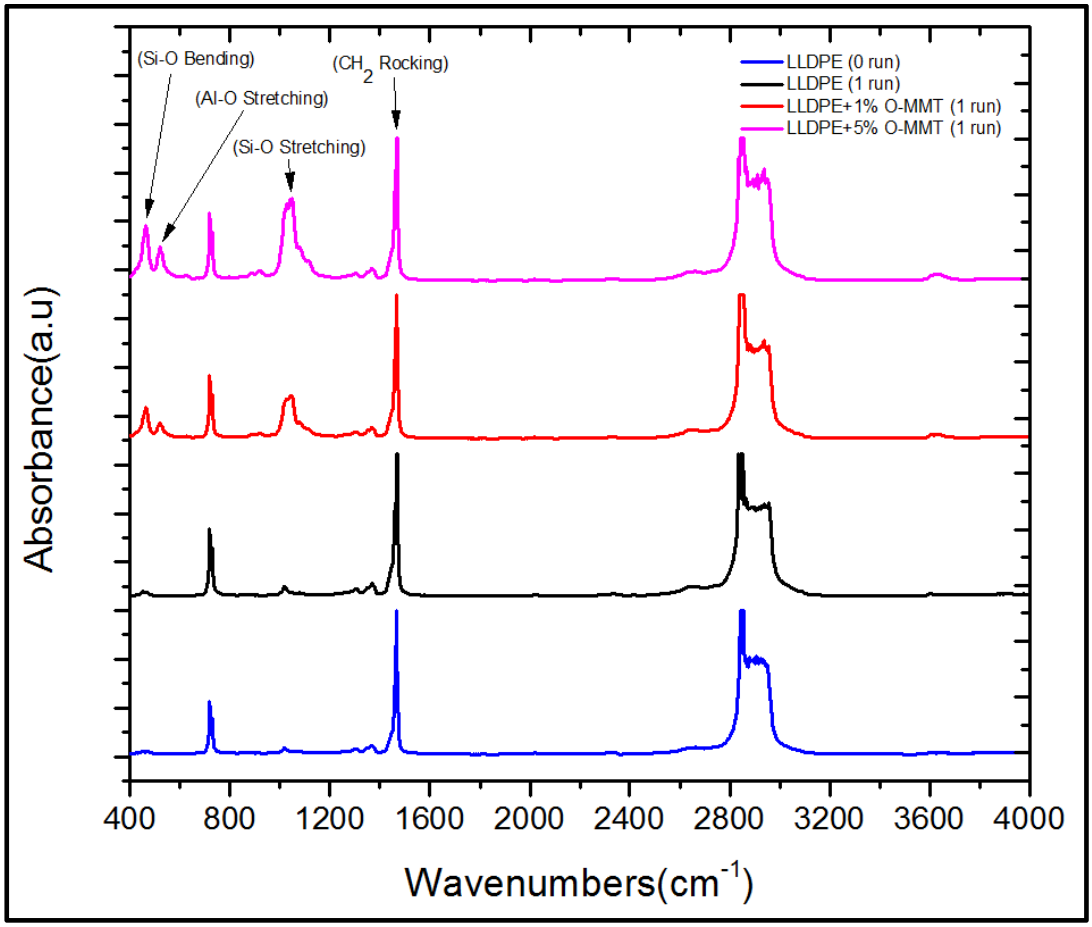

Figure 5.4 FTIR spectra of of LLDPE and its nanocomposites

5.4.6 Effect of screw speed on morphological characterization

To study the effect of screw speed on clay dispersion of nanoclay layers in the polymer matrix, two different speeds (50 rpm and 350 rpm) were selected. The nanoclay content was 3 wt % and the compatibilizer M603 concentration was set at 10 % wt. Figure 5.5 shows the morphology of the ternary nanocomposite LLDPE+3% O-MMT+10% M603 on a nanometric scale, using scanning electron microscope (SEM). A comparison between the morphology of the nanocomposite extruded with a low speed (Figure 5.5 (a)) and that with a high speed (Figure 5.5 (b)) shows that the density and size of aggregates decreased as the screw speed increased. The screw speed led to an improvement in the nanoclay dispersion and to more exfoliated layers.

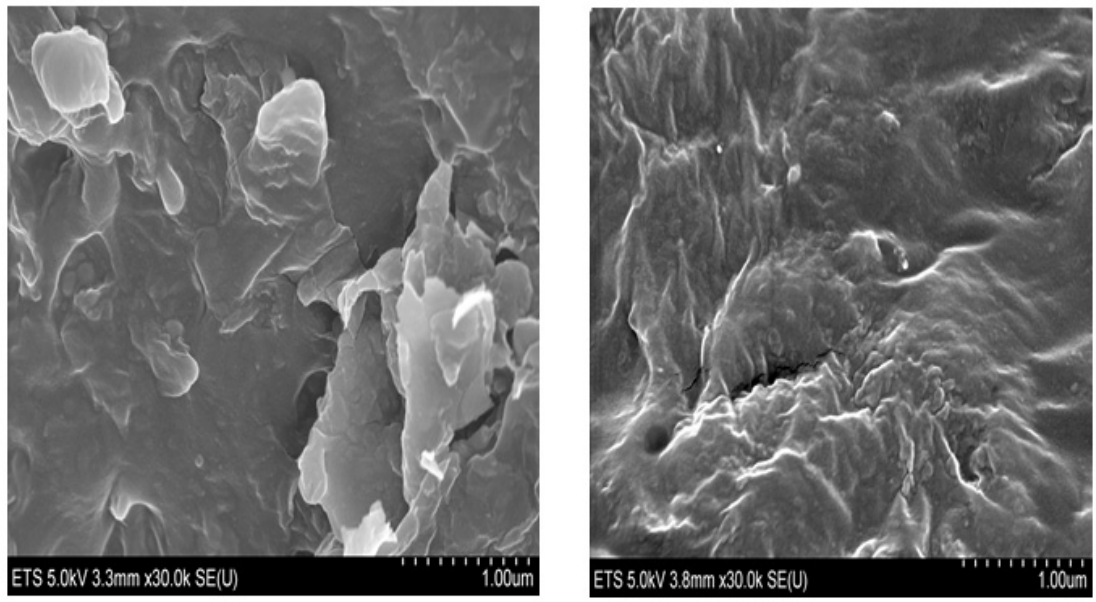

(a) (b)

Figure 5.5 SEM micrograph of LLDPE+3% O-MMT+10% M603 for a screw speed of (a) 50 rpm and (b) 350 rpm

Rapport-gratuit.com
LE NUMERO 1 MONDIAL DU MÉMOIRES

5.4.7 Broadband dielectric spectroscopy

Figure 5.6 shows the dielectric response of LLDPE, LLDPE+1% O-MMT, LLDPE+3% O-MMT, LLDPE+3% O-MMT+10% M603 and LLDPE+5% O-MMT nanocomposites obtained using Frequency-Domain dielectric spectroscopy at 40 °C in the 10^{-2} to 10^{5} Hz frequency range. It can be observed from Figure 5.6 (a) that the relative permittivity ε' of the 1, 3 and 5 wt % LLDPE/O-MMT nanocomposites is sharply decreasing. The corresponding dielectric loss ε'' shows a relaxation peak at around 10^{2} Hz, as shown in Figure 5.6 (b). It is also observed that both real and imaginary permittivity increase with decreasing frequency. It is evident that the ε'' peak observed in the nanocomposites is due to the addition of nanoclay, because there is no dielectric relaxation peaks for pure LLDPE in this frequency range. The peak of the relaxation processes presented in the nanocomposites is attributable to a Maxwell-Wagner-Sillars polarization associated with the blocking of charges at the interfaces between two inhomogeneous phases of different permittivities and conductivities, such as the polymer matrix and the silicates filler (Laredo et al., 2003; Le Huy et Rault, 1994; McCall et Anderson, 1960). Furthermore, when 10 wt % of compatibilizer was used to improve the dispersion of the clay platelets, this relaxation peak was found to shift towards low frequencies.

5.4.8 Dielectric breakdown measurements

Figure 5.7 shows the Weibull cumulative failure probability plot for the dielectric strength of pure LLDPE and its nanocomposites (without confidence bounds, for clarity). As reported in Table 3, for LLDPE, LDPE+1% O-MMT, LLDPE+3% O-MMT, LLDPE+3% O-MMT+10% M603 and LLDPE+5% O-MMT, the scale parameters α were 58.8, 62.9, 66.6, 69.6 and 69.9 kV/mm, respectively, and the shape parameters β were 17.1, 17.9, 18.2 , 17.9 and 12.3, respectively. It can be clearly seen from the scale parameter values α and from the confidence intervals that increasing the O-MMT concentration in a binary nanocomposite leads to a noticeable increase in the material dielectric strength. This could be explained by the major role played by the interface between the LLDPE matrix and the nanoclay particles

which could impact the space charge distribution and charge densities. In turn, this probably led to a better

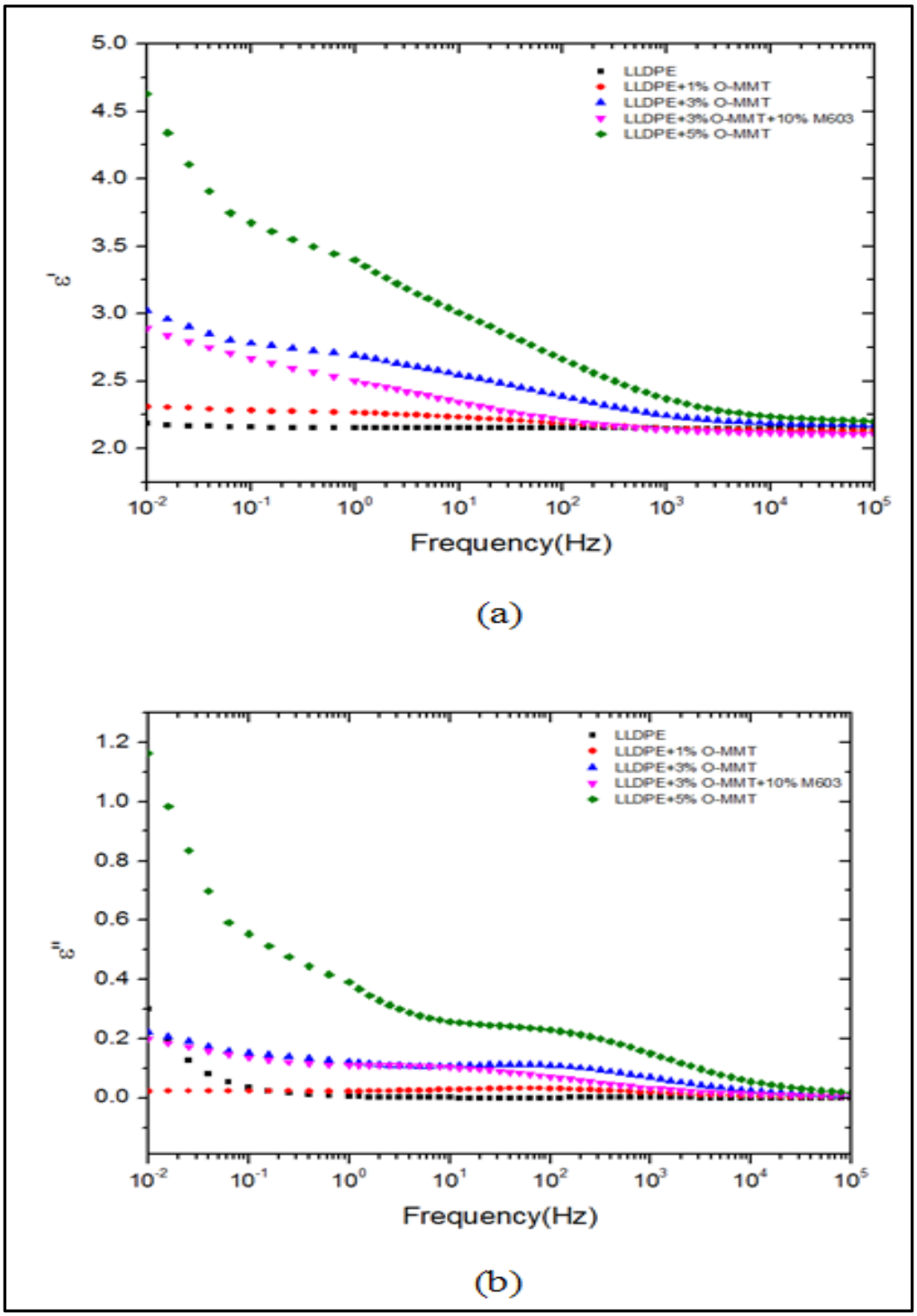

Figure 5.6 Relative permittivity (a) and dielectric losses (b) as a function of frequency of LLDPE and its nanocomposites at 40 ^{o}C

distribution of the electrical stress (Nelson et Fothergill, 2004). When the compatibilizer was added to LLDPE+3% O-MMT nanocomposites, further improvements of the breakdown strength were noticed. A possible explanation for this is related to the change of microstructure which occurred with the addition of compatibilizer into LLDPE+3% O-MMT nanocomposites. This change of microstructure was already underlined by the microscopic observation results discussed above.

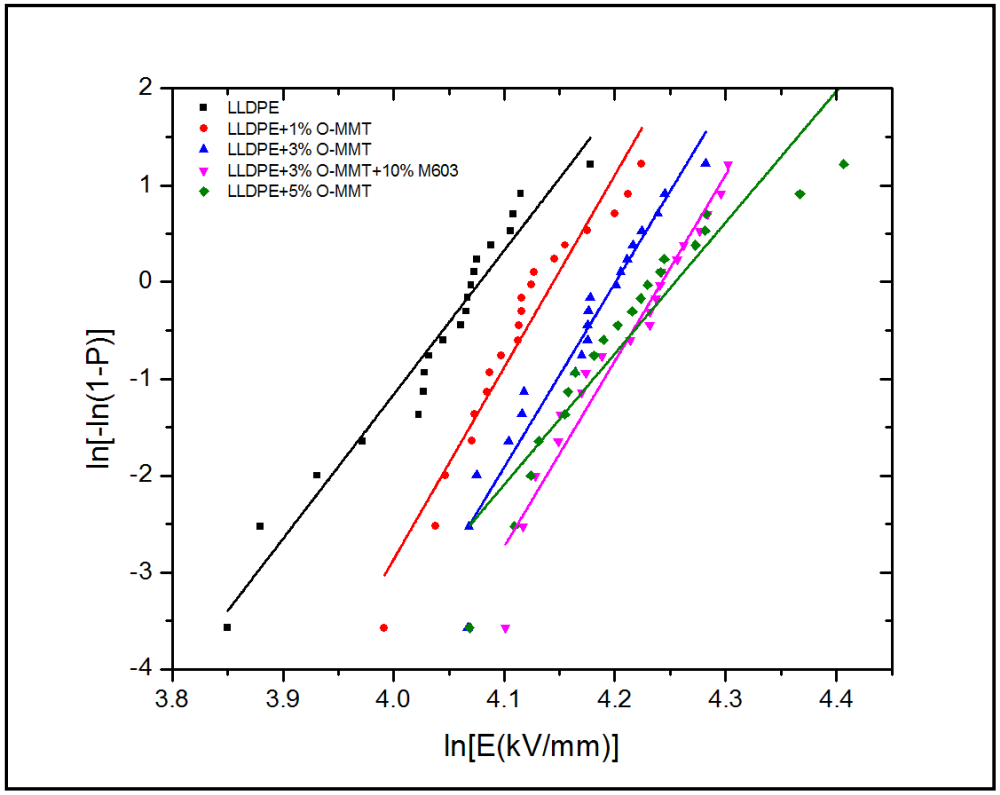

Figure 5.7 Weibull probability plot of dielectric strength of LLDPE and its nanocomposites

Tableau 5.3 Weibull parameters for dielectric breakdown strength of LLDPE and its nanocomposites

Samples	**Average thickness (mm)**	**α (kV/mm)**	**β**	**Confidence intervals for α (kV/mm)**
LLDPE	0.61	58.8	17.1	57.4-60.1
LLDPE+1% O-MMT	0.58	62.9	17.9	61.4-64.2
LLDPE+3% O-MMT	0.57	66.6	18.2	65.1-68.0
LLDPE+3% O-MMT+10% M603	0.56	69.6	17.9	68.0-71.1
LLDPE+5% O-MMT	0.58	69.9	12.3	67.6-72.0

5.5 Conclusion

A commercial nanoclay masterbatch was used in this study to prepare LLDPE/O-MMT nanocomposites. Microstructural characterizations revealed that the degree of dispersion was improved by the incorporation of the compatibilizer. No relaxation peaks were observed in the pure LLDPE, but one was found in the nanocomposites and was attributed to an interfacial process. When the compatibilizer was added, this peak was found to shift towards low frequencies.

Dielectric strength measurements showed that in LLDPE/O-MMT nanocomposites, significant improvements in dielectric breakdown strength can be reached, in comparison with pure LLDPE. It was also shown that the improvement of the quality of dispersion leads to a further improvement in dielectric breakdown strength. This may suggest a correlation between nanocomposite structure and dielectric breakdown strength.

Acknowledgment

The authors are grateful for financial support from the National Sciences and Engineering Research Council of Canada (NSERC). We also thank Professors Abdellah Ajji, Ahmad Zohre Vand and Weawkamol Leelapornpisit from the Department of Chemical Engineering, École Polythechnique de Montréal, for the TEM measurements.

Conflict of Interests

The authors declare that there is no conflict of interests regarding the publication of this paper.

CHAPITRE 6

ARTICLE IV: Simulation and Modeling of Polyethylene/Clay Nanocomposite for Dielectric Application

B. Zazoum, E. David and A.D. Ngô

Department of Mechanical Engineering, École de technologie supérieure (ÉTS), 1100 Notre-Dame Street West, Montreal QC Canada H3C 1K3

Article accepté dans la revue «Transactions on Electrical and Electronic Materials» en Juin 2014. Numéro de confirmation: 14-0028

Abstract

In this paper, the simulation and modeling of polyethylene/clay nanocomposite were developed to predict nanocomposite dielectric behavior and to help design a nanocomposite material with optimum electrical properties for electrotechnical or electronic applications. A 3-D simulation model using the finite elements method was employed in order to study the effective permittivity and electric field distribution of two-phase nanocomposite materials for ordered and random distributions of inclusions in a low-loss host matrix such as polyethylene. The influence of the dispersion of reinforcing particles, and of the permittivity and radius of the inclusions, was analysed. The simulation results were compared with different known theoretical solutions obtained from classical models, and were found to be in good agreement.

Keywords: Dielectric nanocomposites, effective permittivity, modeling, finite elements method.

6.1 Introduction

In recent years, nanocomposites have attracted a great deal of attention from many researchers. Several studies have shown that the incorporation of nanometric inclusions in a polymer matrix can often significantly improve the mechanical, dielectric and optical properties when compared to a pure polymer matrix (David et al., 2013; Han et al., 2001; Hoyos et al., 2008a; Kawasumi et al., 1997; Kornmann, Lindberg et Berglund, 2001; Osman, Rupp et Suter, 2005; Utracki et Kamal, 2002; Vaia, Teukolsky et Giannelis, 1994; Zazoum, David et Ngô, 2013), provided that the particles are reasonably well dispersed. In the electrical insulation field, polyethylene is extensively used in medium/high voltage electrical cables due to its excellent dielectric properties, very low dielectric losses and high intrinsic breakdown strength. In order to improve these properties and be able to meet new needs such as those relating to insulation systems in DC power cables, composite materials consisting of a thermoplastic matrix and nano-filler as reinforcing fillers can be used; this results in a possible increase in breakdown strength, dielectric endurance, thermal conductivity, and allows the electrical conductivity to be tailored to avoid space charge accumulation in DC applications.

The effective permittivity of composite materials generally depends on the material microstructure, which includes the volume fraction, the shapes and the types of the components. For some specific conditions (the mixture has a periodic well-defined structure), the effective permittivity can be calculated from the analytical solution of the field distribution, resulting in various analytical models, such as the commonly used laws of mixtures. However, if the structure is disordered, as may be expected for a real compounded composite, analytical models cannot be used to accurately estimate the material effective permittivity; it should be noted that in this case, it can still be measured experimentally.

Numerical methods have been developed and calculation capabilities expanded to evaluate the effective dielectric permittivity of composite materials. Numerical simulations have in fact grown to represent another method for dealing with a large proportion of the physical problem of composite materials.

In this paper, the effective permittivity of a polyethylene-based nanocomposite has been calculated by numerical simulation using the Comsol Multiphysics software, which is based on the finite element method (FEM). The influence of dispersion as well as the variation of the permittivity and radius (or the volume fraction) of inclusion on effective permittivity is studied. The electric field and polarization distribution in the nanocomposite materials are also reported in this paper. A comparison between the numerical results and analytical models is presented.

6.2 Analysis

The effective dielectric permittivity of a multi-phase material can be estimated either by analytical or numerical methods.

6.2.1 Analytical models

The starting point of the most common analytical approaches used for estimating the effective properties of heterogeneous media is the solution of the single inclusion problem for which a constant field E_o along the z-direction is applied at a distance from the inclusion. This approach has been detailed in many textbooks and review papers (Banhegyi, 1986; Barber et al., 2009a; Blanchard et al., 2007; Cret et Cret, 2004; Fărcaş et al., 2010; Karkkainen, Sihvola et Nikoskinen, 2000; Koledintseva et al., 2009; Peng et al., 2009; Sihvola et Kong, 1988b; Torquato, 2002; Tuncer, Serdyuk et Gubanski, 2002). In spherical coordinates, the solution of the Laplace equation for a spherical inclusion of radius R is given by:

$$\Psi(r,\theta) = -E_o r cos\theta - AE_o \frac{cos^2\theta}{r^2} \qquad r \geq R \tag{6.1}$$

$$\Psi(r,\theta) = -E_o r cos\theta + BE_o r cos\theta \qquad r \leq R$$

with

$$A = -R^3 \frac{\varepsilon_2 - \varepsilon_1}{\varepsilon_2 + 2\varepsilon_1}$$

$$B = \frac{\varepsilon_2 - \varepsilon_1}{\varepsilon_2 + 2\varepsilon_1}$$

and where Ψ(r,θ) is the electrical potential, r is the radial coordinate, θ is the angle between the position vector and the z-coordinate, and ε_1 and ε_2 are the permittivities of the inclusion and the matrix, respectively. It should be noted that the same equations hold in a steady-state AC condition for which the potential would be a phasor, and the permittivity could be complex values, including a possible conductivity term. The electrical field along the z-direction inside the inclusion according to (6.1) is given by:

$$E_2 = \left(1 + \frac{1}{3}\frac{\varepsilon_2 - \varepsilon_1}{\varepsilon_1}\right)^{-1} E_o \tag{6.2}$$

A similar calculation can be made for the more general case of an ellipsoidal inclusion leading to

$$E_2 = \left(1 + A_1 \frac{\varepsilon_2 - \varepsilon_1}{\varepsilon_1}\right)^{-1} E_o \tag{6.3}$$

where A_1 is the depolarization factor along the ellipsoid principal axis parallel to the electrical field (Banhegyi, 1986). For spherical particles, $A_1 = A_2 = A_3 = 1/3$ and (6.3) is identical to (6.2). By definition, the effective dielectric constant of a two-component heterogeneous linear material can be defined by (Beran, 1968):

$$\varepsilon_c = \frac{q_1 \varepsilon_1 \langle E_1 \rangle + q_2 \varepsilon_2 \langle E_2 \rangle}{\langle E \rangle} \tag{6.4}$$

where ε_c is the effective permittivity, q_1 and q_2 are the volume fraction of the matrix and the inclusion, and the brackets denote an average over phase 1, phase 2, or over the material's volume. An analytical calculation of the electrical field in a composite material can only be

done if the minority phase is present in a small concentration and for regular shape inclusions. A number of results can be found in which an exact solution for several matrix systems with periodic arrangements of regular inclusions is obtained (Emets, 1998; Tuncer, Gubanski et Nettelblad, 2001). In the case of a dilute suspension of ellipsoidal shape inclusions with a permittivity ε_2 in a continuum matrix of permittivityε_1, it is possible to use the solution of the single-inclusion problem (equation (6.3)), assuming that the field E_o is equivalent to the average field in the matrix (phase 1). It leads to (Banhegyi, 1986):

$$\varepsilon_c = \varepsilon_1 \frac{\varepsilon_1(1-q_2)(1-A_1)+ \varepsilon_2[q_2+A_1(1-q_2)]}{\varepsilon_1+A_1(1-q_2)(\varepsilon_2-\varepsilon_1)} \tag{6.5}$$

A similar procedure, in case of randomly oriented inclusions leads to:

$$\varepsilon_c = \frac{\varepsilon_1(1-q_2)+\frac{\varepsilon_2 q_2}{3}\sum_{i=1}^{3}\frac{\varepsilon_1}{\varepsilon_1+(\varepsilon_2-\varepsilon_1)A_i}}{1-q_2+\frac{q_2}{3}\sum_{i=1}^{3}\frac{\varepsilon_1}{\varepsilon_1+(\varepsilon_2-\varepsilon_1)A_i}} \tag{6.6}$$

where A_i is depolarization factor for the ith axis of the ellipsoid. For spherical particles, $A_1 = A_2 = A_3 = 1/3$. In the case of spheroids for which two axes are equal ($a = b \neq c$), the analytical expressions for A_i for oblate spheroids (disk-like spheroids with $a = b > c$) and prolate spheroids (needle-like spheroids with $a = b < c$) can be found in the literature (Torquato, 2002).

Another approach, the effective medium approximation, also relies on the solution of the single-inclusion boundary value problem. The generalization of the Maxwell approximation for ellipsoidal inclusion leads to:

$$\sum_{j=1}^{2} q_j(\varepsilon_c - \varepsilon_j)\left[1 + A\frac{\varepsilon_j-\varepsilon_i}{\varepsilon_j}\right]^{-1} = 0 \tag{6.7}$$

Rapport-gratuit.com
LE NUMERO 1 MONDIAL DU MÉMOIRES

for a two-phase composite consisting of a perfectly oriented ellipsoidal inclusion (phase 2) inside a matrix (phase 1). It can be shown that this equation is equivalent to equation (6.5), and the randomly oriented case would be equivalent to (6.6). This is also the exact solution of the coated-spheres model (Hashin et Shtrikman, 1962).

A different approach in the effective medium approximation family is the self-consistent approximation, which was originally developed by Bruggeman (Bergman, 1982). It leads to a slight modification of (6.7):

$$\sum_{j=1}^{2} q_j\left(\varepsilon_c - \varepsilon_j\right)\left[1 + A\frac{\varepsilon_j - \varepsilon_c}{\varepsilon_c}\right]^{-1} = 0 \tag{6.8}$$

which in turn leads to a quadratic equation for the effective permittivity. For the case of the randomly oriented ellipsoidal, equation (6.8) can be written (Lal et Parshad, 1973) as:

$$\sum_{k=1}^{3} \frac{q_1(\varepsilon_1 - \varepsilon_c)}{A_k(\varepsilon_1 - \varepsilon_c) + \varepsilon_c} + \frac{q_2(\varepsilon_2 - \varepsilon_c)}{A_k(\varepsilon_2 - \varepsilon_c) + \varepsilon_c} = 0 \tag{6.9}$$

Finally, using a symmetric integration technique (Looyenga, 1965), it was shown that the Looyenga equation for randomly oriented ellipsoids, independently of their shape, is given by:

$$\varepsilon_c{}^{1/3} = q_1\varepsilon_1{}^{1/3} + q_2\varepsilon_2{}^{1/3} \tag{6.10}$$

As mentioned previously, all the above equations also hold in steady-state AC conditions. In this case, the electric fields can be replaced by their respective phasors and the permittivity can be replaced by their complex representation. Accordingly, equations (6.5) to (6.10) can also be used to predict a composite dielectric response, i.e., the variation of the effective complex permittivity as a function of frequency, by replacing ε_1 and ε_2 by their frequency-dependent complex representations.

6.2.2 Numerical Methods

The effective permittivity of the dielectric mixture can be calculated once the electrical field vector is known inside the material. In a purely electrostatic case, it can be calculated by solving the Poisson's equation given by:

$$\nabla.(\varepsilon_r \varepsilon_0 \nabla \Psi) = -\rho \tag{6.11}$$

where $\varepsilon_r, \varepsilon_0$ and Ψ are the relative permittivity, the vacuum permittivity and the electrical potential, respectively, and ρ is the charge density. For the neutral condition ($\rho = 0$), and if we take into account a possible conductivity σ and dielectric losses, then (6.11) can be written in the steady state more generally as (Brosseau et Beroual, 2001; Tuncer, Nettelblad et Gubañski, 2002; Tuncer, Serdyuk et Gubanski, 2001):

$$\vec{\nabla} \cdot \left[j\omega \left(\hat{\varepsilon}_r \varepsilon_0 \vec{\nabla} \hat{\Psi} \right) \right] = 0 \tag{6.12}$$

where the complex permittivity is given by:

$$\hat{\varepsilon}_r = \varepsilon' - j\left(\varepsilon'' + \frac{\sigma}{\omega \varepsilon_o}\right) \tag{6.13}$$

Once the material microstructure and the properties of each phase are known, (6.11) or (6.12) can be numerically solved by the finite elements method (FEM) using a commercially available package, such as COMSOL Multiphysics. After the field distribution is numerically evaluated, the effective permittivity of the dielectric mixture can be calculated in several ways (Brosseau et Beroual, 2001; Cret et al., 2011; Fa et al., 2010; Jebbor et Bri, 2012; Karkkainen, Sihvola et Nikoskinen, 2001; Nilsson, Gedde et Hedenqvist, 2011; Sihvola et Kong, 1988a; Tuncer, Gubański et Nettelblad, 2001; Venkatesulu et al., 2013). In this paper, the effective dielectric permittivity of the composites was calculated by using the averages of

the electric field and dielectric displacement values. Therefore, the effective dielectric permittivity can be expressed as follows:

$$\varepsilon_c = \frac{\langle D \rangle}{\langle E \rangle \varepsilon_0}$$

(6.14)

where $\langle D \rangle$ denotes the mean value of the electric displacement field and $\langle E \rangle$ is the mean value of the electric field over the material. Both averages were taken in the direction of the applied field.

6.3 Results and discussion

6.3.1 Simulation Setup

The morphology of polyethylene/clay nanocomposite in the nanometric scale observed by scanning electronic microscope (SEM) is shown in Figure 6.1. As can be seen, two components are presented in the nanocomposite. This two-phase nanocomposite consists of 5 wt % of nanoclay particles dispersed in a polyethylene matrix. A comparison between the morphology of polyethylene with 5 wt % nanoclay, PE/O-MMT (Figure 6.1(a)), and polyethylene with 5 wt % nanoclay and 10 wt % of compatibilizer, PE/O-MMT/PE-MA (Figure 6.1(b)),)), shows that the density and size of aggregates were decreased in the compatibilized nanocomposite. This improvement in the nanoclay dispersion is due to the presence of the polar compatibilizer, PE-MA (Zazoum, David et Ngô, 2013). In this paper, the dielectric permittivity of the polyethylene matrix and that of the nanoclay reinforcing fillers were taken as follows $\varepsilon_1 = 2.3$ and $\varepsilon_2 = 4.4$, for the matrix and the filler, respectively. A single-inclusion 3-D model cell was used as a first approach, as shown in Figure 6.2. The inclusion was assumed to have a spherical shape, and the particle radius was calculated in order to meet the requirement of a 5 % volume fraction of the particles. The bottom face of

the cube was set to a constant potential (Ψ = 1V), and the opposite face was set to ground (Ψ = 0). The other faces of the cube were set to periodic conditions.

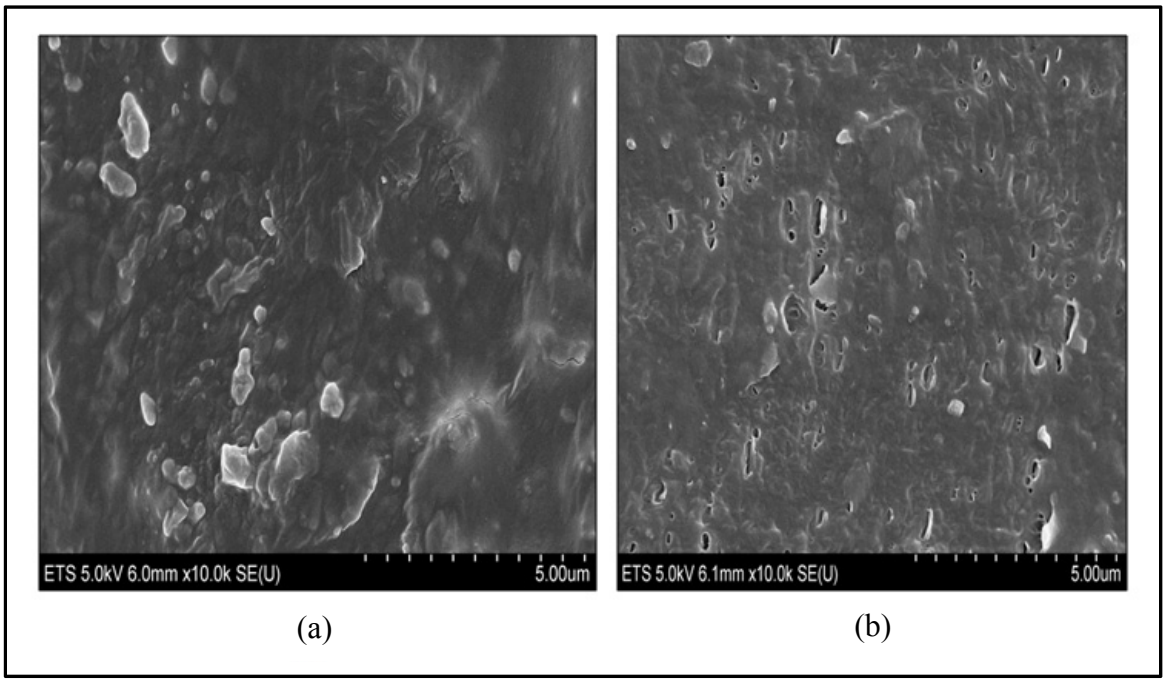

Figure 6.1 SEM micrograph of (a) PE/O-MMT and (b) PE/O-MMT/PE-MA nanocomposites

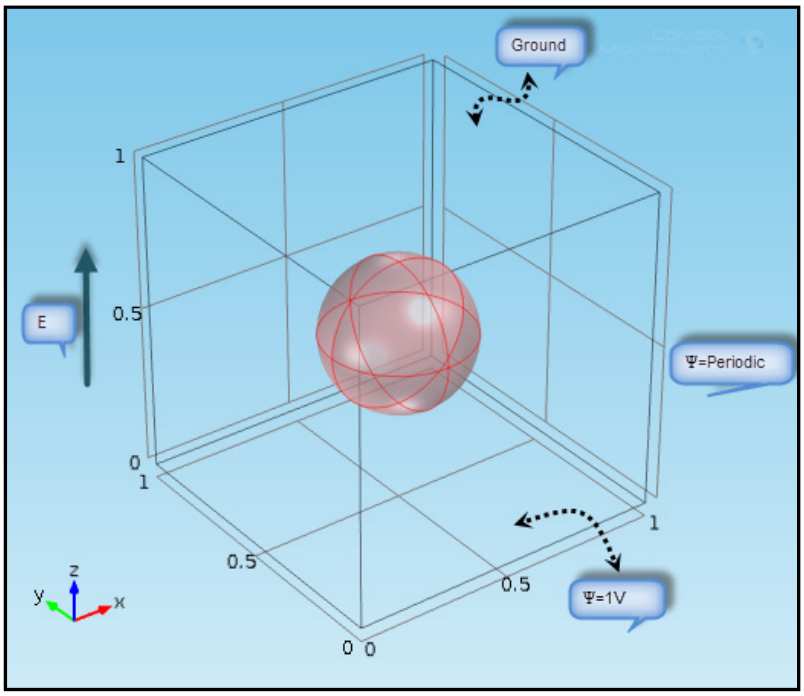

Figure 6.2 Unit cell model of a single-inclusion two-component periodic composite material

6.3.2 Ordered distribution

In order to study the effect of the dispersion of nanoclay particles on dielectric properties, such as electric field distributions and effective permittivity, four geometries (with the same volume fraction q = 0.05) were drawn with 1, 8, 27 and 64 spheres, respectively, corresponding to particle normalized radii of 0.229, 0.114, 0.076 and 0.057 (Figures 6.3 (a)-6.3 (d)).

The surface plots of the electric field distribution in the 3-D model were obtained by FEM simulations, and are shown in Figure 6.3. As can be predicted by the single-inclusion solution, a field enhancement is present at the interface between the particle and the matrix on the bottom and the top sides in the z-direction, and the field is almost constant and smaller within the inclusion. The maximum value of the electric field E_{max} increases as the degree of dispersion of the nanoclay particles increases, and the highest value is obtained when the number of spheres is 27.

The polarization vector (in C/m^2) distributions for all 4 geometries are shown in Figure 6.4, along with an enhancement at the matrix-particle interfaces in the z-direction. The highest value of polarization was found at the surface of the particles in the cell with 64 spheres. It is evident from the images that the polarization increases as the degree of dispersion of the nanoclay particles increases.

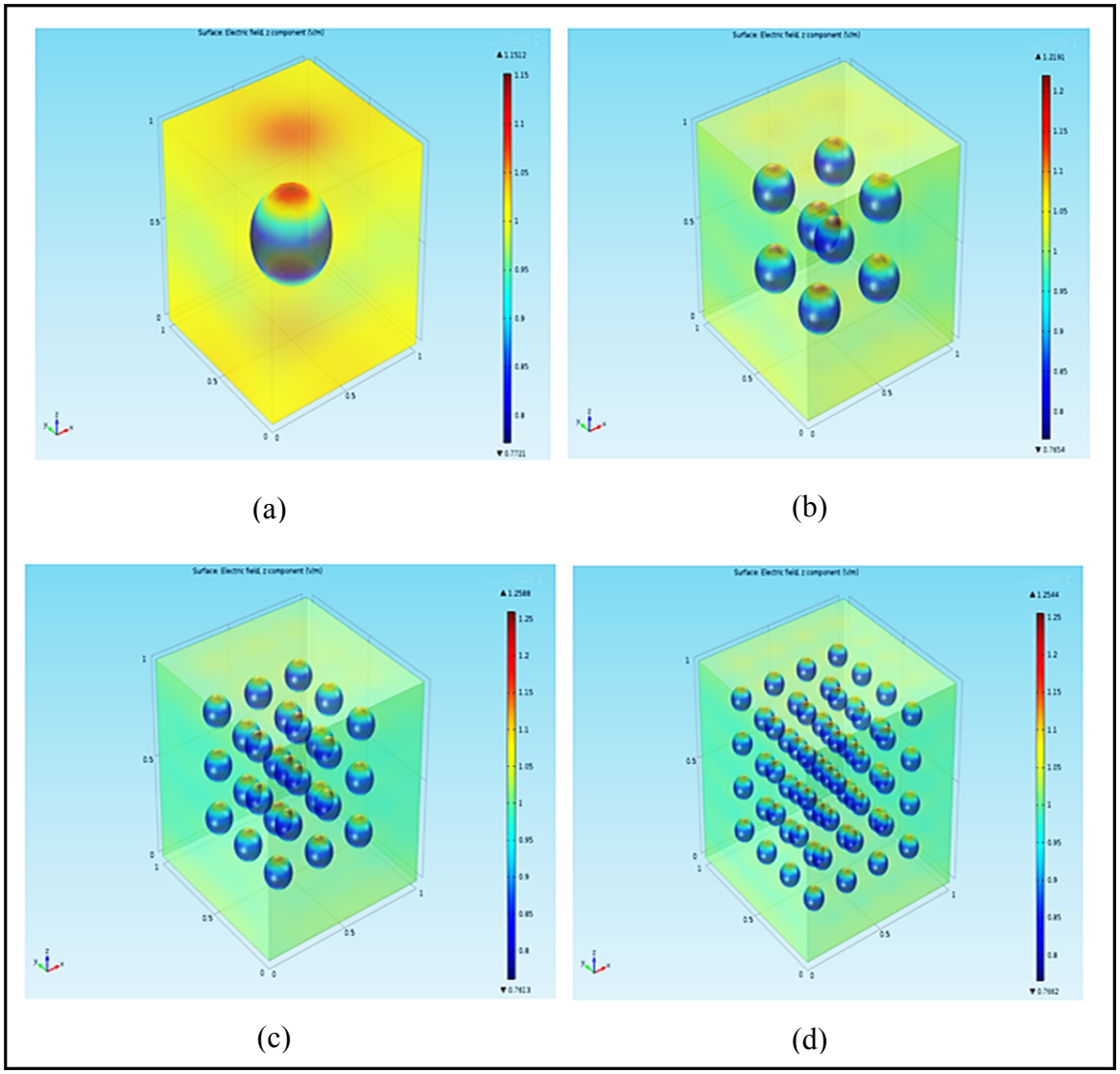

Figure 6.3 Electric field distribution in the nanocomposite with (a) 1 particle, (b) 8 particles, (c) 27 particles and (d) 64 particles, respectively (ordered distribution)

.

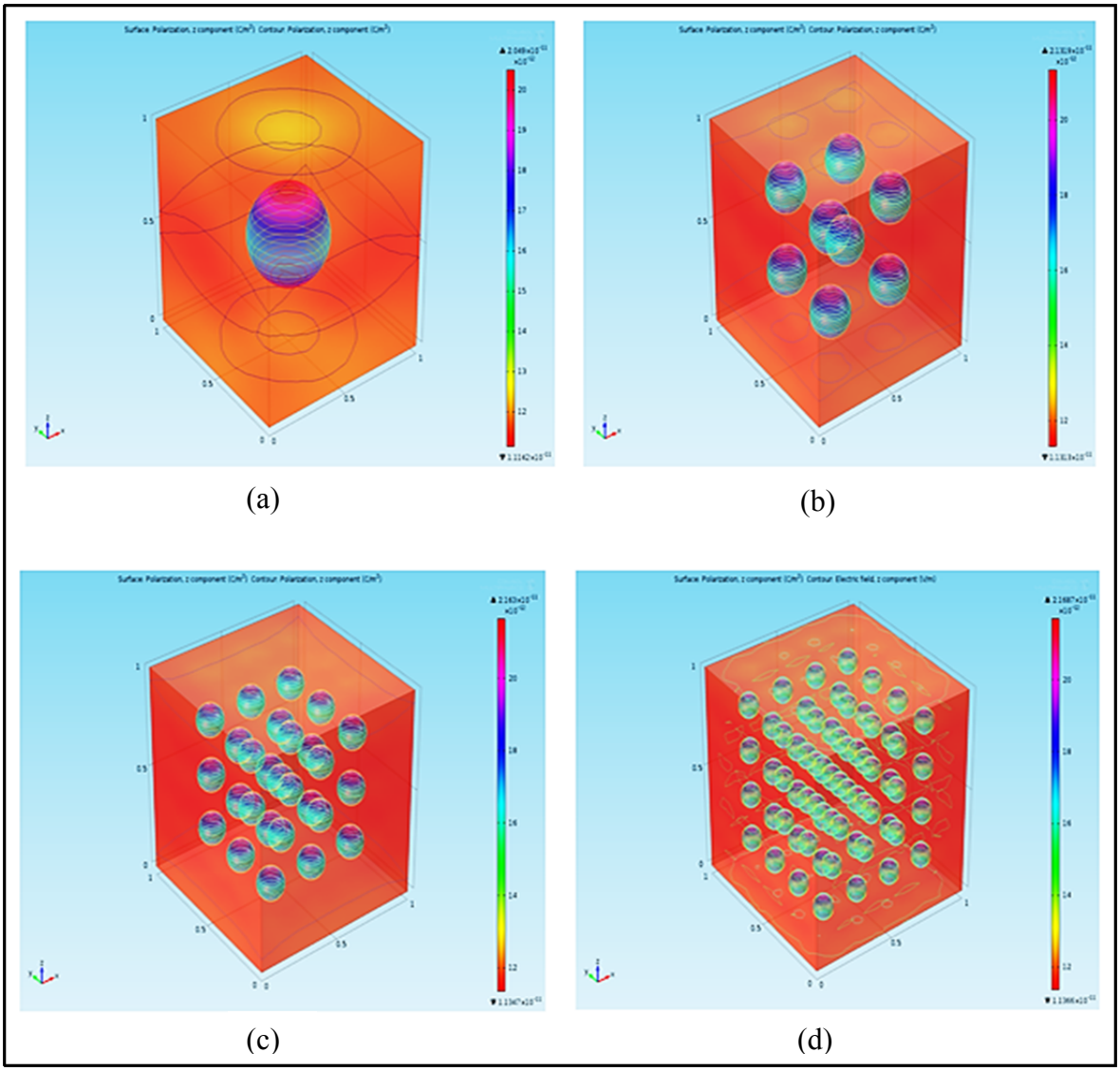

Figure 6.4 Polarization field distribution in the nanocomposites with (a) 1 particle, (b) 8 particles, (c) 27 particles and (d) 64 particles, respectively (ordered distribution)

6.3.3 Random Distribution

In the above section, the uniform reinforcing particles are considered to be orderly dispersed in a polyethylene matrix. In real materials, nanoclay particles or any reinforcing filler are distributed more or less randomly in the polymer matrix with agglomerate size distributions. Figures 6.5 (a)-6.5 (d) show four geometries and electric field distribution plots for different numbers of randomized nanoclay particles. The volume fraction of nanoclay particles was set at 5 % and dispersed in a unit cell. The corresponding effective permittivity and normalized maximum electric field E_{max}/E_0 (where E_0 = 1kV/mm) of the nanocomposite materials are plotted in Figures 6.6 and 6.7, respectively. As can be seen from Figure 6.6, the effective permittivity for both distributions does not vary significantly with the number of particles. On the other hand, the effective permittivity of the random distribution was found to be higher than that of ordered distributions. Figure 6.7 shows the normalized maximum value of the electrical field in the z-direction as a function of the particle dispersion. At a low particle number, it can be seen that the normalized maximum electric field is almost identical for the ordered distribution as for the random cases, and increases as the quality of dispersion is improved. For particle numbers higher than 27, the normalized maximum value of the electrical field in the random distribution decreases slightly as the quality of dispersion increases, while in the ordered distribution, the electric field is found to increase considerably with an increase in the number of particles.

Rapport-Gratuit.com

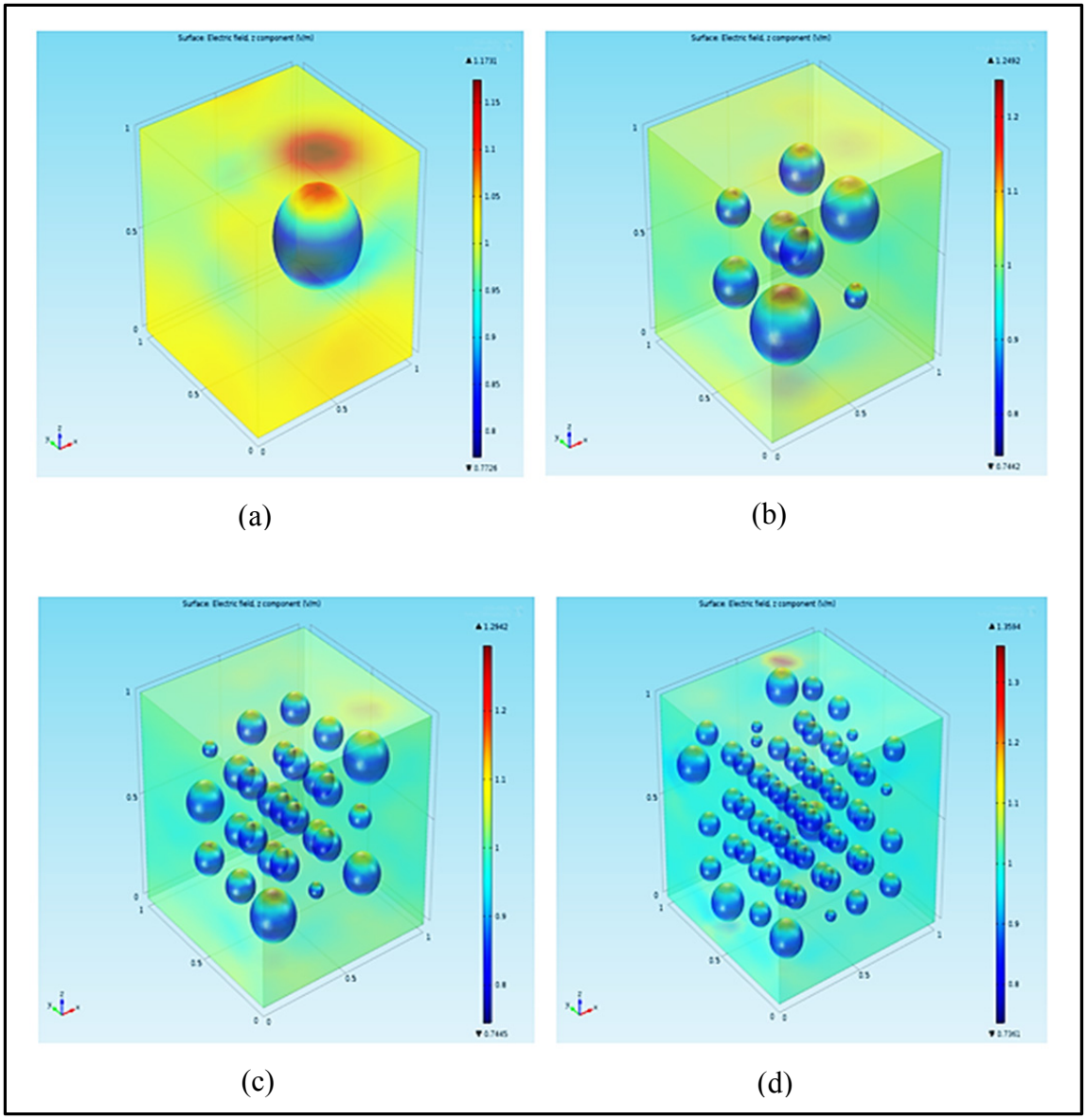

Figure 6.5 Electric field distribution in the nanocomposites with
(a) 1 particle, (b) 8 particles, (c) 27 particles and (d) 64 particles, respectively
(random distribution)

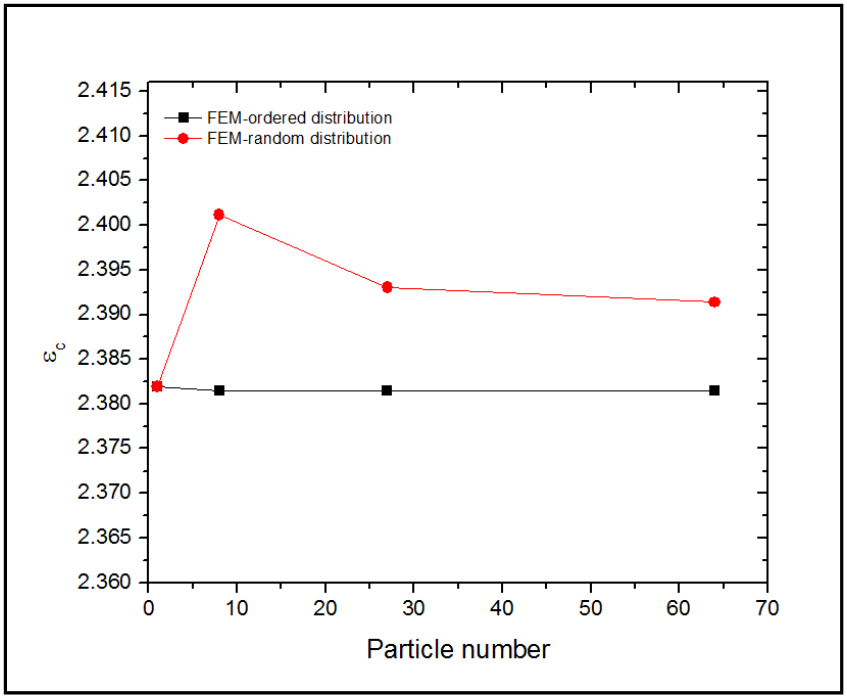

Figure 6.6 Comparison of effective permittivity for random and ordered nanoparticle distributions

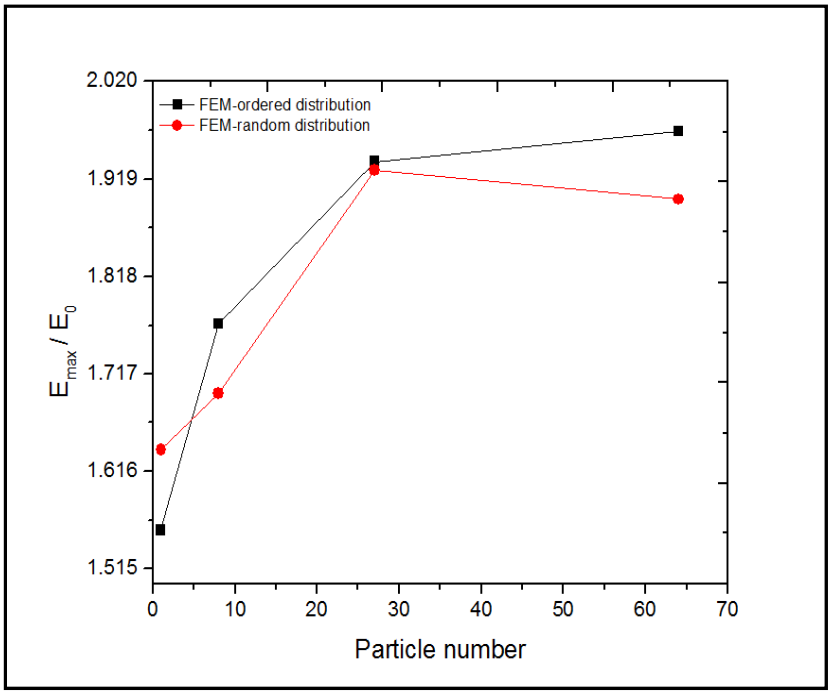

Figure 6.7 Comparison of normalized maximum electric field for random and ordered nanoparticle distributions

Rapport-gratuit.com
LE NUMERO 1 MONDIAL DU MÉMOIRES

6.3.4 Effect of the Permittivity of the Inclusion on Effective Permittivity

In this section, the two geometries of 64 spheres of the ordered and random distributions presenting the distribution of the electrical potential simulated by FEM are shown in Figures 6.8 (a) and 6.8 (b) to study the effect of a variation of the dielectric permittivity of inclusion on the effective permittivity of the ordered and random nanocomposites. The resulting effective permittivities obtained from FEM are compared with those calculated from equation (6.7), the Maxwell-Garnett model, equation (6.9), the Bruggeman model, and equation (6.10), the Looyenga model. The dielectric permittivity of the polyethylene matrix ε_1 was assumed to be 2.3, while that of the inclusion ε_2 was varied from 2 to 30. The effective permittivity ε_c as a function of ε_2 is plotted in Figure 6.9. At values of ε_2 less than 5, the effective permittivity of the ordered and random composites and that of analytical equations were very close to one another. When ε_2 was greater than 5, the effective permittivity of the ordered distribution was identical to that of the Maxwell-Garnett model, while the effective permittivity of the random distribution was closer to that of the Bruggeman symmetrical model.

Figure 6.10 shows the effect of varying the permittivity of the inclusion ε_2 on the normalized maximum value of electrical field in the z-direction. As expected, for ordered and random distributions, the maximum value of the electrical field increases as the value ε_2 increases.

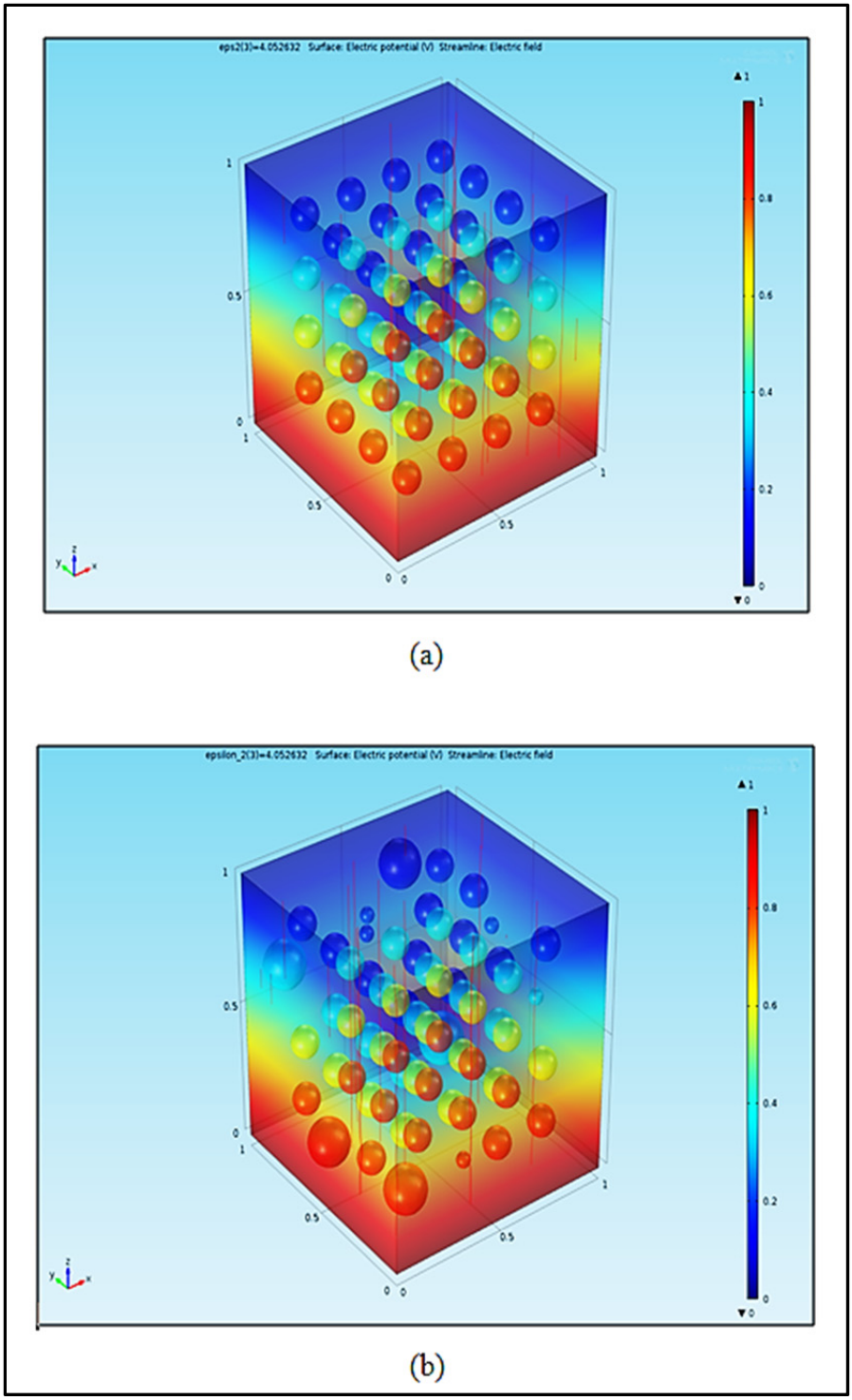

Figure 6.8 Electric potential distribution in the nanocomposite with 64 particles: (a) ordered distribution and (b) random distribution. The red lines present the electrical field stream lines

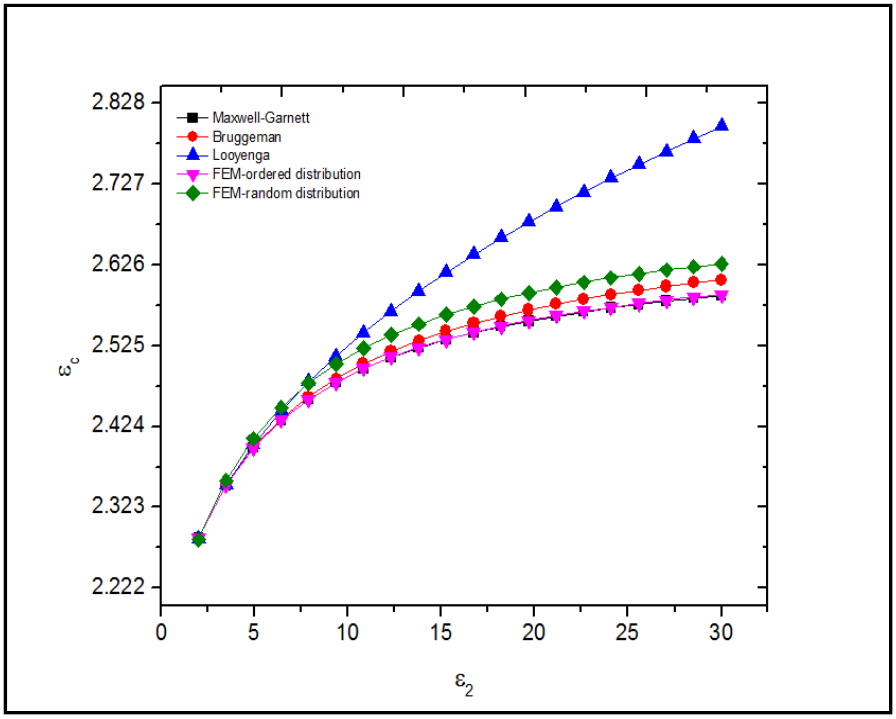

Figure 6.9 Numerical and theoretical results of the effective permittivity as a function of the dielectric permittivity of inclusion

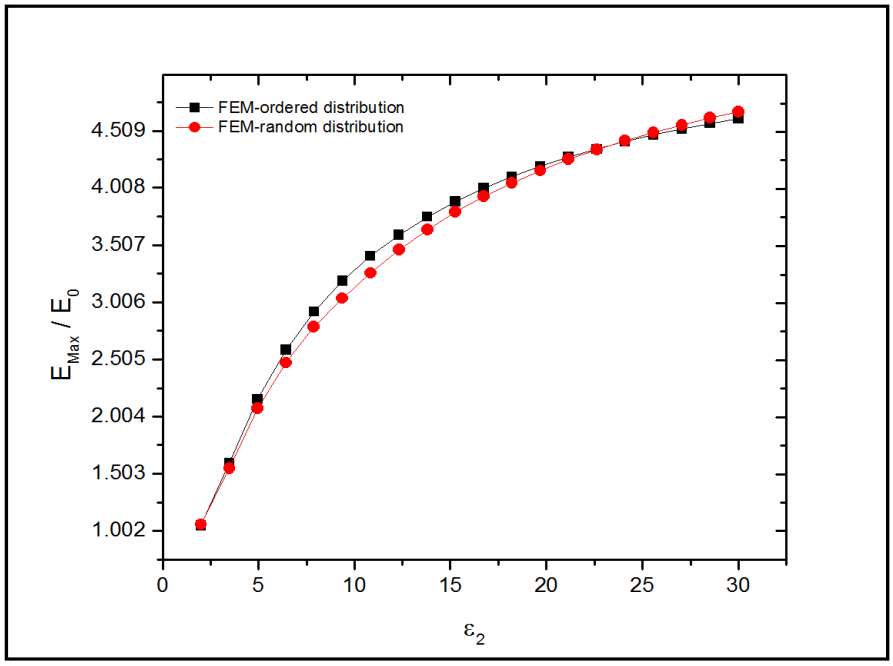

Figure 6.10 Normalized maximum electric field for ordered and random nanoparticle distributions as a function of the dielectric permittivity of inclusion

6.3.5 Effect of the Radius (and Volume Fraction) of the Inclusion on Effective Permittivity

The two geometries for the single-inclusion case of the ordered and random distributions presenting the distribution of the electric potential simulated by FEM are shown in Figure 6.11. In the simulation, the permittivity of the polymer matrix ε_1 is still assumed to be 2.3, and the permittivity of the inclusion ε_2 is set at 4.4. To study the effect of nanoclay loading on the effective permittivity ε_c, the normalized radius of the inclusion r/r_0 (where $r_0 = 1\mu m$) was varied from 0.010 to 0.400, corresponding to the volume fraction of nanoparticles ranging from 0.0004 % to 26.81 %.

The effective permittivity of the nanocomposites as a function of the radius of nanoclay particles is plotted in Figure 6.12. It can be observed that the effective permittivity increases with the nanoclay particle radius, and it is evident from this figure that the effective permittivity of the ordered and random distributions obtained from FEM is quite similar to that calculated with the Maxwell-Garnett model, and is also very close to those of the Bruggeman and Looyenga models. These results confirm the validity of our simulation method.

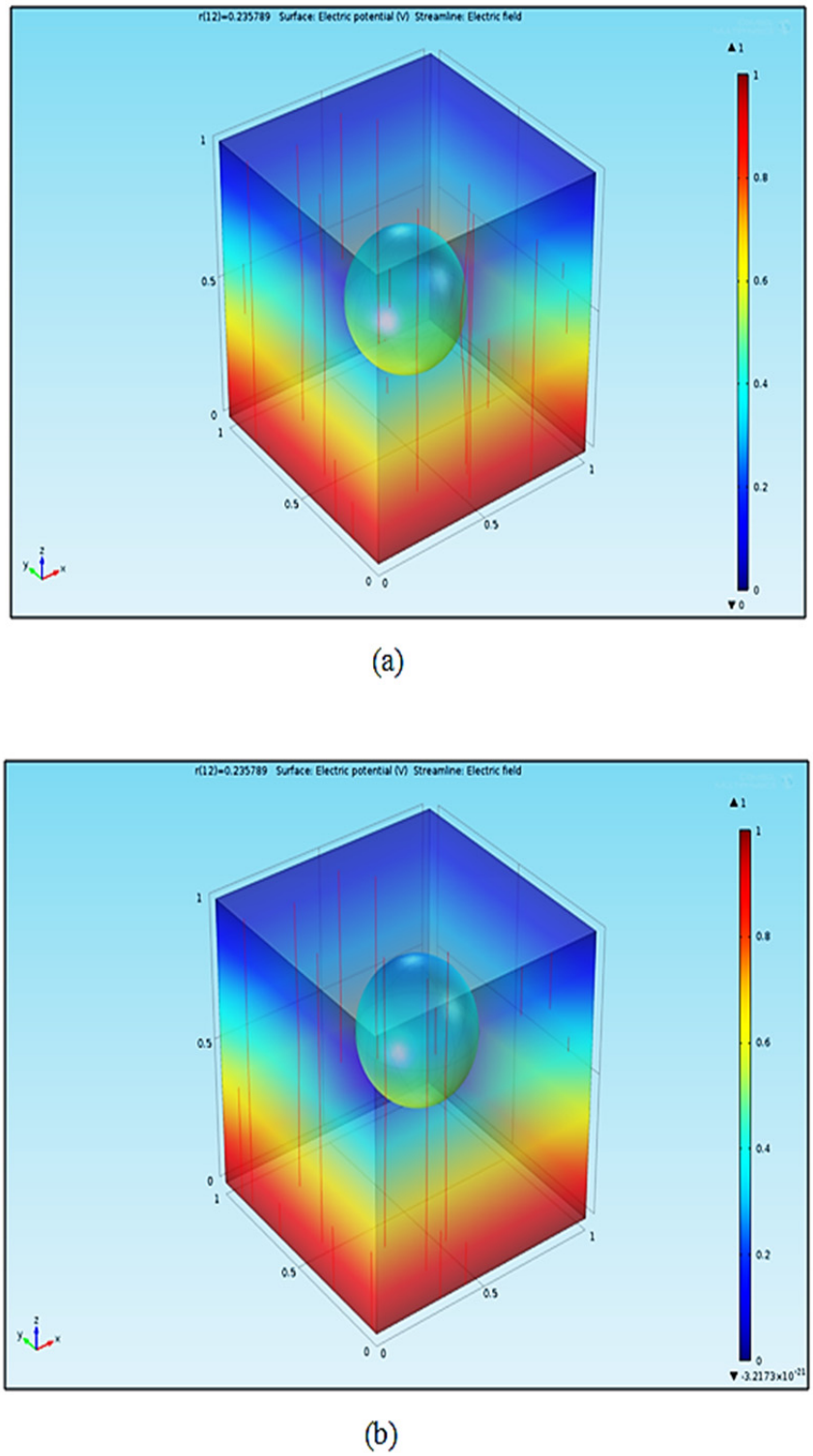

Figure 6.11 Electric potential distribution in the nanocomposite with 1 particle: (a) ordered distribution and (b) random distribution. The red lines present the electrical field stream lines

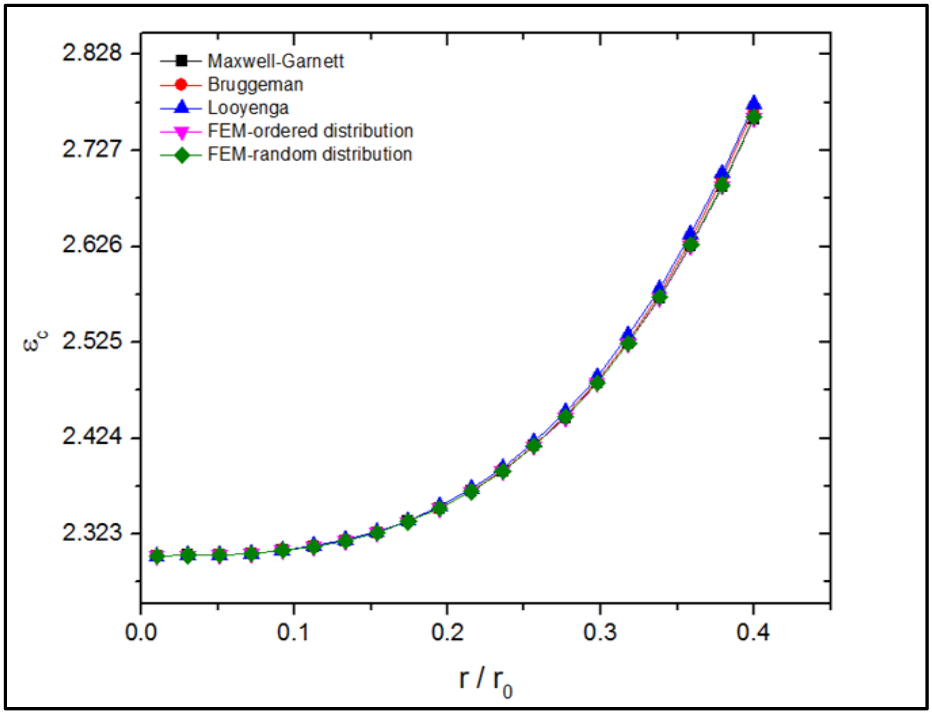

Figure 6.12 Variation of the effective permittivity with normalized radius of the spherical nanoclay particles

6.4 Conclusion

A 3-D simulation model using the finite elements method was developed in order to study the effective permittivity and electric field distribution of polyethylene/clay nanocomposite materials for electrical applications. An enhancement of the electric field and polarization was observed as the degree of dispersion of the nanoclay particles increased; however, the effective permittivity of the nanocomposites was not affected by improving the quality of dispersion of nanoclay particles in the host matrix. The numerical results indicate that the Maxwell-Garnett model is appropriate for evaluating the effective permittivity of ordered distribution, while the Bruggeman Symmetry model remains the most suitable for calculating the effective permittivity for the random distribution. Finally, this numerical model can be extended to design nanocomposite materials with optimum dielectric properties for electrotechnical or electronic applications.

Acknowledgment

The authors are grateful for financial support from the National Sciences and Engineering Research Council of Canada (NSERC).

Conflict of Interests

The authors declare that there is no conflict of interests regarding the publication of this paper.

CONCLUSION GÉNÉRALE

Ce travail de thèse a pour objectifs, d'abord, de contribuer à optimiser le procédé de fabrication des nanocomposites (les paramètres opératoires et la formulation chimique). Ensuite, d'analyser l'influence de la microstructure des nanocomposites sur leurs propriétés diélectriques. Cela permettrait d'évaluer l'apport que peuvent présenter ce type de matériaux dans l'industrie des isolants électriques, et très particulièrement les câbles de puissance.

La première partie de ce travail a été consacrée à l'étude bibliographique concernant l'argile utilisée, le polymère et les systèmes polymère/nanoargile. Différentes techniques sont envisagées pour atteindre les objectifs de ce travail de recherche. On peut citer, à ce propos, l'observation microscopique (MEB, MET, MOP et MFA), la diffraction des rayons X, les mesures dynamiques mécaniques, les analyses thermiques. La combinaison de ces techniques a permis de caractériser l'état de dispersion, et par la suite d'étudier les propriétés diélectriques des nanocomposites PE/O-MMT et PE/O-MMT/PE-MA.

Dans la partie expérimentale, le matériau nanocomposite PE/O-MMT a été préparé avec et sans compatibilisant par la technique du mélange à l'état fondu en utilisant l'extrudeuse à double vis co-rotatives.

Les mesures de diffraction des rayons X ont montré que l'état de dispersion dépend des paramètres opératoires utilisés lors de la fabrication, et que l'ajout du compatibilisant au mélange binaire PE/O-MMT conduit à une structure partiellement exfoliée. Ces résultats ont été confirmés par les observations microscopiques.

Les caractérisations thermiques, par DSC des systèmes PE/O-MMT et PE/O-MMT/PE-MA, ont révélé que l'introduction des nanoargiles au sein de la matrice polymère n'a pas modifié la morphologie du polymère; le taux de cristallinité n'ayant pas été changé. Toutefois, les mesures effectuées par TGA ont montré que l'ajout des nanoargiles conduit à une amélioration de la résistance aux dégradations thermiques. En outre, les résultats obtenus par

Rapport-Gratuit.com

les mesures de DMTA ont révélé qu'une structure partialement exfoliée des nanocomposites améliore les propriétés thermomécaniques.

Ce travail a apporté une contribution importante au niveau de la corrélation structure-propriétés diélectriques. Les études de l'effet de la structure des nanocomposites sur la réponse diélectrique (article #1) ont mis en évidence l'existence de deux pics de relaxation dans les systèmes PE/O-MMT et PE/O-MMT/PE-MA. La première relaxation est interfaciale de type Maxwell-Wagner, tandis que la deuxième est une relaxation dite dipolaire. Une relation entre la structure des nanocomposites et le taux de relaxation a été observée. Les résultats de l'article #2 et #3 révèlent que le claquage diélectrique est très sensible à la structure finale des nanocomposites. Une amélioration au niveau de la qualité de dispersion entraine une augmentation de la rigidité diélectrique.

Dans la dernière partie de cette thèse (article#4) un modèle de simulation, utilisant la méthode des éléments finis, a été mis en place pour étudier l'effet de la qualité de dispersion sur la permittivité effective des nanocomposites. Les résultats obtenus ont permis de comprendre la corrélation entre la structure et les propriétés diélectriques du système PE/argile nanocomposites.

Le degré de dispersion des nanoargiles dans le système PE/O-MMT/PE-MA reste supérieur à celui obtenu dans le PE/O-MMT. Les résultats obtenus sont limités à une structure intercalée/exfoliée. Pour parvenir à une dispersion exfoliée, une concentration suffisante en PE-MA est nécessaire.

La caractérisation de l'état de dispersion dans le domaine des nanocomposites polymère/nanoargile, par des méthodes microscopiques, est considérée comme un grand défi. Comme il a été montré dans ce travail, le comportement diélectrique est très sensible à la structure des matériaux nanocomposites, il est donc intéressant d'approfondir les études sur ce sujet pour arriver à utiliser des méthodes de caractérisation macroscopique, comme la

réponse diélectrique et le claquage, pour évaluer l'état de dispersion des nanoargiles au sein d'une matrice polymère.

Rapport-gratuit.com
LE NUMERO 1 MONDIAL DU MÉMOIRES

RECOMMANDATIONS

Dans ce qui suit, nous présentons quelques perspectives et pistes de recherches, qui pourraient être menées à la lumière des résultats émanant de ce travail de thèse:

- Il pourrait être intéressant de développer d'autres techniques de mise en forme qui permettent d'orienter les nanoargiles, et étudier l'effet d'orientation des feuillets argileux sur les propriétés des nanocomposites.
- Il est intéressant, également, de tester d'autres types d'argiles, et d'étudier l'influence du traitement de surface des nanoargile sur la structure et les propriétés diélectriques des nanocomposites.
- Essayer d'autres types de compatibilisant tels le PP-g-MA, et étudier l'effet du choix de l'agent couplant sur le degré de dispersion, et par la suite sur les propriétés diélectriques.
- Pour compléter cette étude, il est intéressant d'effectuer des mesures de charges d'espace et de la résistance aux décharges partielles dans les nanocomposites polyéthylène/argile, afin de comprendre les mécanismes impliqués dans l'accumulation de ces charges.
- Finalement, dans l'article #4 nous avons élaboré un modèle de simulation qui décrit l'état de dispersion des nanoargiles. Toutefois, il ne représente qu'une étape intermédiaire et requiert un développement qui tiendrait en compte de l'effet de l'interface dans le domaine fréquentiel, afin de comparer les résultats numériques et expérimentaux.

ANNEXE I

PUBLICATIONS

ARTICLES DE REVUE:

1. Zazoum, B, E David et AD Ngô. 2014. « Correlation between Structure and Dielectric Breakdown in LDPE/HDPE/Clay Nanocomposites ». ISRN Nanomaterials, vol. 2014.
2. Zazoum, B, E David et AD Ngô. 2013. « LDPE/HDPE/Clay Nanocomposites: Effects of Compatibilizer on the Structure and Dielectric Response ». Journal of Nanotechnology, vol. 2013.
3. David, E, M Fréchette, B Zazoum, C Daran-Daneau, AD Ngô et H Couderc. 2013. « Dielectric properties of PE/clay nanocomposites ». Journal of Nanomaterials, vol. 2013, p. 65.
4. Zazoum, B, E David et AD Ngô. 2014. « Simulation and Modeling of Polyethylene/Clay Nanocomposite for Dielectric Application ». Accepted, Transactions on Electrical and Electronic Materials.
5. Zazoum, B, E David et AD Ngô. 2014. « Structural and Dielectric Studies of LLDPE/O-MMT Nanocomposites ». Accepted, Transactions on Electrical and Electronic Materials.

ARTICLES DE CONFÉRENCES:

1. Zazoum, B, E David et AD Ngô. 2013. « Dynamic Mechanical Characterization of LLDPE/Clay Nanocomposite ». In Design, Manufacturing and Applications of Composites: Proceedings of the Ninth Joint Canada-Japan Workshop on Composites; Kyoto Institute of Technology, Kyoto, Japan July 2012. p. 225. DEStech Publications, Inc.

2. Zazoum, B, AD Ngô, E David, C Daneau et M Fréchette. 2011. « Morphology characteristics, thermal properties and dielectric breakdown of LLDPE/clay nanocomposites ». In Proceedings of the 26th Technical Conference of the American Society for Composites and 2nd Joint Canadian-American International Conference on Composites.
3. David, E, C Daran-Daneau, MF Fréchette, B Zazoum, AD Ngo et S Savoie. 2012. « Dielectric response of LLDPE/Clay nanocomposite melt compounded from a masterbatch ». In Electrical Insulation (ISEI), Conference Record of the 2012 IEEE International Symposium on. p. 641-645. IEEE.

LISTE DE RÉFÉRENCES BIBLIOGRAPHIQUES

Alexandre, Michael, et Philippe Dubois. 2000. « Polymer-layered silicate nanocomposites: preparation, properties and uses of a new class of materials ». *Materials Science and Engineering: R: Reports,* vol. 28, n° 1, p. 1-63.

Ambid, Matthieu. 2007. « Evaluation de nanocomposites polypropylène/silicate pour l'isolation électrique: étude des phénomènes de polarisation, de conduction et des propriétés optiques ». Université de Toulouse, Université Toulouse III-Paul Sabatier.

Artbauer, J. 1996. « Electric strength of polymers ». *Journal of Physics D: Applied Physics,* vol. 29, n° 2, p. 446.

AWAJI, H., Y. NISHIMURA, S.M. CHOI, Y. TAKAHASHI, T. GOTO et S. HASHIMOTO. 2009. « Toughening mechanism and frontal process zone size of ceramics ». *Journal of the Ceramic Society of Japan,* vol. 117, n° 1365, p. 623-629.

Banhegyi, G. 1986. « Comparison of electrical mixture rules for composites ». *Colloid and polymer science,* vol. 264, n° 12, p. 1030-1050.

Barber, Peter, Shiva Balasubramanian, Yogesh Anguchamy, Shushan Gong, Arief Wibowo, Hongsheng Gao, Harry J Ploehn et Hans-Conrad Zur Loye. 2009a. « Polymer composite and nanocomposite dielectric materials for pulse power energy storage ». *Materials,* vol. 2, n° 4, p. 1697-1733.

Barber, Peter, Shiva Balasubramanian, Yogesh Anguchamy, Shushan Gong, Arief Wibowo, Hongsheng Gao, Harry Ploehn et Hans-Conrad Zur Loye. 2009b. « Polymer Composite and Nanocomposite Dielectric Materials for Pulse Power Energy Storage ». *Materials,* vol. 2, n° 4, p. 1697-1733.

Beran, MJ. 1968. « Statistical Continuum Theories, Interscience Publ ». *N. York.*

Bergman, David J. 1982. « Rigorous bounds for the complex dielectric constant of a two-component composite ». *Annals of Physics,* vol. 138, n° 1, p. 78-114.

Blanchard, Cédric, Jorge A Portí, Juan A Morente, Alfonso Salinas et Enrique A Navarro. 2007. « Determination of the effective permittivity of dielectric mixtures with the transmission line matrix method ». *Journal of Applied Physics,* vol. 102, n° 6, p. 064101-064101-9.

Böhning, M., H. Goering, A. Fritz, K.W. Brzezinka, G. Turky, A. Schönhals et B. Schartel. 2005. « Dielectric study of molecular mobility in poly (propylene-graft-maleic anhydride)/clay nanocomposites ». *Macromolecules,* vol. 38, n° 7, p. 2764-2774.

Brosseau, C, et A Beroual. 2001. « Effective permittivity of composites with stratified particles ». *Journal of Physics D: Applied Physics,* vol. 34, n° 5, p. 704.

Chen, G, et AE Davies. 2000. « The influence of defects on the short-term breakdown characteristics and long-term dc performance of LDPE insulation ». *Dielectrics and Electrical Insulation, IEEE Transactions on,* vol. 7, n° 3, p. 401-407.

Chen, L., et G. Chen. 2009. « Relaxation behavior study of silicone rubber crosslinked network under static and dynamic compression by electric response ». *Polymer Composites,* vol. 30, n° 1, p. 101-106.

Chiu, Fang-Chyou, Hong-Zhi Yen et Cheng-En Lee. 2010. « Characterization of PP/HDPE blend-based nanocomposites using different maleated polyolefins as compatibilizers ». *Polymer Testing,* vol. 29, n° 3, p. 397-406.

Cret, R, et L Cret. 2004. « Numerical computation of dielectric permittivity of mixtures ». *Journal of Optoelectronics and Advanced Materials,* vol. 6, p. 1045-1048.

Cret, R., L. Darabant, C. Farcas et A. Turcu. 2011. « Considerations about the influence of some factors related to the geometric characteristics of inclusions on effective permittivity of dielectric mixtures ». In *Advanced Topics in Electrical Engineering (ATEE), 2011 7th International Symposium on*. (12-14 May 2011), p. 1-6.

David, E., M. Fréchette, B. Zazoum, C. Daran-Daneau, A. D. Ngô et H. Couderc. 2013. « Dielectric properties of PE/clay nanocomposites ». *Journal of Nanomaterials,* vol. 2013.

David, Éric. 2010. « Matériaux diélectriques : Propriétés diélectriques statiques.Coll. « Notes du cours SYS-862 Matériaux diélectriques ». Montréal: École de Technologie Supérieure.Montréal: École de Technologie Supérieure.

Davis, R.D., A.J. Bur, M. McBrearty, Y.H. Lee, J.W. Gilman et P.R. Start. 2004. « Dielectric spectroscopy during extrusion processing of polymer nanocomposites: a high throughput processing/characterization method to measure layered silicate content and exfoliation ». *Polymer,* vol. 45, n° 19, p. 6487-6493.

de Paiva, Lucilene Betega, Ana Rita Morales et Francisco R. Valenzuela Díaz. 2008. « Organoclays: Properties, preparation and applications ». *Applied Clay Science,* vol. 42, n° 1–2, p. 8-24.

Debye, Peter Josef William, Peter Joseph Wilhelm Debye et Peter Joseph Wilhelm Debye. 1929. *Polar molecules*, 172. Dover New York.

Diaham, Sombel. 2007. « Etude du comportement sous haute température de matériaux polyimides en vue de la passivation de composants de puissance à semi-conducteurs grand cap ». Université de Toulouse, Université Toulouse III-Paul Sabatier.

Douminge, Ludovic. 2010. « Etude du comportement du polyéthylène haute densité sous irradiation ultraviolette ou sollicitation mécanique par spectroscopie de fluorescence ». Université de La Rochelle.

DUBOIS, Jean-Claude. 1998. *Propriétés diélectriques des polymères*. Ed. Techniques Ingénieur.

Dumont, M. J., A. Reyna-Valencia, J. P. Emond et M. Bousmina. 2007. « Barrier properties of polypropylene/organoclay nanocomposites ». *Journal of Applied Polymer Science,* vol. 103, n° 1, p. 618-625.

Emets, Yu P. 1998. « Electrical characteristics of three-component dielectric media ». *Journal of Experimental and Theoretical Physics,* vol. 87, n° 3, p. 612-620.

Fa, x, rcas, x, C., Cret, x, R., D. Petreus, Palaghit, x, x et N. 2010. « Modeling and simulation of dielectric mixtures using finite elements method ». In *Design and Technology in Electronic Packaging (SIITME), 2010 IEEE 16th International Symposium for*. (23-26 Sept. 2010), p. 305-308.

Fărcaş, C, R Creţ, D Petreuş et N Palaghiţă. 2010. « Modeling and simulation of dielectric mixtures using finite elements method ». In *Design and Technology in Electronic Packaging (SIITME), 2010 IEEE 16th International Symposium for*. p. 305-308. IEEE.

Gao, Junguo, Ning Guo, Yali Liu, Jing Li, Haitao Hu, Liang Sun et Xiaohong Zhang. 2009. « Effect of compound technology on polyethylene/montmorillonite composites ». In *Properties and Applications of Dielectric Materials, 2009. ICPADM 2009. IEEE 9th International Conference on the*. p. 781-784. IEEE.

Gaume, Julien, Christine Taviot-Gueho, Stéphane Cros, Agnès Rivaton, Sandrine Thérias et Jean-Luc Gardette. 2012. « Optimization of PVA clay nanocomposite for ultra-barrier multilayer encapsulation of organic solar cells ». *Solar Energy Materials and Solar Cells,* vol. 99, n° 0, p. 240-249.

Gloaguen, Jean-Michel, et Jean-Marc Lefebvre. 2007. « Nanocomposites polymères/silicates en feuillets ». *Techniques de l'ingénieur. Plastiques et composites*, n° AM5205.

Green, CD, AS Vaughan, Geoffrey Robert Mitchell et T Liu. 2008. « Structure property relationships in polyethylene/montmorillonite nanodielectrics ». *Dielectrics and Electrical Insulation, IEEE Transactions on,* vol. 15, n° 1, p. 134-143.

Rapport-Gratuit.com

Green, CD, AS Vaughan, GC Stevens, SJ Sutton, T Geussens et MJ Fairhurst. 2011. « On the temperature dependence of electrical and mechanical properties of recyclable cable insulation materials based upon polyethylene blends ». In *Electrical Insulation and Dielectric Phenomena (CEIDP), 2011 Annual Report Conference on*. p. 36-39. IEEE.

Guastavino, F., G. Coletti, A. Dardano, A. Fina et A. S. Thelakkadan. 2010. « Thermo-mechanical and electrical characterization of epoxy/nanoclay composites ». In *Electrical Insulation and Dielectric Phenomena (CEIDP), 2010 Annual Report Conference on*. (17-20 Oct. 2010), p. 1-4.

Han, Y., Z. Wang, X. Li, J. Fu et Z. Cheng. 2001. « Polymer-layered Silicate Nanocomposites: Synthesis, Characterization, Properties and Applications ». *Current Trends in Polymer Science,* vol. 6, p. 1-16.

Hashin, Zvi, et Shmuel Shtrikman. 1962. « A variational approach to the theory of the effective magnetic permeability of multiphase materials ». *Journal of applied Physics,* vol. 33, n° 10, p. 3125-3131.

Havriliak, S, et S Negami. 1966. « A complex plane analysis of α-dispersions in some polymer systems ». In *Journal of Polymer Science Part C: Polymer Symposia*. Vol. 14, p. 99-117. Wiley Online Library.

Havriliak, S, et S Negami. 1967. « A complex plane representation of dielectric and mechanical relaxation processes in some polymers ». *Polymer,* vol. 8, p. 161-210.

Hong, Seok-In, et Jong-Whan Rhim. 2012. « Preparation and properties of melt-intercalated linear low density polyethylene/clay nanocomposite films prepared by blow extrusion ». *LWT - Food Science and Technology,* vol. 48, n° 1, p. 43-51.

Hosier, IL, AS Vaughan et SG Swingler. 2002. « The effects of measuring technique and sample preparation on the breakdown strength of polyethylene ». *Dielectrics and Electrical Insulation, IEEE Transactions on,* vol. 9, n° 3, p. 353-361.

Hotta, S., et DR Paul. 2004. « Nanocomposites formed from linear low density polyethylene and organoclays ». *Polymer,* vol. 45, n° 22, p. 7639-7654.

Hoyos, M., N. Garcia, R. Navarro, A. Dardano, A. Ratto, F. Guastavino et P. Tiemblo. 2008a. « Electrical strength in ramp voltage AC tests of LDPE and its nanocomposites with silica and fibrous and laminar silicates ». *Journal of Polymer Science Part B: Polymer Physics,* vol. 46, n° 13, p. 1301-1311.

Hoyos, M., N. García, R. Navarro, A. Dardano, A. Ratto, F. Guastavino et P. Tiemblo. 2008b. « Electrical strength in ramp voltage AC tests of LDPE and its nanocomposites with silica and fibrous and laminar silicates ». *Journal of Polymer Science Part B: Polymer Physics,* vol. 46, n° 13, p. 1301-1311.

Ieda, Masayuki. 1980. « Dielectric breakdown process of polymers ». *Electrical Insulation, IEEE Transactions on*, n° 3, p. 206-224.

Jebbor, Nawfal, et Seddik Bri. 2012. « Effective permittivity of periodic composite materials: Numerical modeling by the finite element method ». *Journal of Electrostatics,* vol. 70, n° 4, p. 393-399.

Job, Aldo E, Neri Alves, Maria Zanin, Marcelo M Ueki, Luiz HC Mattoso, Marcia Y Teruya et José A Giacometti. 2003. « Increasing the dielectric breakdown strength of poly (ethylene terephthalate) films using a coated polyaniline layer ». *Journal of Physics D: Applied Physics,* vol. 36, n° 12, p. 1414.

Junguo, G., Z. Jinmei, J. Quanquan, L. Jiayin, Z. Mingyan et Z. Xiaohong. 2008. « Study on brekdown and paitial discharge of polyethylene/montmorillonite nanocomposites ». In *Electrical Insulating Materials, 2008.(ISEIM 2008). International Symposium on*. p. 597-600. IEEE.

Karkkainen, Kimmo K, Ari Henrik Sihvola et Keijo I Nikoskinen. 2000. « Effective permittivity of mixtures: Numerical validation by the FDTD method ». *Geoscience and Remote Sensing, IEEE Transactions on,* vol. 38, n° 3, p. 1303-1308.

Karkkainen, Kimmo, Ari Sihvola et Keijo Nikoskinen. 2001. « Analysis of a three-dimensional dielectric mixture with finite difference method ». *Geoscience and Remote Sensing, IEEE Transactions on,* vol. 39, n° 5, p. 1013-1018.

Kato, Makoto, Arimitsu Usuki et Akane Okada. 1997. « Synthesis of polypropylene oligomer—clay intercalation compounds ». *Journal of Applied Polymer Science,* vol. 66, n° 9, p. 1781-1785.

Kawasumi, M., N. Hasegawa, M. Kato, A. Usuki et A. Okada. 1997. « Preparation and mechanical properties of polypropylene-clay hybrids ». *Macromolecules,* vol. 30, n° 20, p. 6333-6338.

Kim, P., N.M. Doss, J.P. Tillotson, P.J. Hotchkiss, M.J. Pan, S.R. Marder, J. Li, J.P. Calame et J.W. Perry. 2009. « High energy density nanocomposites based on surface-modified BaTiO3 and a ferroelectric polymer ». *ACS nano,* vol. 3, n° 9, p. 2581-2592.

Koledintseva, Marina Y, Sandeep K Patil, Robert W Schwartz, Wayne Huebner, Konstantin N Rozanov, Jianxiang Shen et Ji Chen. 2009. « Prediction of effective permittivity of diphasic dielectrics as a function of frequency ». *Dielectrics and Electrical Insulation, IEEE Transactions on,* vol. 16, n° 3, p. 793-808.

Kornmann, X., H. Lindberg et L.A. Berglund. 2001. « Synthesis of epoxy–clay nanocomposites: influence of the nature of the clay on structure ». *Polymer,* vol. 42, n° 4, p. 1303-1310.

Rapport-gratuit.com
LE NUMERO 1 MONDIAL DU MÉMOIRES

Kremer, F., et A. Schönhals. 2003. *Broadband dielectric spectroscopy*. Springer Verlag.

Lagaly, G. 1981. « Characterization of clays by organic compounds ». *CLAY MINER. Clay Miner.,* vol. 16, n° 1, p. 1.

Lagaly, G. 1986. « Interaction of alkylamines with different types of layered compounds ». *Solid State Ionics,* vol. 22, n° 1, p. 43-51.

Lai, S. M., W. C. Chen et X. S. Zhu. 2009. « Melt mixed compatibilized polypropylene/clay nanocomposites: Part 1 – the effect of compatibilizers on optical transmittance and mechanical properties ». *Composites Part A: Applied Science and Manufacturing,* vol. 40, n° 6–7, p. 754-765.

Lal, K, et R Parshad. 1973. « The permittivity of heterogeneous mixtures ». *Journal of Physics D: Applied Physics,* vol. 6, n° 11, p. 1363.

Laredo, E, M Grimau, F Sanchez et A Bello. 2003. « Water absorption effect on the dynamic properties of nylon-6 by dielectric spectroscopy ». *Macromolecules,* vol. 36, n° 26, p. 9840-9850.

Le Huy, HM, et J Rault. 1994. « Remarks on the α and β transitions in swollen polyamides ». *Polymer,* vol. 35, n° 1, p. 136-139.

Lertwimolnun, W., et B. Vergnes. 2005. « Influence of compatibilizer and processing conditions on the dispersion of nanoclay in a polypropylene matrix ». *Polymer,* vol. 46, n° 10, p. 3462-3471.

Lertwimolnun, Wiboon. 2006. « Réalisation de nanocomposites polypropylène/argile par extrusion bivis ». École Nationale Supérieure des Mines de Paris.

Lewis, TJ. 1994. « Nanometric dielectrics ». *Dielectrics and Electrical Insulation, IEEE Transactions on,* vol. 1, n° 5, p. 812-825.

Lewis, TJ. 2004. « Interfaces are the dominant feature of dielectrics at the nanometric level ». *Dielectrics and Electrical Insulation, IEEE Transactions on,* vol. 11, n° 5, p. 739-753.

Lonkar, Sunil P., Sandrine Therias, Fabrice Leroux, Jean-Luc Gardette et Raj Pal Singh. 2012. « Thermal, mechanical, and rheological characterization of polypropylene/layered double hydroxide nanocomposites ». *Polymer Engineering & Science,* vol. 52, n° 9, p. 2006-2014.

Looyenga, H. 1965. « Dielectric constants of heterogeneous mixtures ». *Physica,* vol. 31, n° 3, p. 401-406.

López-Quintanilla, M. L., S. Sánchez-Valdés, L. F. Ramos de Valle et F. J. Medellín-Rodríguez. 2006. « Effect of some compatibilizing agents on clay dispersion of polypropylene-clay nanocomposites ». *Journal of Applied Polymer Science,* vol. 100, n° 6, p. 4748-4756.

Ma, Dongling, Treese A Hugener, Richard W Siegel, Anna Christerson, Eva Mårtensson, Carina Önneby et Linda S Schadler. 2005. « Influence of nanoparticle surface modification on the electrical behaviour of polyethylene nanocomposites ». *Nanotechnology,* vol. 16, n° 6, p. 724.

Madejová, J. 2003. « FTIR techniques in clay mineral studies ». *Vibrational Spectroscopy,* vol. 31, n° 1, p. 1-10.

McCall, David W, et Ernest W Anderson. 1960. « Dielectric properties of linear polyamides ». *The Journal of Chemical Physics,* vol. 32, p. 237.

Montanari, Gian Carlo, Davide Fabiani, Fabrizio Palmieri, Dirk Kaempfer, Ralf Thomann et Rolf Mulhaupt. 2004. « Modification of electrical properties and performance of EVA and PP insulation through nanostructure by organophilic silicates ». *Dielectrics and Electrical Insulation, IEEE Transactions on,* vol. 11, n° 5, p. 754-762.

Morawiec, J., A. Pawlak, M. Slouf, A. Galeski, E. Piorkowska et N. Krasnikowa. 2005. « Preparation and properties of compatibilized LDPE/organo-modified montmorillonite nanocomposites ». *European Polymer Journal,* vol. 41, n° 5, p. 1115-1122.

Nelson, J.K., et J.C. Fothergill. 2004. « Internal charge behaviour of nanocomposites ». *Nanotechnology,* vol. 15, n° 5, p. 586.

Nilsson, F., U. W. Gedde et M. S. Hedenqvist. 2011. « Modelling the relative permittivity of anisotropic insulating composites ». *Composites Science and Technology,* vol. 71, n° 2, p. 216-221.

Noda, N., Y.H. Lee, A.J. Bur, V.M. Prabhu, C.R. Snyder, S.C. Roth et M. McBrearty. 2005. « Dielectric properties of nylon 6/clay nanocomposites from on-line process monitoring and off-line measurements ». *Polymer,* vol. 46, n° 18, p. 7201-7217.

Osman, M.A., J.E.P. Rupp et U.W. Suter. 2005. « Tensile properties of polyethylene-layered silicate nanocomposites ». *Polymer,* vol. 46, n° 5, p. 1653-1660.

Peng, Jin-hui, Jing-jing Yang, Ming Huang, Jun Sun et Zhong-yuan Wu. 2009. « Simulation and analysis of the effective permittivity for two-phase composite medium ». *Frontiers of Materials Science in China,* vol. 3, n° 1, p. 38-43.

Pereira de Abreu, D. A., P. Paseiro Losada, I. Angulo et J. M. Cruz. 2007. « Development of new polyolefin films with nanoclays for application in food packaging ». *European Polymer Journal,* vol. 43, n° 6, p. 2229-2243.

Perez, Naum Andres. 2008. « Etude Calorimétrique et Diélectrique de Nanocomposites Silicones ». Institut National Polytechnique de Grenoble-INPG.

Purohit, P.J., J.E. Huacuja-Sánchez, D.Y. Wang, F. Emmerling, A. Thünemann, G. Heinrich et A. Schönhals. 2011. « Structure–Property Relationships of Nanocomposites Based on Polypropylene and Layered Double Hydroxides ». *Macromolecules,* vol. 44, n° 11, p. 4342-4354.

Qiu, Longzhen, Wei Chen et Baojun Qu. 2006. « Morphology and thermal stabilization mechanism of LLDPE/MMT and LLDPE/LDH nanocomposites ». *Polymer,* vol. 47, n° 3, p. 922-930.

Ranade, Ajit, Nandika Anne D'Souza et Bruce Gnade. 2002. « Exfoliated and intercalated polyamide-imide nanocomposites with montmorillonite ». *Polymer,* vol. 43, n° 13, p. 3759-3766.

Rigaud, Bernard, Jean-Pierre Morucci et Nicolas Chauveau. 1995. « Bioelectrical impedance techniques in medicine. Part I: Bioimpedance measurement. Second section: impedance spectrometry ». *Critical reviews in biomedical engineering,* vol. 24, n° 4-6, p. 257-351.

Sanchez-Valdes, S., J. Méndez-Nonell, FJ Medellin-Rodriguez, E. Ramirez-Vargas, JG Martinez-Colunga, H. Soto-Valdez, L. Munoz-Jimenez et G. Neira-Velázquez. 2009. « Effect of PEgMA/amine silane compatibilizer on clay dispersion of polyethylene-clay nanocomposites ». *Polymer bulletin,* vol. 63, n° 6, p. 921-933.

SAWI, Ihab EL. 2010. « Dispersion de nanotubes de carbone et integration de la fonction de conductivite electrique dans les materiaux composites structuraux, Thèse de doctorat de l'Université Toulouse III - Paul Sabatier ».

Schneuwly, A, P Groning, L Schlapbach, C Irrgang et J Vogt. 1998. « Breakdown behavior of oil-impregnated polypropylene as dielectric in film capacitors ». *Dielectrics and Electrical Insulation, IEEE Transactions on,* vol. 5, n° 6, p. 862-868.

Shen, Yang, Yuanhua Lin, Ming Li et C-W Nan. 2007. « High dielectric performance of polymer composite films induced by a percolating interparticle barrier layer ». *Advanced Materials,* vol. 19, n° 10, p. 1418-1422.

Sihvola, A. H., et Jin-Au Kong. 1988a. « Effective permittivity of dielectric mixtures ». *Geoscience and Remote Sensing, IEEE Transactions on,* vol. 26, n° 4, p. 420-429.

Sihvola, Ari H, et Jin Au Kong. 1988b. « Effective permittivity of dielectric mixtures ». *Geoscience and Remote Sensing, IEEE Transactions on,* vol. 26, n° 4, p. 420-429.

Sinha Ray, Suprakas, et Masami Okamoto. 2003. « Polymer/layered silicate nanocomposites: a review from preparation to processing ». *Progress in polymer science,* vol. 28, n° 11, p. 1539-1641.

Std-930, IEEE. 2004.

Sun, Yangyang, Zhuqing Zhang et CP Wong. 2005. « Influence of interphase and moisture on the dielectric spectroscopy of epoxy/silica composites ». *Polymer,* vol. 46, n° 7, p. 2297-2305.

Százdi, László, Béla Pukánszky Jr, Enikő Földes et Béla Pukánszky. 2005. « Possible mechanism of interaction among the components in MAPP modified layered silicate PP nanocomposites ». *Polymer,* vol. 46, n° 19, p. 8001-8010.

Tan, H., et W. Yang. 1998. « Toughening mechanisms of nano-composite ceramics ». *Mechanics of materials,* vol. 30, n° 2, p. 111-123.

Tanaka, T., G. C. Montanari et R. Mulhaupt. 2004. « Polymer nanocomposites as dielectrics and electrical insulation-perspectives for processing technologies, material characterization and future applications ». *Dielectrics and Electrical Insulation, IEEE Transactions on,* vol. 11, n° 5, p. 763-784.

Thelakkadan, AS, G Coletti, F Guastavino et A Fina. « Effect of clay dispersion methods on the mechano-dynamical and electrical properties of epoxy–organoclay nanocomposites ». *Polymer Bulletin*, p. 1-18.

Tilmatine, Amar. 2006. « MATERIAUX DIELECTRIQUES « Notes du cours Diélectrique chapitre 7» ».

Tomer, V., G. Polizos, CA Randall et E. Manias. 2011. « Polyethylene nanocomposite dielectrics: Implications of nanofiller orientation on high field properties and energy storage ». *Journal of Applied Physics,* vol. 109, n° 7, p. 074113-074113-11.

Torquato, Salvatore. 2002. *Random heterogeneous materials: microstructure and macroscopic properties*, 16. Springer.

Tsagaropoulos, George, et Adi Eisenburg. 1995. « Direct observation of two glass transitions in silica-filled polymers. Implications to the morphology of random ionomers ». *Macromolecules,* vol. 28, n° 1, p. 396-398.

Tuncer, Enis, Stanisław M Gubanski et B Nettelblad. 2001. « Dielectric relaxation in dielectric mixtures: Application of the finite element method and its comparison with

dielectric mixture formulas ». *Journal of Applied Physics,* vol. 89, n° 12, p. 8092-8100.

Tuncer, Enis, Stanisław M. Gubański et B. Nettelblad. 2001. « Dielectric relaxation in dielectric mixtures: Application of the finite element method and its comparison with dielectric mixture formulas ». *Journal of Applied Physics,* vol. 89, n° 12, p. 8092-8100.

Tuncer, Enis, Bo Nettelblad et Stanisław M Gubañski. 2002. « Non-Debye dielectric relaxation in binary dielectric mixtures (50-50): Randomness and regularity in mixture topology ». *Journal of applied physics,* vol. 92, n° 8, p. 4612-4624.

Tuncer, Enis, Adam J Rondinone, Jonathan Woodward, Isidor Sauers, D Randy James et Alvin R Ellis. 2009. « Cobalt iron-oxide nanoparticle modified poly (methyl methacrylate) nanodielectrics ». *Applied Physics A,* vol. 94, n° 4, p. 843-852.

Tuncer, Enis, Yuriy V Serdyuk et Stanislaw M Gubanski. 2002. « Dielectric mixtures: electrical properties and modeling ». *Dielectrics and Electrical Insulation, IEEE Transactions on,* vol. 9, n° 5, p. 809-828.

Tuncer, Enis, YV Serdyuk et SM Gubanski. 2001. « Comparing dielectric properties of binary composite structures obtained with different calculation tools and methods ». In *Electrical Insulation and Dielectric Phenomena, 2001 Annual Report. Conference on*. p. 665-668. IEEE.

Utracki, LA, et MR Kamal. 2002. « Clay-containing polymeric nanocomposites ». *Arabian Journal Science & Engineering--special issue,* vol. 27, n° 1C, p. 43-67.

Vaia, R.A., R.K. Teukolsky et E.P. Giannelis. 1994. « Interlayer structure and molecular environment of alkylammonium layered silicates ». *Chemistry of Materials,* vol. 6, n° 7, p. 1017-1022.

Venkatasubramanian, N, KEVIN J Wiacek, SANDRA Fries-Carr, ERIC Fossum et THUY D Dang. 2007. « High-temperature polymer dielectrics for capacitive energy-storage applications ». In *POLYIMIDES AND OTHER HIGH TEMPERATURE POLYMERS-INTERNATIONAL SYMPOSIUM-*. Vol. 4, p. 393. VSP.

Venkatesh, G. S., A. Deb, Ajay Karmarkar et Shakti S. Chauhan. 2012. « Effect of nanoclay content and compatibilizer on viscoelastic properties of montmorillonite/polypropylene nanocomposites ». *Materials & Design,* vol. 37, n° 0, p. 285-291.

Venkatesulu, B., B. L. G. Jonsson, H. Edin et M. Norgren. 2013. « Modeling of insulating nanocomposites-electric and temperature fields ». *Dielectrics and Electrical Insulation, IEEE Transactions on,* vol. 20, n° 1, p. 177-184.

Villanueva, M. P., L. Cabedo, E. Giménez, J. M. Lagarón, P. D. Coates et A. L. Kelly. 2009. « Study of the dispersion of nanoclays in a LDPE matrix using microscopy and in-process ultrasonic monitoring ». *Polymer Testing,* vol. 28, n° 3, p. 277-287.

Vorob'ev, AA. 1980. « Excitation and electrical breakdown of solid insulators ». *Soviet Physics Journal,* vol. 23, n° 5, p. 382-386.

Wang, Ki Hyun, Min Ho Choi, Chong Min Koo, Yeong Suk Choi et In Jae Chung. 2001. « Synthesis and characterization of maleated polyethylene/clay nanocomposites ». *Polymer,* vol. 42, n° 24, p. 9819-9826.

Wen, Jianye, et Garth L Wilkes. 1996. « Organic/inorganic hybrid network materials by the sol-gel approach ». *Chemistry of Materials,* vol. 8, n° 8, p. 1667-1681.

Xu, Weibing, Guodong Liang, Wei Wang, Shupei Tang, Pingsheng He et Wei-Ping Pan. 2003. « PP–PP-g-MAH–Org-MMT nanocomposites. I. Intercalation behavior and microstructure ». *Journal of applied polymer science,* vol. 88, n° 14, p. 3225-3231.

Yasue, K, S Katahira, M Yoshikawa et K Fujimoto. 2000. « In situ polymerization route to nylon 6-clay nanocomposites ». *Polymer-Clay Nanocomposites, Wiley, New York.*

Zakrevskii, VA, NT Sudar, A Zaopo et Yu A Dubitsky. 2003. « Mechanism of electrical degradation and breakdown of insulating polymers ». *Journal of applied Physics,* vol. 93, n° 4, p. 2135-2139.

Zazoum, B, E David et AD Ngô. 2013. « LDPE/HDPE/Clay Nanocomposites: Effects of Compatibilizer on the Structure and Dielectric Response ». *Journal of Nanotechnology,* vol. 2013.

Zhang, X., Z. Liu, Q. Li, Y. Leung, K. Ip et S. Hark. 2005. « Routes to grow well-aligned arrays of ZnSe nanowires and nanorods ». *Advanced Materials,* vol. 17, n° 11, p. 1405-1410.

Zhao, K., et K. He. 2006. « Dielectric relaxation of suspensions of nanoscale particles surrounded by a thick electric double layer ». *Physical Review B,* vol. 74, n° 20, p. 205319.

Zhao, Zhongfu, Tao Tang, Yongxin Qin et Baotong Huang. 2003. « Relationship between the continually expanded interlayer distance of layered silicates and excess intercalation of cationic surfactants ». *Langmuir,* vol. 19, n° 22, p. 9260-9265.

Zhu, Zi-Kang, Yong Yang, Jie Yin, Xin-Yu Wang, Yang-Chuan Ke et Zong-Neng Qi. 1999. « Preparation and properties of organosoluble montmorillonite/polyimide hybrid materials ». *Journal of applied polymer science,* vol. 73, n° 11, p. 2063-2068.